FAA-RD-76-3, II

Project Report
ATC-63
Volume II

MLS Multipath Studies
Volume II: Application of Multipath Model to Key MLS Performance Issues

J. E. Evans
R. B. Burchsted
J. Capon
R. S. Orr
D. A. Shnidman
S. M. Sussman

25 February 1976

Lincoln Laboratory
MASSACHUSETTS INSTITUTE OF TECHNOLOGY
LEXINGTON, MASSACHUSETTS

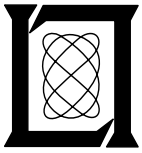

Prepared for the Federal Aviation Administration,
Washington, D.C. 20591

This document is available to the public through
the National Technical Information Service,
Springfield, VA 22161

1. Report No.	2. Government Accession No.	3. Recipient's Catalog No.
FAA-RD-76-3, II		

4. Title and Subtitle	5. Report Date
MLS Multipath Studies Volume II: Application of Multipath Model to Key MLS Performance Issues	25 February 1976 6. Performing Organization Code

7. Author(s)	8. Performing Organization Report No.
J.E. Evans, J. Capon, D.A. Shnidman R.B. Burchsted, R.S. Orr, S.M. Sussman	ATC-63, Vol. II

9. Performing Organization Name and Address	10. Work Unit No. (TRAIS)
Massachusetts Institute of Technology Lincoln Laboratory P.O. Box 73 Lexington, MA 02173	11. Contract or Grant No. DOT-FA74WAI-461

12. Sponsoring Agency Name and Address	13. Type of Report and Period Covered
Department of Transportation Federal Aviation Administration Systems Research and Development Service Washington, DC 20591	Project Report 14. Sponsoring Agency Code

15. Supplementary Notes

The work reported in this document was performed at Lincoln Laboratory, a center for research operated by Massachusetts Institute of Technology under Air Force Contract F19628-76-C-0002.

16. Abstract

This report summarizes MLS multipath work carried out at Lincoln Laboratory from March 1974 to Sept. 30, 1975. The focus of the program is the development of realistic models for 1) the multipath in representative real world environments and 2) the multipath characteristic of candidate MLS techniques. These multipath and system models are used in a comprehensive computer simulation to predict the strengths and weaknesses of major MLS systems when subjected to representative real world environments. The report is organized into two volumes. Volume I describes the algorithms and validation of various portions of the program. In Volume II, the simulation (or selected portions thereof) is applied to key multipath related MLS issues.

Mathematical models are given for the major MLS multipath sources (ground reflections, building and aircraft reflections, and shadowing by objects and humped runways), and it is shown that they agree well with field data (including the Lincoln measurements at Logan Airport). Models for the techniques (Doppler and scanning beam) considered in phase II of the U.S. MLS program are presented together with validation by comparison with theory and bench tests. Also presented are the results of a general study in motion averaging.

The (validated) computer simulation (and portions thereof) is then applied to studying 1) the critical areas required by the TRSB system to avoid excessive reflection effects, 2) the expected TRSB performance with vertical polarization and benefits that might be derived with an alternative polarization and 3) siting of a specific TRSB system at Friendship International Airport (MD).

17. Key Words	18. Distribution Statement
Microwave landing system L-band multipath C-band multipath	Document is available to the public through the National Technical Information Service, Springfield, Virginia 22151.

19. Security Classif. (of this report)	20. Security Classif. (of this page)	21. No. of Pages	
Unclassified	Unclassified	178	

VOLUME I

TABLE OF CONTENTS

VOLUME II

TABLE OF CONTENTS

VOLUME II

LIST OF ILLUSTRATIONS

VIII. CRITICAL AREAS STUDIES PART 1: REFLECTION EFFECTS

One of the prime applications to date of the Lincoln Laboratory MLS multipath model has been determining the critical areas for TRSB operation. These are the areas in which restrictions must be placed on vehicle/aircraft movement to avoid excessive azimuth or elevation errors. The first phase of the work has concentrated on determining restrictions required to avoid excessive errors due to reflection effects; in the next phase, the restrictions needed to avoid excessive shadowing effects will be determined.

For purposes of this study, we have defined the critical areas to be those points on the airport surface from which parked or taxiing aircraft and vehicles should be excluded as to avoid out-of-tolerance perturbations in the MLS guidance signal quality. This definition essentially coincides with that advanced by Rondini and McFarland [38] for conventional ILS.

It is recognized that conventional ILS divides the above zone into "critical" and "sensitive" areas where aircraft/vehicles may be taxiing, but not parked. The basis for this division has not clearly been set down. Since it seems to hinge on a number of operational considerations which need to be closely reexamined in the MLS context,* we (like McFarland) have chosen not to match the current ILS practice, but rather to present the basic "physics" data from which one could attempt such a division.

---

*For example, MLS is intended to provide cat II autoland capability for all of the "basic" configurations whereas this capability exists at a very small number of current ILS runways.

One possible approach to determining the critical areas would be to run a full scale simulation with a given scatterer at each possible location at which an error might be generated. However, there is a sufficiently large number of performance-related issues which need to be studied parametrically, e.g.,

(a) multipath scatterer parameters

trucks - sizes
aircraft - type

(b) transmitter antennas

patterns in both elevation and azimuth planes
siting (including height)

(c) receiver parameters

velocity
airborne antenna patterns,

that the total volume of computer runs and data analysis would clearly be prohibitive.

Therefore, we opted for the following two step approach to quantify the errors for a given reflector with given system parameters:

1. Step 1: Identify the airport surface areas of greatest concern by determining contours of the "worst case" static dynamic error as a function of scatterer location on the surface for fixed transmitter and receiver locations (e.g., cat I and II decision heights). Repeat this for a variety of receiver locations to identify the areas of greatest concern.

2. Step 2: Run full system simulations with a given reflector located at representative points identified in step 1, so as to examine:

   (a) changes in multipath amplitude and separation angle from a fixed scatterer as receiver moves (in step 1, the scatterer orientation at a fixed location changes when the receiver position changes),

   (b) raw error histories as well as flight control system model outputs (path following filters, etc.),

   (c) effects of several scatterers being simultaneously present.

The next section describes the method used to determine the "worst case" error contours. Section 8.2 describes the results of the "error contour" program for the TRSB Basic Wide Aperture and Basic Narrow Aperture systems.*

In Section 8.3, the method of making full system runs is described, while Section 8.4 gives the results for some representative full runs. In Section 8.5, we draw some conclusions as to the critical areas required by TRSB to avoid significant reflection errors.

---

*To permit lower cost, the TRSB configuration at most airports will be chosen from two basic configurations: "wide" or "narrow." The basic wide system with a 60λ aperture in the scanned plane is intended for the more demanding applications (e.g., long runways and/or low glide slopes) while the basic narrow (with 30-40λ apertures) is to provide a lower cost solution at the less demanding sites. Thus, differences in critical areas may be a prime factor in choice of system for a given runway.

8.1 Determination of "Worst Case" Error Contours

This section describes the technical approach taken in the critical area study error contours computer program. This program generates and plots contours of constant static or dynamic TRSB error in either azimuth or elevation for scattering by a single building or aircraft. Either an omni or a forward-looking airborne antenna pattern can be selected.

For fixed transmitter and receiver locations, the program initially evaluates the "worst case" static error arising from the placement of a scattering obstacle (building or aircraft) at each point on a rectangular grid in the runway plane. Worst case error is characterized by two conditions; first of all, the obstacle is oriented so that the specular reflection point is horizontally centered upon it. Secondly, the phase relationships among the received signal components are selected in a manner which gives rise to peak error. Following the static error calculation, the user may opt for a dynamic error plot which shows the effects due to motion averaging.

The scattering properties, with the exception of the ground reflection (see Section 3), are computed by the programs incorporated in the full MLS simulation. The TRSB errors are estimated using an error approximation derived in Appendix C.

(a) Obstacle Grid

Separate grids are used for AZ and EL, since they have distinct transmitter locations and greatly different in-beam coverage zones. As shown in Fig. 8-1, a grid is specified as follows. A rectangle (two sides parallel to centerline) in front of the transmitter is designated by two opposite

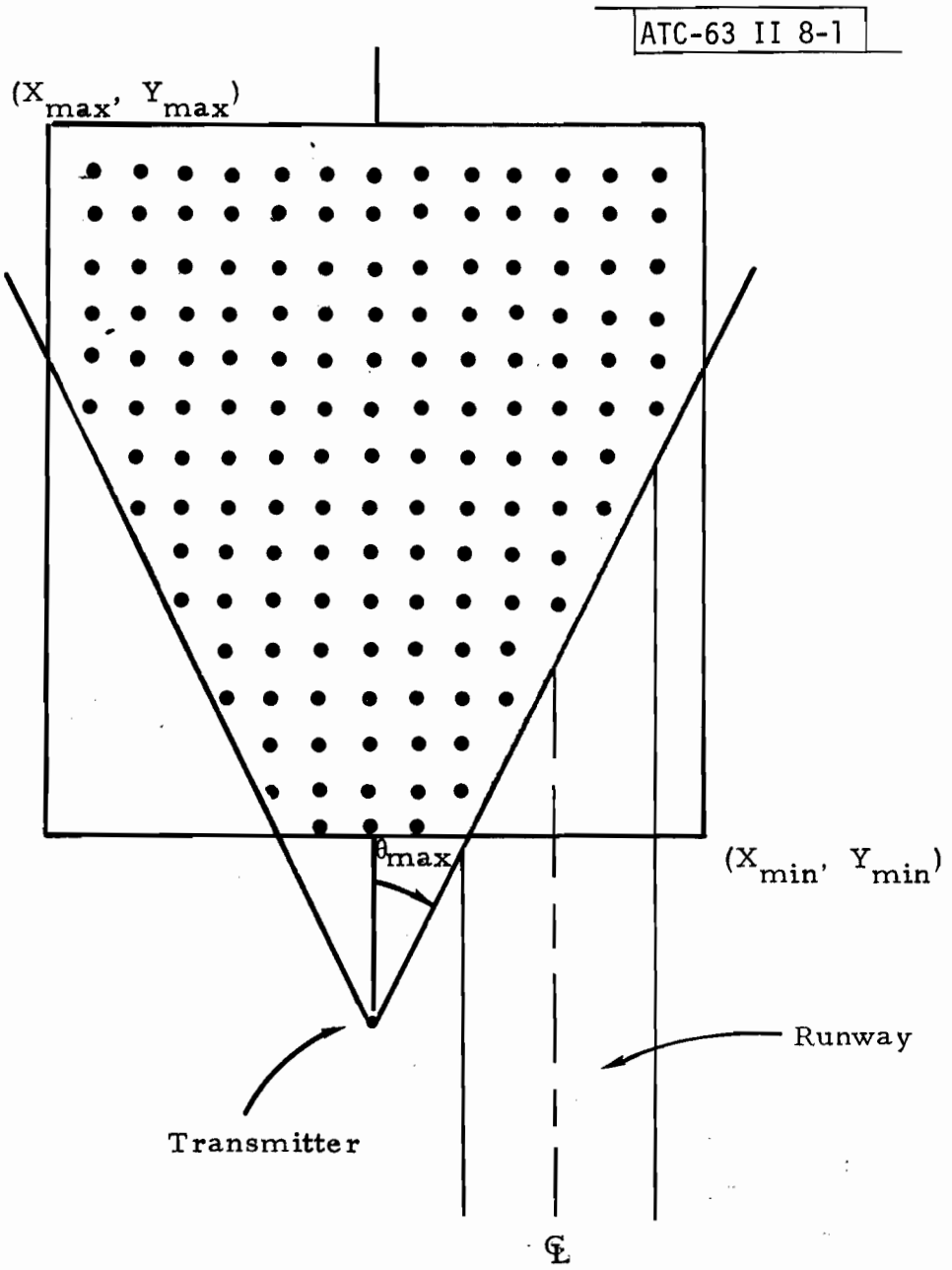

Fig. 8-1. Obstacle placement grid for critical area study.

corner points (X_{min}, Y_{min}), (X_{max}, Y_{max}). The grid area consists of all points common to the rectangle and an angular sector ranging over $\pm\theta_{max}$ relative to a half-line (directed towards threshold) emanating from the transmitter and parallel to centerline. For elevation, $\theta_{max} = 40°$; in azimuth, $\theta_{max} = 2$ BW (BW is the antenna beamwidth, an input parameter). The actual obstacle locations constitute a rectangular grid with specifiable increments X_{inc}, Y_{inc}.

(b) Obstacle Orientation

The scattering obstacle may be either a building or a parked aircraft. Buildings are centered on the grid point. Orientation for specular reflection is accomplished by rotating the building to an angle α, where (see Fig. 8-2)

$$\alpha = \frac{\theta - \psi}{2} \tag{8-1}$$

For parked aircraft, the fuselage center lies on the grid point. Angular orientation is the same as for buildings, which is equivalent to approximating the fuselage cylinder by a flat plate. This approximation is accurate except for cases in which the specular point lies on a tangent plane which is inclined appreciably with respect to the vertical. In such cases, a search procedure is used to rotate the fuselage so that the specular point lies near the fuselage center. The tail end of the aircraft is towards the stop end of the runway, the intent being to simulate an aircraft which is taxiing towards threshold end for take-off.

ATC-63 II 8-2

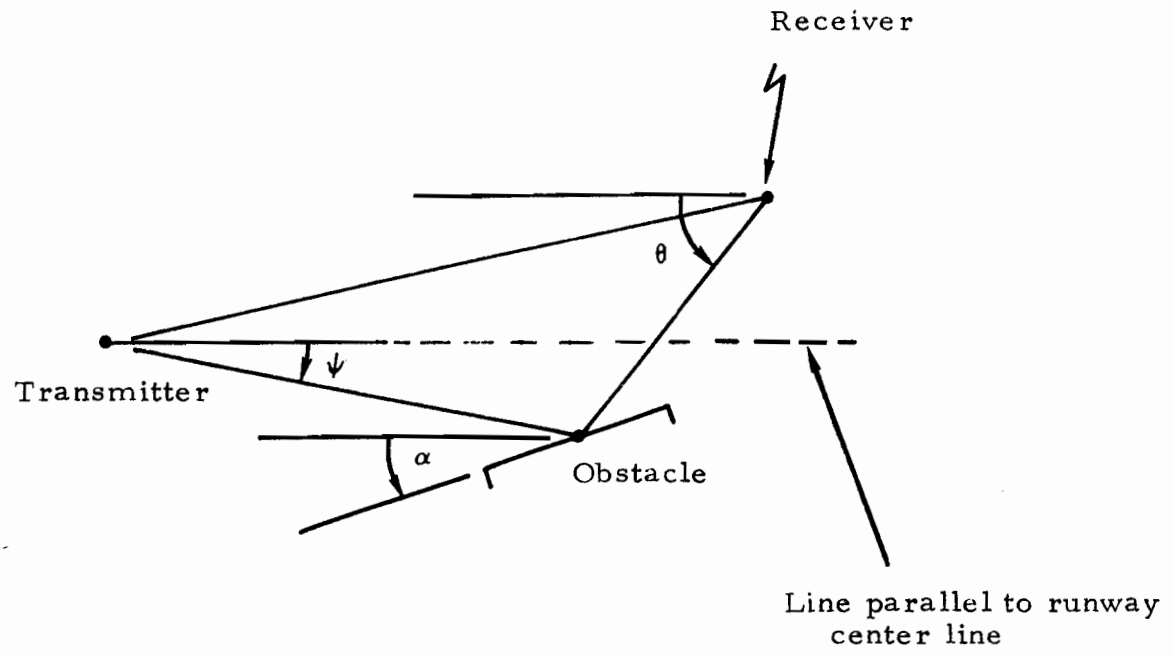

Fig. 8-2. Obstacle orientation for critical area study.

Placement of the fuselage specular point at the fuselage center is chosen to maximize the fuselage multipath. In doing so, it is important to ensure that the tail fin multipath is not inadvertently eliminated or minimized, since the tail fin center can be quite removed from the fuselage center (~90 ft for a B747). However, since the tail fin is modeled as a section of vertical circular cylinder rather than a flat plate, its specular point will not be the same as that of the fuselage. Due to the curvature of the tail, its specular point will migrate along with it as the tail is displaced horizontally in the vertical plane defined by the fuselage axis. Thus, even though the tail fin center is displaced somewhat from the grid point, it will still exhibit specular reflection in most cases.

The above argument was checked experimentally with the program prior to performing the runs reported later on. From looking at contour plots of fuselage and tail fin errors separately, under conditions of both fuselage and tail fin centering of the specular point, it was found that tail centering reduced the fuselage component far below the values attained for fuselage centering, whereas fuselage centering did not reduce the tail fin errors significantly.

(c) Ground Reflection Multipath Computation

As indicated previously, the building and A/C multipath computations are done by the programs used in the MLS simulation. For the critical area study, the ground reflection routine, which uses a time-consuming numerical integration, has been replaced by a simpler algorithm which treats the ground as an infinite flat plate. The multipath amplitude is taken to be the Fresnel

reflection coefficient for vertical polarization, a formula for which is given in [47]. This formula depends only on the relative complex dielectric constant, ε_r, and the conical incidence angle relative to the surface normal, θ_o. The latter is given by

$$\theta_o = \tan^{-1} \frac{r_o}{h_t + h_r} \tag{8-2}$$

where (see Fig. 8-3)

h_t = transmitter height

h_r = receiver height

r_o = x-y plane distance from transmitter to receiver

Phase is computed by assuming 180° phase change at reflection and a differential path length of $2h_th_r/r_o$. The phase increment is $2\pi/\lambda$ times the differential path.

(d) Computation of Static TRSB AZ and EL Errors

For the initial critical area study, the TRSB static errors are obtained from an approximation formula rather than the TRSB simulation subroutines. This is done primarily for economy in computation time. In Appendix C, an approximate TRSB error formula is derived. The essential assumptions in the approximation are (1) Gaussian beam pattern and (2) small-to-moderate multipath amplitude. The result covers the case of multiple small amplitude scattering components. The details of the derivation are presented in Appendix C, but the result is simple -- the error is simply the algebraic sum of the single component errors. The error is given in beamwidths and

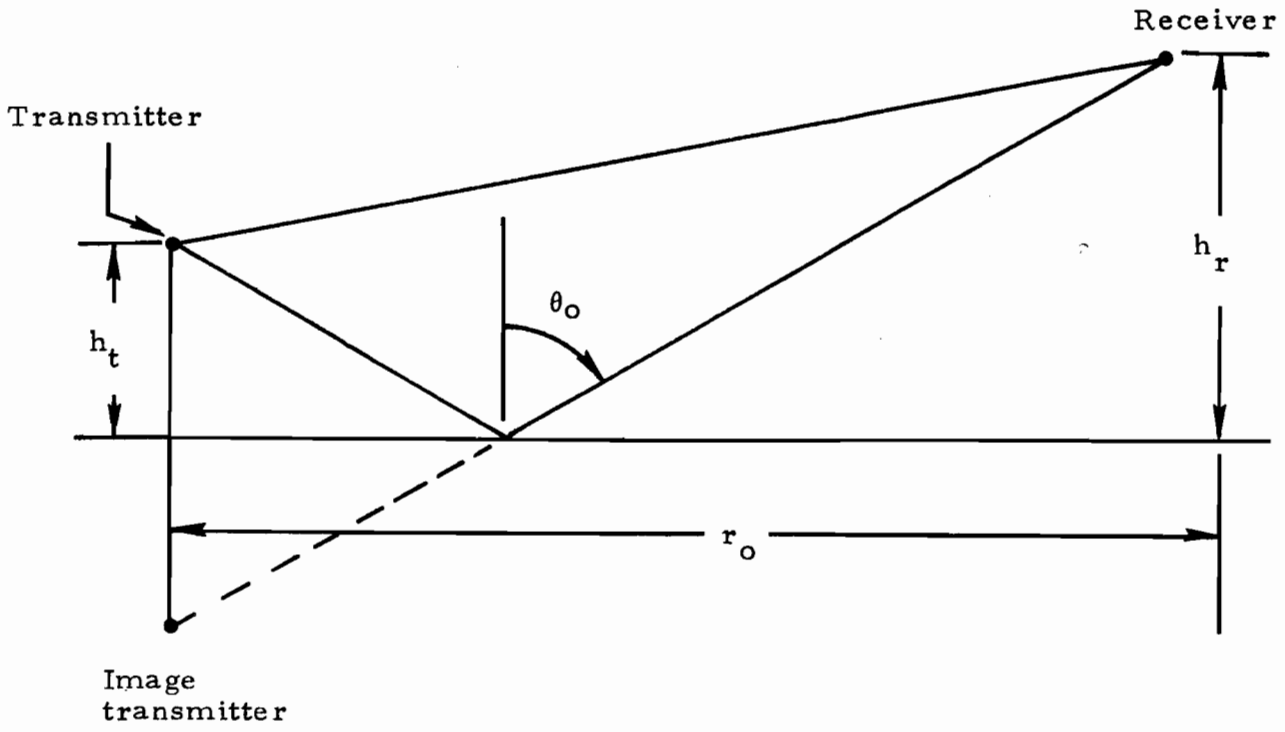

Fig. 8-3. Geometry for computation of specular ground reflection.

converted to degrees using the input beamwidth parameter. The formula has been compared to exact calculations in Section VI where we saw (see, e.g., Figs. 6-1 to 6-4) that for moderate multipath levels the formula compares quite well with the subroutine output and is quite adequate for the intended use.

The multipath levels are preprocessed prior to the error computation. The nature of the preprocessing depends on whether the system is AZ or EL and on whether the scatterer is a building or an aircraft. Each case is discussed in turn.

Building - AZ

Since the building surface is assumed to be perpendicular to the runway plane, all building multipath components emanate from the transmitter at a common azimuth angle, or equivalently, they all have a common separation angle from the direct path. By the same token, the ground reflection has 0° separation from the direct. Therefore the building components are combined coherently into a single effective multipath component; likewise, the direct and ground reflection are combined into an effective direct. The multipath amplitude ρ entered into the error formula is the ratio of the magnitudes of these:

$$\rho = \frac{\left| \sum_{\text{bldg}} \rho_i \text{expj}[\phi_i - \omega_c \tau_i] \right|}{\left| \sum_{\text{dir,gnd}} \rho_j \text{expj}[\phi_j - \omega_c \tau_j] \right|} \qquad (8\text{-}3)$$

The relative phase need not be computed; worst case error is obtained by entering phase = 0° into the formula.

Aircraft - AZ

For aircraft scattering, multipath computations are made for both the fuselage and tail fin. It is assumed that all fuselage components are at one separation angle (this may not be the case when the fuselage is close to the transmitter), and that the tail components are at another. The fuselage components are combined coherently, as are those of the tail, and the resultants are normalized to the effective direct signal defined above and used in the two component error formula. Phase of both components is set to zero for maximum error.

Building - EL

In elevation, only the X-O-R multipath is considered, it being the principal one which can arise from in-beam scattering. Although the X-O-G-R component could be in-beam, it is generally small and is neglected here. The two components which have a ground reflection between transmitter and obstacle are neglected on the grounds that they are well out-of-beam. The two components which have a ground reflection between transmitter and obstacle are neglected on the grounds that they are well out-of-beam. The specular ground reflection is treated similarly. Thus the single component error formula (with ϕ = 0°) is used.

Aircraft - EL

This case is perhaps the most complicated of the four. Three multipath components are used: tail fin (X-O-R) and fuselage (X-O-R and X-O-G-R).* All others are neglected. Separate errors for the fuselage and tail fin are computed and then combined in a manner specified below to yield a net error.

The tail fin error, e_T, is computed on the basis of the X-O-R term alone; again, zero phase is assumed for worst case error. For the fuselage, separate error magnitudes are computed for the two components, but the errors are combined in phase. Let $e_{F,XOR}$ and $e_{F,XOGR}$ stand for the peak values of these two errors. The net fuselage error is taken to be

$$e_F = e_{F,XOR} + e_{F,XOGR} \cos \Delta\phi \tag{8-4}$$

where $\Delta\phi$ is the differential phase between the two components:

$$\Delta\phi = \phi_{XOGR} - \phi_{XOR} - \omega_c(\tau_{XOGR} - \tau_{XOR}) \tag{8-5}$$

Generally, $e_{F,XOR}$ and $e_{F,XOGR}$ will be negative, due to negative conical separation angle.† Also, $e_{F,XOR}$ will usually be the larger of the two (in magnitude) because the corresponding multipath amplitude is larger. No matter what the value of $\Delta\phi$, then, e_F will generally be negative as well. By similar

---

*The fuselage X-O-G-R term may be in-beam and of appreciable amplitude, unlike the corresponding case for building reflections.

†For vertical planar reflectors, this will always be true unless the geometric specular point lies off the reflector and is artificially "pinned" to one of its sides. When, however, the scattering fuselage is near the transmitter, the multipath could be at greater elevation than the direct.

argument, e_T is also negative, resulting in a total error

$$e_{A/C} = e_F + e_T \tag{8-6}$$

which represents the largest negative error. In cases where $e_F > 0$, the largest positive error is computed:

$$e_{A/C} = e_F = e_T \; ; \; e_F > 0 \tag{8-7}$$

(e) Motion Averaging

Upon completion of a static error calculation and contour plot, dynamic errors for the same geometries can be calculated. An aircraft speed v is input (velocity assumed parallel to centerline) from which a scalloping frequency f_s is calculated:

$$f_s = \frac{v}{\lambda} (\cos \beta_d - \cos \beta_m) \tag{8-8}$$

where β_d and β_m are the arrival angles (projected into the runway plane for simplicity) of the direct and multipath components relative to the A/C velocity vector. If N uniformly spaced samples are taken over interval T, the static error is reduced approximately by the motion averaging factor

$$A_f = \frac{\sin \pi f_s T}{N \sin \frac{\pi f_s T}{N}} \tag{8-9}$$

Near scalloping frequencies $f_s = n/T$ (n not a multiple of N) the averaging factor is quite small, implying almost complete cancellation of errors. Assumptions not well satisfied in practice regarding unbiased estimates and

sinusoidal variation of error with multipath phase are involved in obtaining this result. To avoid optimistic predictions of error cancellation, the motion averaging factor is pinned at the random error averaging level $1/\sqrt{N}$ whenever the previous expression falls below that value. Thus the general relationship between static and dynamic error is

$$e_{dyn} = \max\left\{\frac{1}{\sqrt{N}}, A_f\right\} e_{stat} \qquad (8\text{-}10)$$

Three exceptions to the above are allowed. For elevation only, the sin x/x factor is reduced by 0.85 when the scalloping frequency is in the vicinity of the first grating lobe, $(N-1)/T \leq f_s \leq (N+1)/T$. This factor accounts for jitter in the EL-1 pulse spacing and was obtained from jitter spectra computations.* In both AZ and EL-1, the averaging factor A_f is set equal to $1/\sqrt{N}$ when $f_s > 85$ Hz. For these large scalloping frequencies, the multipath persistence is expected to be too short for coherent averaging of all the scans. For azimuth, averaging between the to-and-fro scans yields an additional multiplicative factor of $|\cos(\pi f_s T_z)|$, where T_z = time between 0° point on to-and-fro scans (which is assumed to be coherent for all scalloping rates), thus yielding

$$e_{dyn}(AZ) = |\cos \pi f_s T_z| \max\left(\frac{1}{\sqrt{N}}, A_f\right) e_{static}(AZ) \qquad (8\text{-}11)$$

(f) Airborne Antenna Pattern

A forward-looking Gaussian beam is assumed. The user enters a 3 dB

---

*These reductions were based on spectra for the scanning beam working group signal format [67]. It now appears that $1/\sqrt{N}$ should be used for the TRSB system for all $f_s \geq 5$ Hz.

beamwidth θ_{ab} and the multipath amplitude is adjusted by the ratio of multipath signal gain to direct signal gain:

$$\frac{G_{ab}(\beta_m)}{G_{ab}(\beta_d)} = e^{-\frac{k(\beta_m^2 - \beta_d^2)}{\theta_{ab}^2}} \quad : \quad k = 2 \ln 2 \tag{8-12}$$

If the scattering obstacle is a parked aircraft, the value of β_m entered corresponds to the fuselage specular point.

The airborne antenna weighting can be skipped by selecting an OMNI option.

8.2 Results for the "Worst Case" Error Contours

In this section, we present the results of the critical areas error contour program for the wide and narrow aperture TRSB systems. First, however, a few words are in order regarding the presentation format. The contour program yields contours at specified increments between specified upper and lower limits. In Fig. 8-4 we show contours every 0.02° from -0.01° to -0.21° for a static case, while Fig. 8-5 shows the corresponding contours for dynamic error.

Although the format of Figs. 8-4 and 8-5 allows a very detailed analysis of the error mechanisms, there are far too many lines to consider superimposing the contours for various parameter variations. Consequently, in the remainder of this chapter we have outlined only a single error contour for each choice of transmitter/scatterer/receiver parameters. In most cases, this contour is 0.03°, which was chosen as being approximately 50% of the MLS functional requirement specification for control noise errors. In a few cases where the error should be rather slowly varying with time, the 0.09° error contour was used as an approximation to the 0.1° path following error specification of the MLS functional requirements.

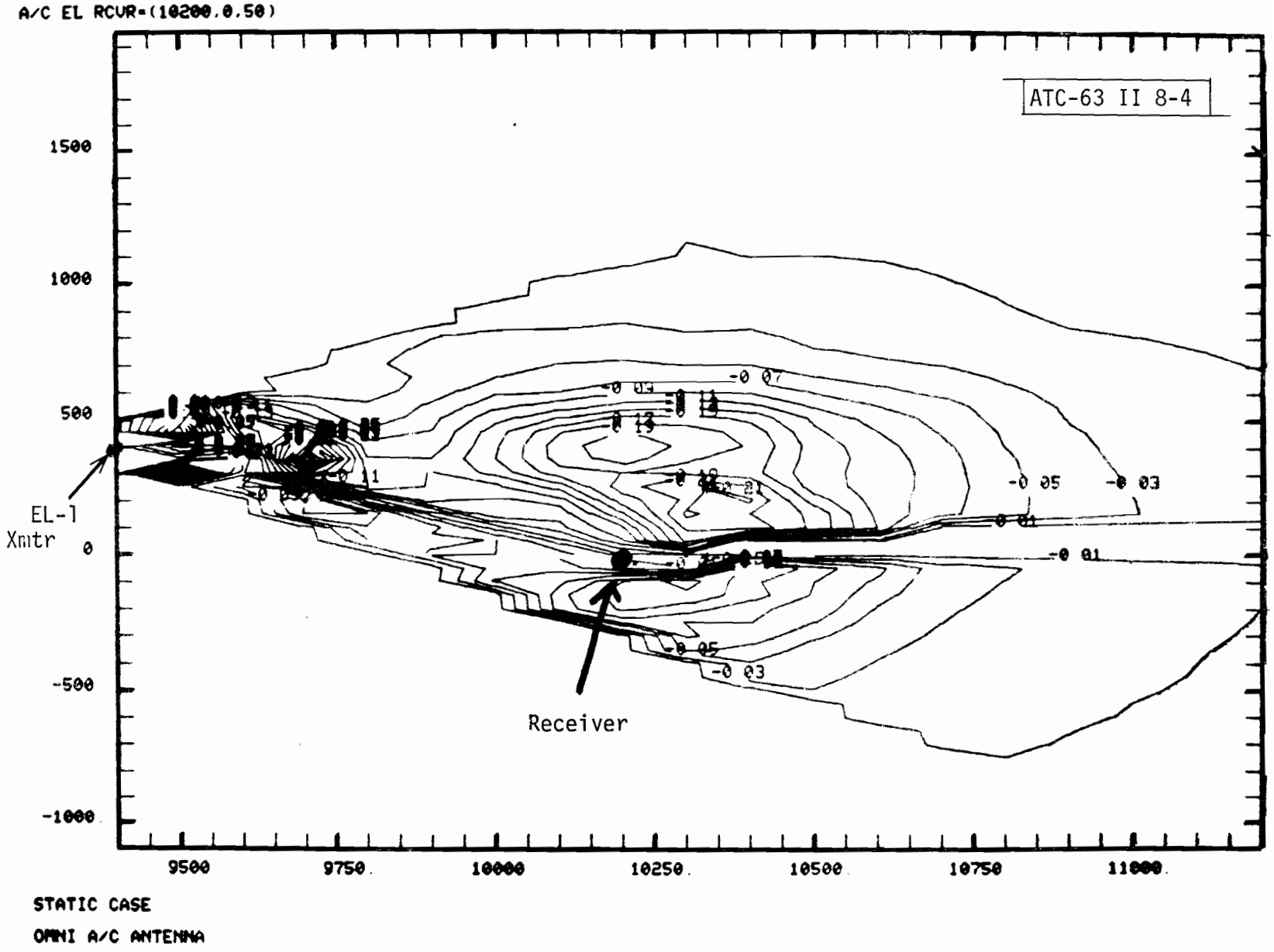

Fig. 8-4. Basic wide aperture EL-1 system: all contours for B747 scatterer when static receiver is at (10200, 0, 50).

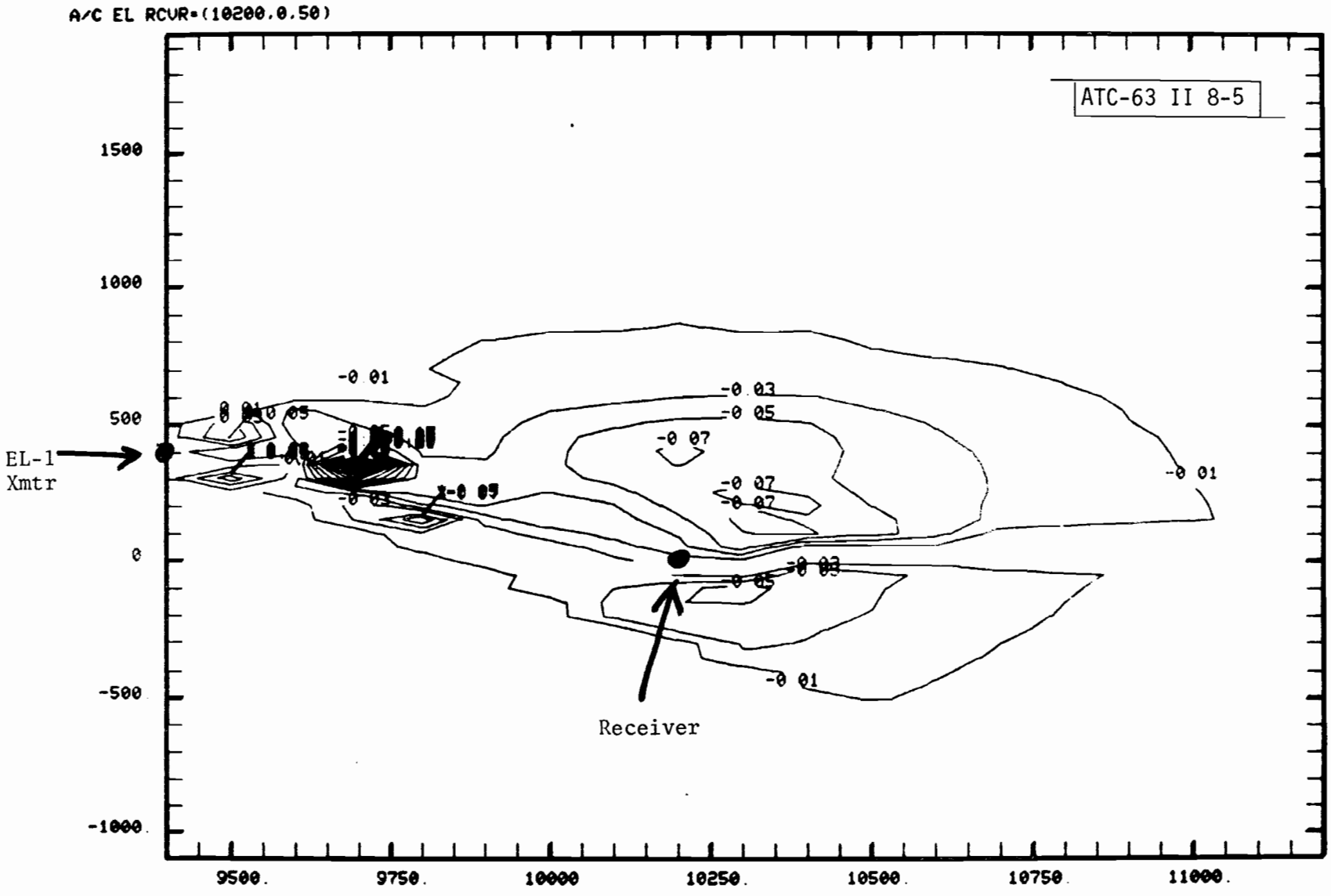

Fig. 8-5. Basic wide aperture EL-1 system: all error contours for B747 scatterer when receiver moving 200 feet per second is at (10200, 0, 50).

It should be kept in mind that these error contours assume worst case scatterer orientations and component summing. Consequently, there is reason to believe that they are sufficiently conservative to handle the case of several scatterers being present simultaneously. In Section 8.4, we shall see that the actual flight path errors for appropriately oriented aircraft are typically smaller than the corresponding contour values.

(a) Basic Wide Aperture El-l System

This system was considered to have a 1° beamwidth in the elevation plane with the azimuthal pattern recommended by the scanning beam working group. The transmitter phase center height was taken to be 10 feet above the local flat terrain, with the antenna displaced 400 feet from centerline and 200 feet forward of GPIP (to have the MLS glide slope at 2.86° coincide with an ILS glide slope).

The first figure considers errors due to trucks or small buildings. These were modeled as a flat perfect conductor some 15 feet high and 20 feet wide. Figure 8-6 shows the effect of receiver motion on the error contours for a receiver at the cat II minimum guidance altitude (MGA) of 50 feet.* We see that significant errors are generated approximately 350 feet in front of the antenna and 200 feet to either side. Motion averaging reduces the error contour size slightly at 100 feet/sec approach velocity and significantly at 200 ft/sec approach velocity. With a directional airborne antenna, the contours are essentially eliminated at 200 fps, while at greater heights (e.g., 100-200 ft) the 0.03° contour is a small ellipse centered within the 50-foot contour.

*This is also the point at which one might transition from EL-1/DME guidance to a radar altimeter for cat III flare.

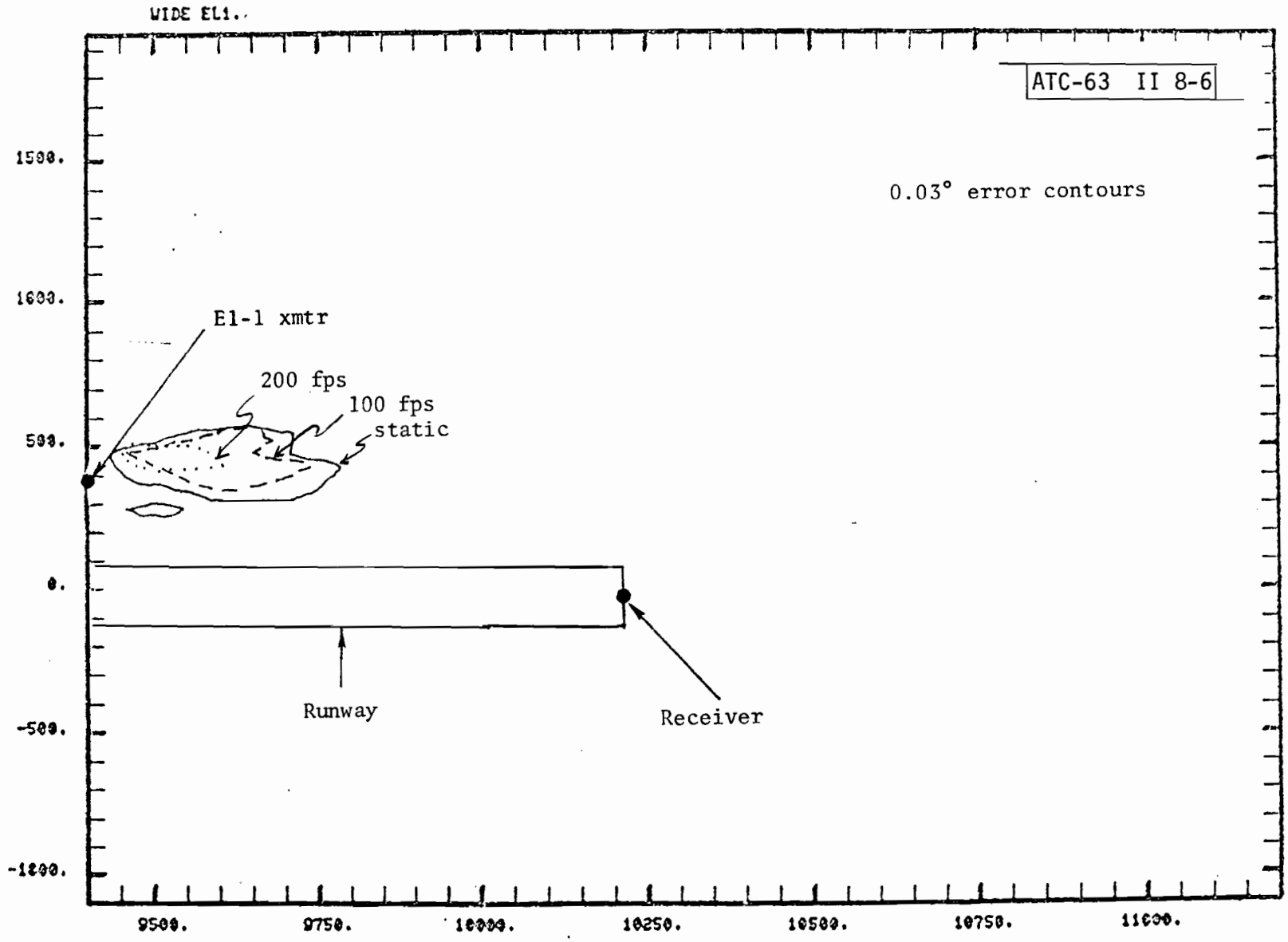

Fig. 8-6. Effect of receiver velocity on basic wide aperture EL-1 system: error contours for 15 x 20 truck scatterer when receiver is at (10200, 0, 50).

Next, we turn our attention to scattering aircraft. To be conservative, we assume a B747 scatterer. Figure 8-7 shows the error contours for a receiver at 50-foot altitude as a function of receiver motion. The tail fin generates a large region of significant errors for a static receiver. With motion averaging at 100 fps or 200 fps, the error contours are reduced significantly. However, a B747 aircraft would not be allowed in much of this area with existing obstacle clearance criteria. Also, much of the contour locations correspond to points to the side or rear of the receiver. A directional airborne antenna was found to sharply reduce the contour size, particularly when combined with motion averaging.

In Fig. 8-8, we show the error contours for various receiver heights. For receiver heights greater than the tail fin height ($\approx$ 60 ft at top), the significant errors are confined to a rectangle extending 400 feet in front of the EL-1 transmitter and approximately 150 feet to each side.

With ILS, it has been observed that the glide slope errors are sensitive to receiver lateral displacement. Error contours were calculated for receiver displacements of -0.25° in elevation and + 0.25° in azimuth at the cat II decision height of 100 feet. It was found that the error contours are elongated somewhat for a receiver displacement to the side of centerline away from the EL-1 transmitter. This arises because the angle of incidence on the tail fin increases, thus increasing the multipath levels.

A significant factor in reducing the TRSB EL-1 sensitivity to building reflections is the pattern control in the azimuth plane which rolls off at wide azimuths so as to reduce building multipath levels. However, this

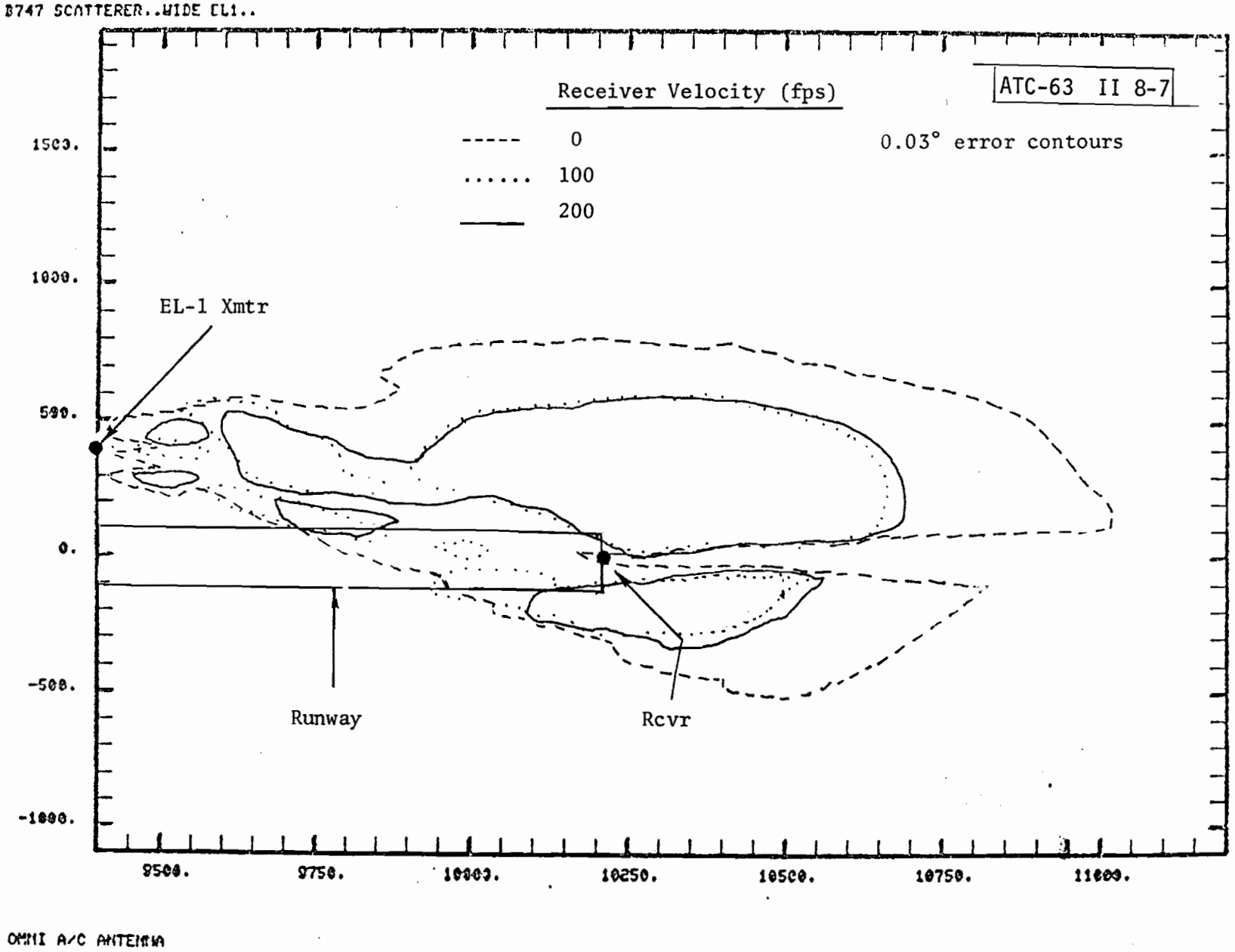

Fig. 8-7. Effect of receiver motion on basic wide aperture EL-1 system: error contours for B747 scatterer when receiver is at (10200, 0, 50).

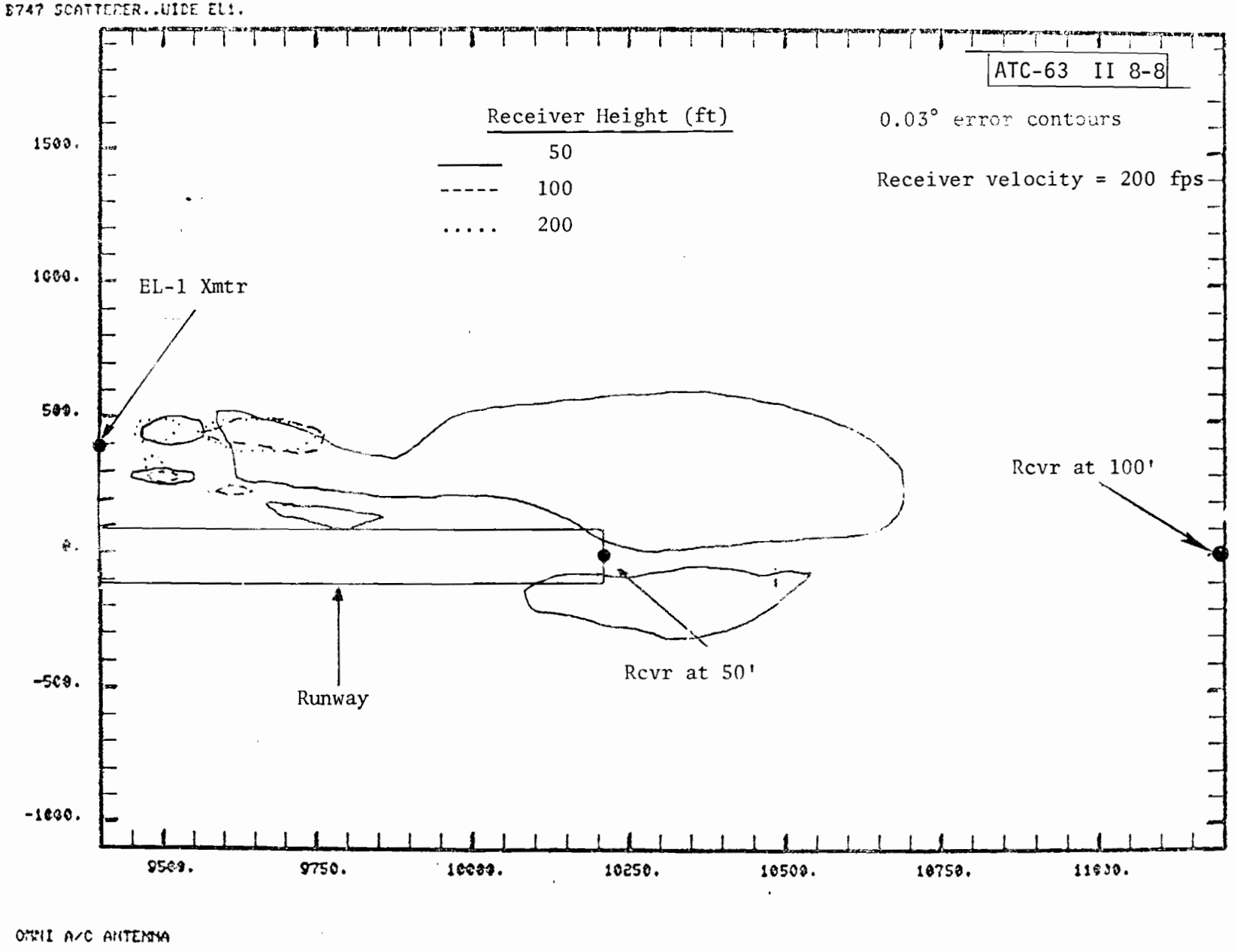

Fig. 8-8. Effect of receiver height on basic wide aperture EL-1 system: error contours for B747 scatterer.

pattern control will increase the effective multipath level for scatterers near zero azimuth when the receiver is at a wide azimuth angle. Thus, there may need to be a sensitive area for the EL-1 system in cases where EL-1 guidance is desired at wide angles on curved approaches, etc. Figure 8-9 shows the 0.09° error contours for several azimuths when the receiver is at a height of 1500 feet at 5 nmi range from GPIP (i.e., the receiver elevation angle is 2.86°). We see that these contours essentially coincide with the earlier contours for receivers on final approach, and hence do not represent a new constraint. For an aircraft at lower angles (e.g., 1.4°), the contours would extend outward for quite a considerable distance. This is to be expected since the separation angle between the top of the tail fin and the direct signal reaches 1° at a transmitter tail fin distance of 8300 feet.

(b) Basic Wide Aperture Azimuth System

This system was assumed to have a 1° beamwidth in the azimuthal plane with an elevation pattern rolling off at 6 dB/degree for elevation angles below +1.5°. Unless otherwise indicated, the transmitter phase center height was taken to be 6 feet.

First, we consider the error due to a truck or small building as modeled by a flat rectangular perfect conductor 15 feet high and 20 feet wide. Such a scatterer was found to yield errors as large as 0.03° only for cat III situations (i.e., aircraft altitudes below 50 feet). Figure 8-10 shows the 0.03° error contours for an aircraft nearing touchdown as a function of receiver motion and/or airborne antenna directivity. We see that the error contours extend out to two beamwidths for positions abreast the end of the

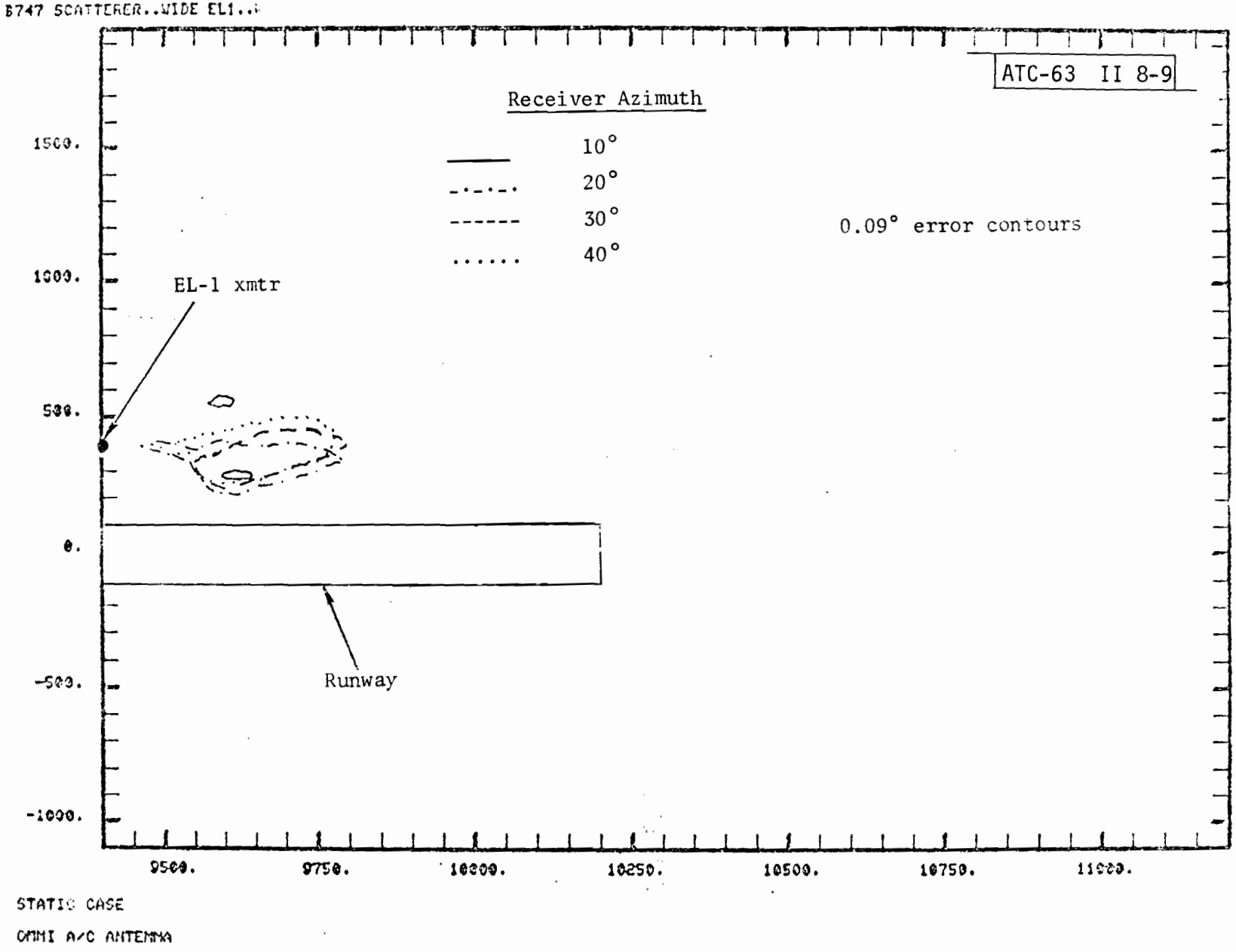

Fig. 8-9. Sensitivity to curved approach receiver azimuth for wide EL-1 system: error contours from B747 scatterer (2.82° elevation angle).

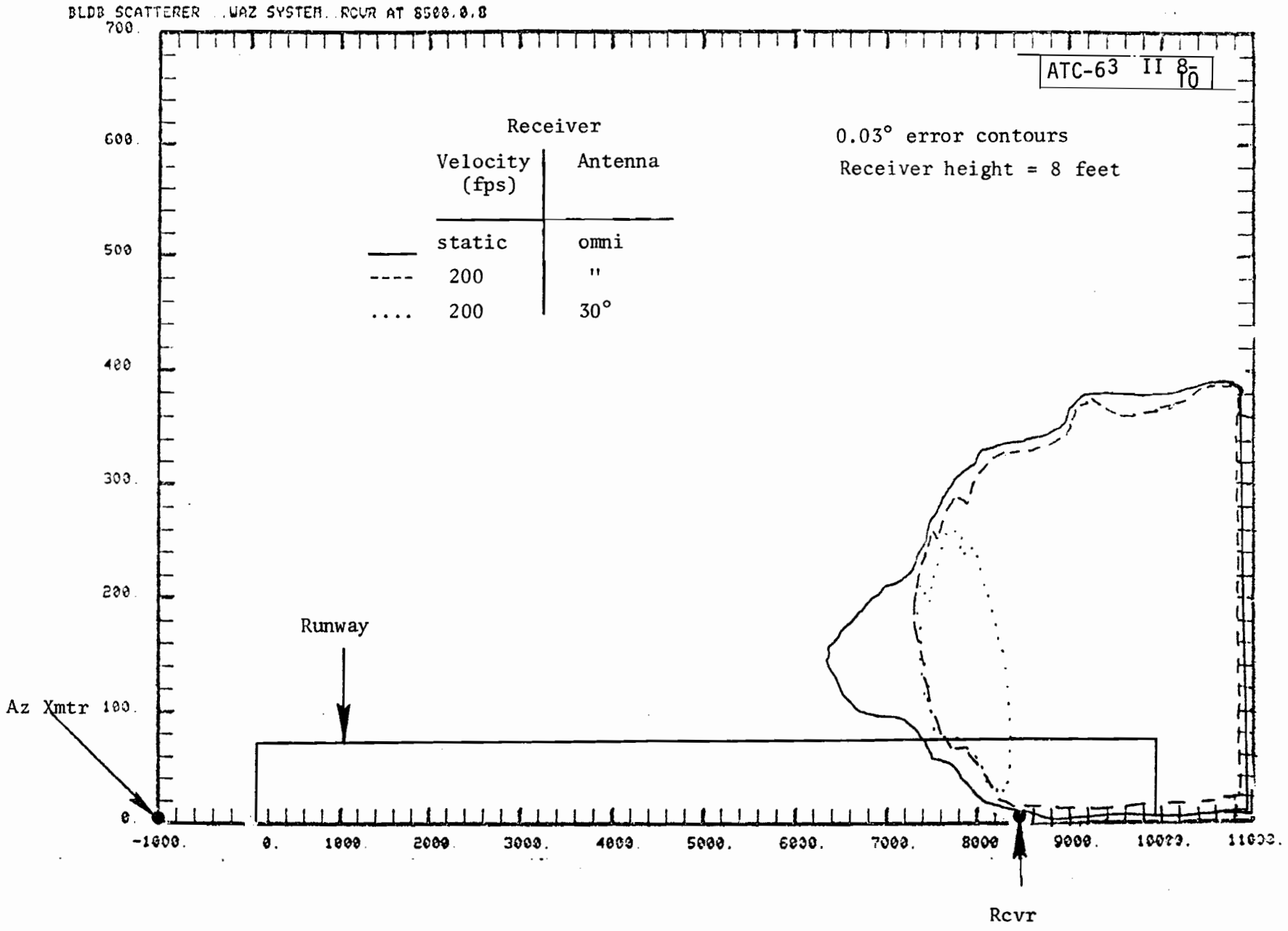

Fig. 8-10. Effect of receiver antenna pattern and/or motion on basic wide aperture azimuth error contours for 15 x 20 truck.

runway. This is to be expected, since an optimally oriented screen yields effective multipath levels ($\tilde{\rho}$) of close to unity at these points. For aircraft with a forward-looking horn, these errors probably will not be significant since the multipath region is quite small ($\approx$ 18 feet) for scatter positions whose x coordinate is less than that of the aircraft. However, for aircraft with nearly omni airborne patterns, the multipath region for truck locations before the runway threshold can be substantial (e.g., 1-2 seconds).

Reflections from Boeing 747 aircraft also yield the largest error contour region near the end of the runway, as shown in Fig. 8-11. The fuselage is the dominant source of errors for scatterer locations near the azimuth transmitter whereas the 60-foot high tail fin is the predominant error source for scatterer positions near the threshold. Motion averaging was found to make only a small change in the error contours. As in the case of trucks, a forward-looking airborne antenna can essentially reduce the error contour region at and beyond the threshold.

Figure 8-11 shows that aircraft scattering effects are substantial only at low altitudes. The prime reason for this is that at higher aircraft altitudes, the reflections from a tail fin located abreast the threshold pass beneath the receiver. Although fuselages scatter upwards such that specular reflections can be received over very long distances along a flight path,*

---

*e.g., George Ploussious [68] shows a case of a specular fuselage reflection from a B747 located abreast the GPIP occurring for some two thousand feet along the final approach.

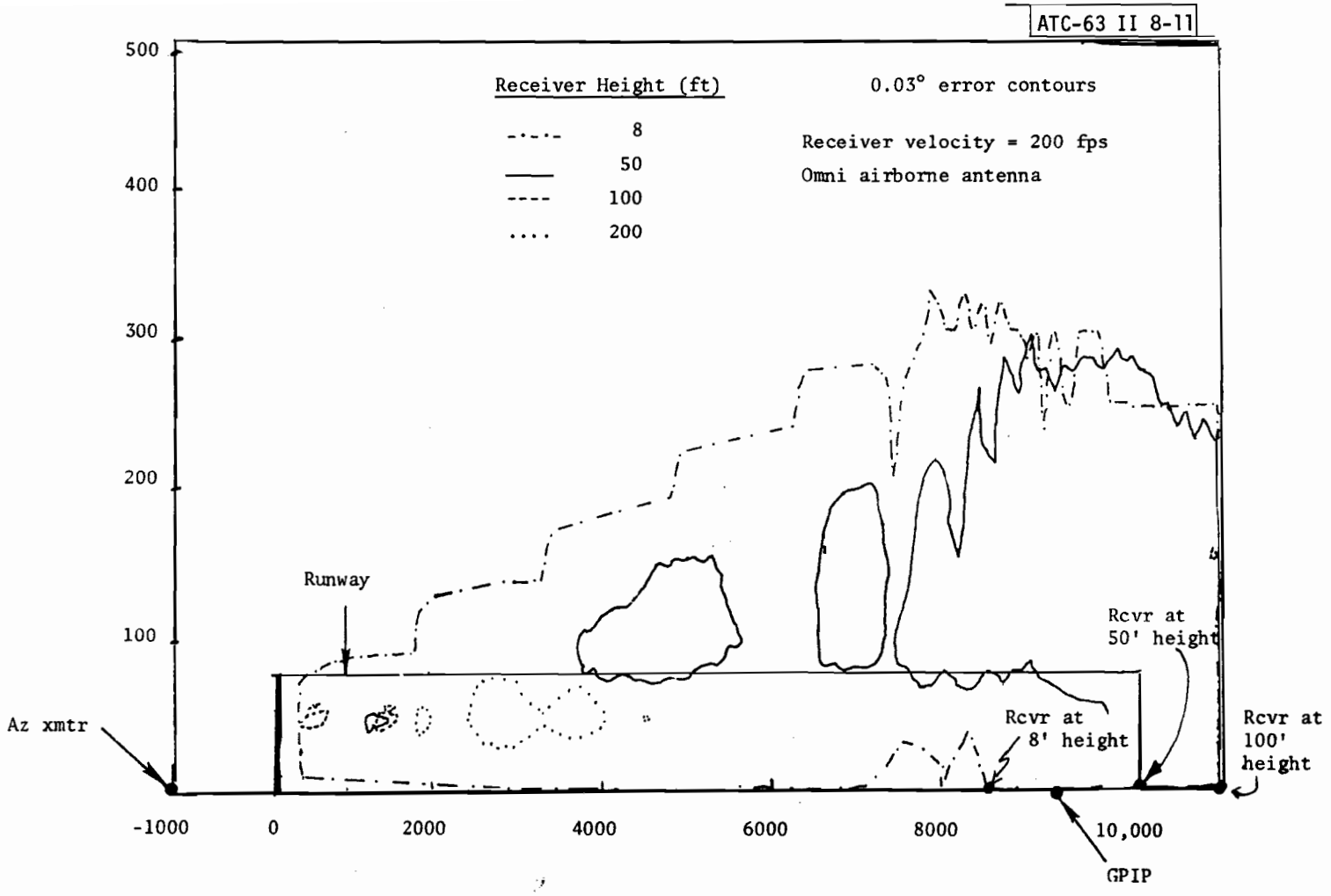

Fig. 8-11. Effect of receiver height on basic wide aperture error contours for B747 scatterer.

the effective multipath level ($\tilde{\rho}$) for scatter locations at the approach end of the runway is generally very low due to divergence, depolarizaion and cancellation by the secondary paths involving ground and fuselage reflection.

However, when the transmitter antenna must be elevated so as to clear obstacles at the end of a runway (e.g., the blast fence at JFK runway 4L), then the ground reflections can sharply increase $\tilde{\rho}$ by causing nulls in the effective direct signal. Figure 8-12 shows the error contours for a B747 scatterer at the first three nulls in the direct signal. Even though the transmitter antenna has a sharp cutoff at the horizon, the receiving aircraft elevation on angle with respect to the azimuth transmitter* is small (less than 1°). Thus, the error contours are substantially larger than those of Fig. 8-11.

Receiver lateral and vertical displacements of 0.25° around the nominal glide slope at the cat II decision height of 100 feet were found to make only very slight changes in the error contours.

The cases to date have considered only a B747 aircraft, which is known to be extreme in terms of fuselage and tail fin sizes. Figure 8-13 compares the error contours at a receiver height of 50 feet for the B747 and the very common B727. We see that the B727 contour is very much smaller. For points near the threshold, the tail fin reflections from the B727 aircraft pass

*It might be noted that this nulling effect does not arise to the same degree with the ILS localizer due to the large wavelength (e.g., for a 20-ft phase center height, MLS has a first null at 0.28° elevation angle whereas ILS would have a first null at 14° elevation angle).

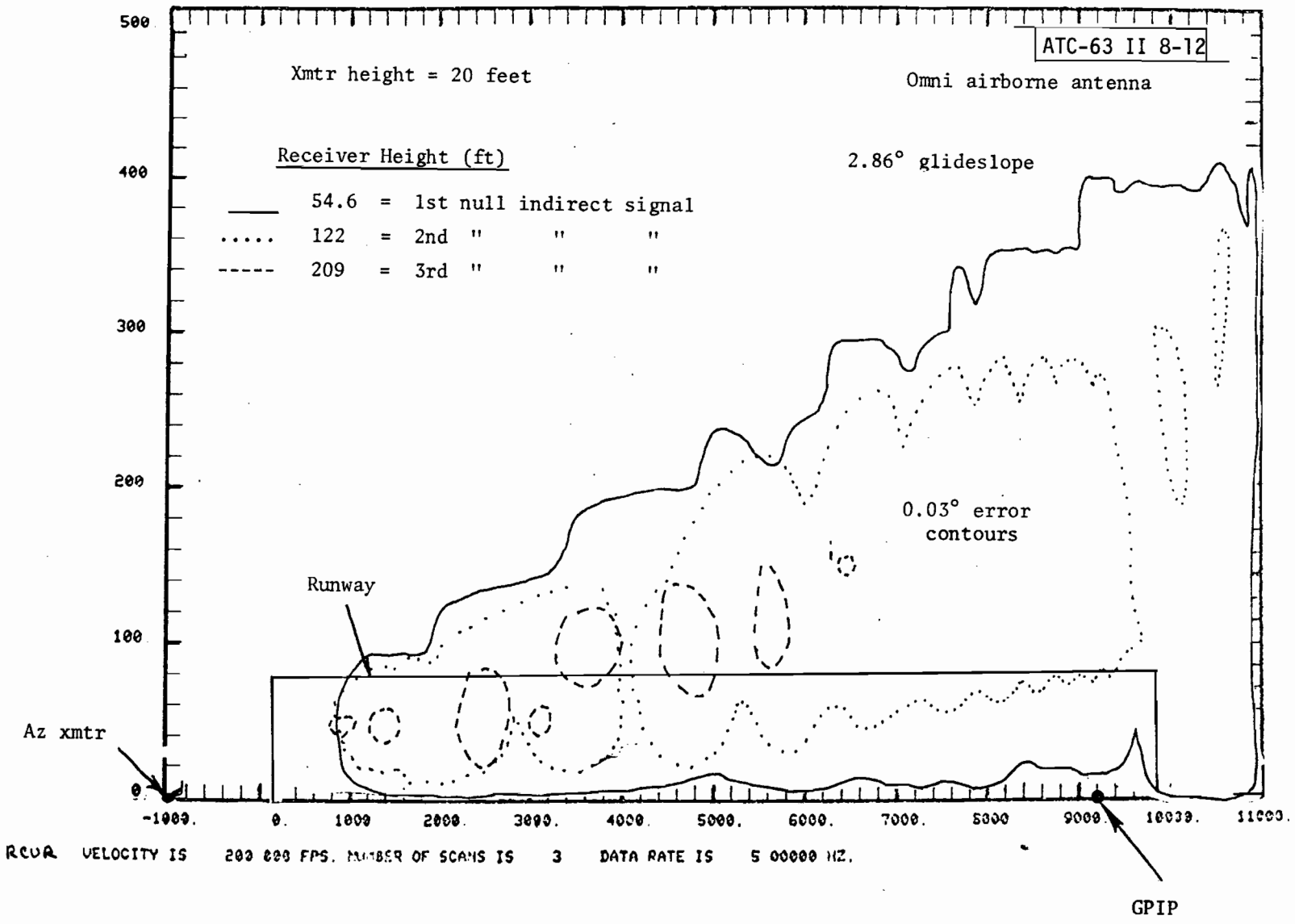

Fig. 8-12. Effect of transmitter height on basic wide aperture error contours for B747 scatterer.

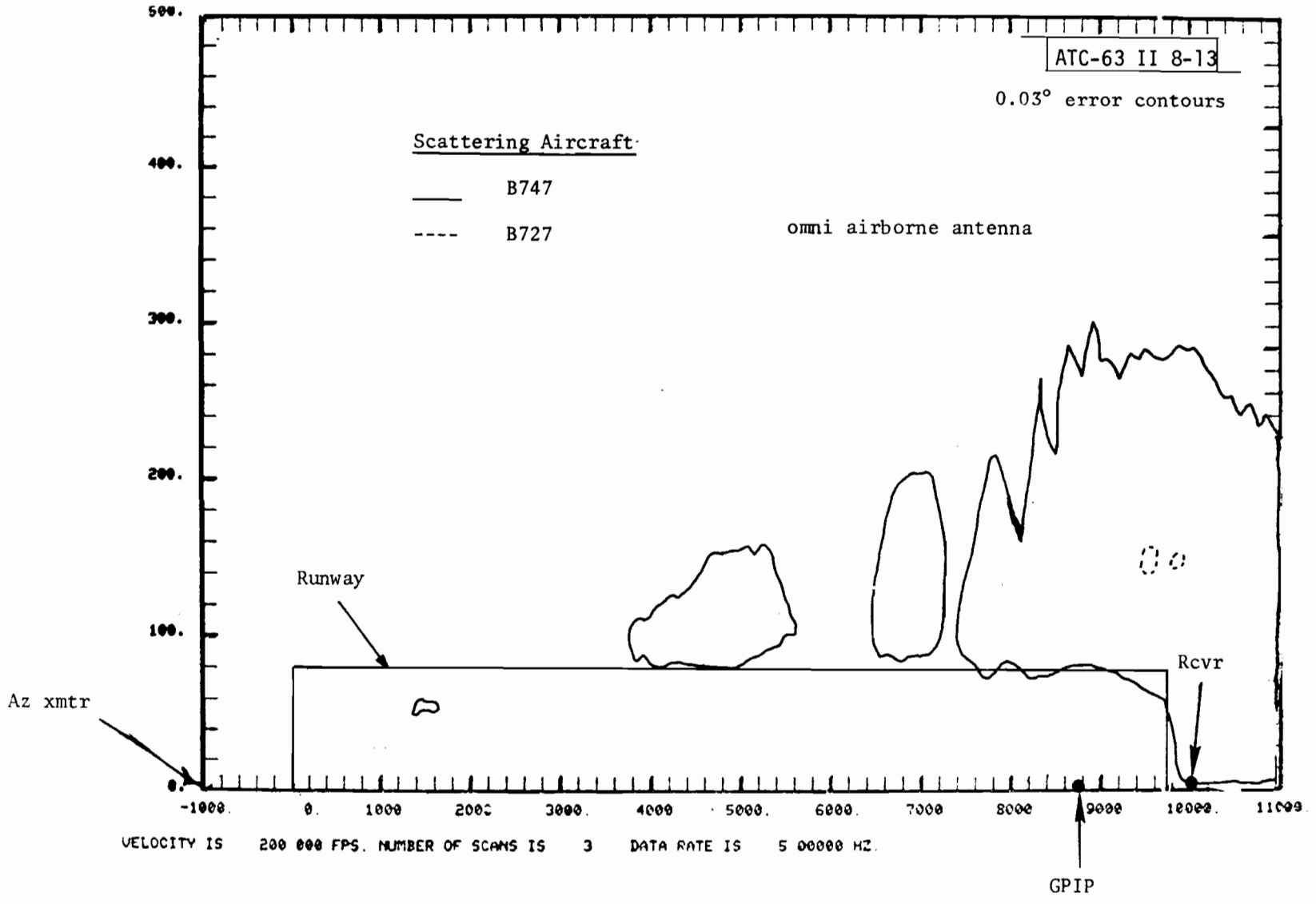

Fig. 8-13. Effect of scattering aircraft type on basic wide aperture azimuth error contours at 50-foot altitude.

under the receiver whereas the B747 tail yields significant multipath. At the middle of the runway, the B747 fuselage yields errors, but the B727 fuselage levels are lower due to (1) the smaller fuselage radius (≈ 3 dB), and (2) (2) greater cancellation by ground/fuselage reflections.

(c) Basic Narrow Aperture Elevational System

This system was modeled as having a 1.5° beamwidth in the elevation plane and the same azimuthal pattern as the basic wide EL-1 system. The antenna phase center height was taken to be 10 feet above the local flat terrain with a 400-foot offset from centerline and a location 200 feet forward of the GPIP.

Since the basic narrow system is to be used primarily on short runways, one expects scattering aircraft to be almost exclusively narrow bodied. In Fig. 8-14, we show the 0.03° error contours for a B727 scatterer at various receiver heights. At 50-foot height, the 0.03° contour is considerably greater than the EL-1 transmitter contours discussed earlier. For greater receiver heights, we see from Fig. 8-14 that the region of 0.03° error contours decreases to a small rectangular patch extending some 250 feet forward and approximately 100 feet to either side of the EL-1 antenna. This rapid decrease occurs because the B727 tail fin reflections pass below the receiver at the greater heights even though the tail fin is still inbeam by the conventional criteria of two beamwidths. As was the case with the wide EL-1 antenna, using a directional airborne antenna sharply reduces the region of significant errors to a small region in front of the EL-1 antenna.

If, however, large aircraft such as a B747 might be found near the threshold of a runway with a basic narrow EL-1 system, then the critical area

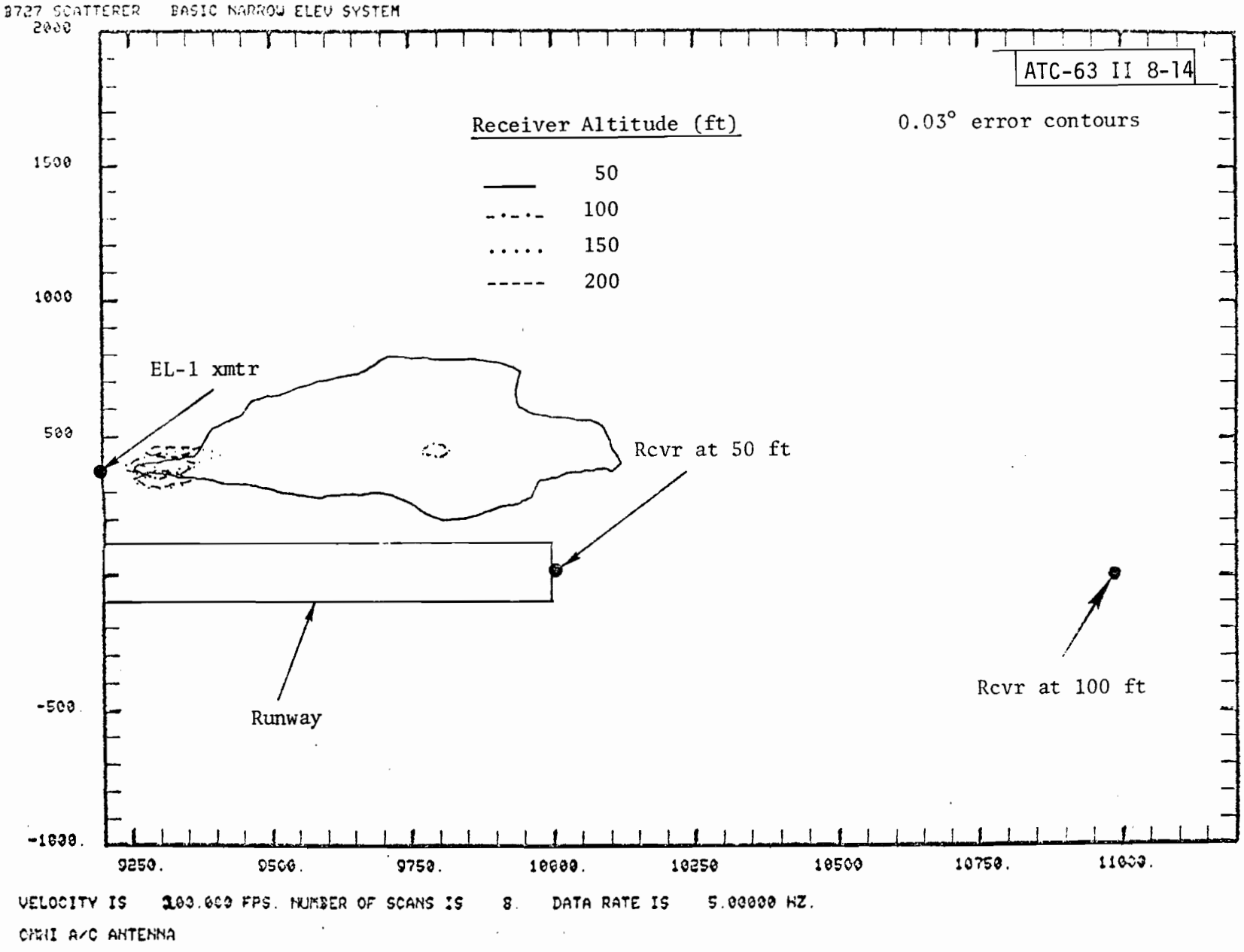

Fig. 8-14. Effect of receiver height on basic narrow EL-1 error contours for B727 scatterer.

would probably have to be increased. In Fig. 8-15, we compare the 0.03° error contours for B747 and B727 scatterers when the receiver is at 100 feet. We see that the B747 tail fin generates a very much larger error contour. Comparing Fig. 8-15 with Fig. 8-8, we see that increasing the beamwidth 50% has extended the B747 0.03° error contour forward approximately threefold. This high degree of sensitivity shows the difficulty of extrapolating MLS multipath performance by simple rules of thumb such as "halving aperture doubles the errors."

(d) Basic Narrow Aperture Azimuth System

This system was assumed to have a 2° beamwidth in the azimuth plane with an elevation pattern rolling off at 6 dB/degree for elevation angles below 1.5°. The transmitter height was assumed to be 6 feet, with the equipment sited 1000 feet behind the stop end of a 7000-foot runway. In all cases, the landing aircraft was assumed to be on a 2.86° glide slope.

Figure 8-16 considers the case of a truck scatterer for a receiver at 50 feet. Whereas with the wide aperture azimuth system, there were no nonrunway locations within the 0.03° error contour, in this case there is one region behind the receiver where the error exceeds 0.03°. Analysis shows that the peak multipath in this region is approximately -17 dB at a separation angle of 1 beamwidth, enough to generate errors > 0.03°. If a wide azimuth system were in use, the separation angle would be 2 beamwidths and the error < 0.03°. At greater heights, the 0.03° errors due to trucks did not include any off runway locations.

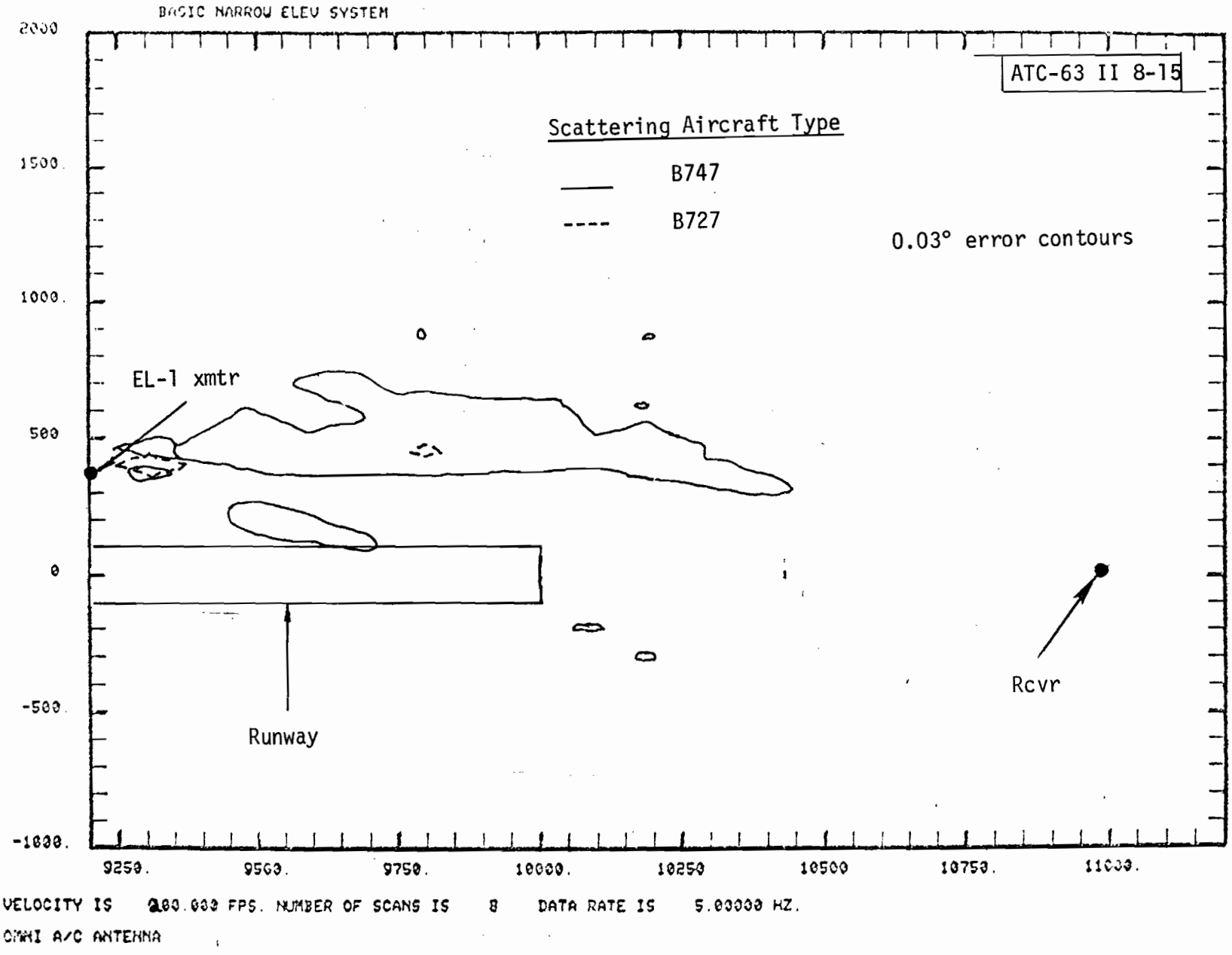

Fig. 8-15. Effect of scattering aircraft type on basic narrow EL-1 error contours at 100-foot altitude.

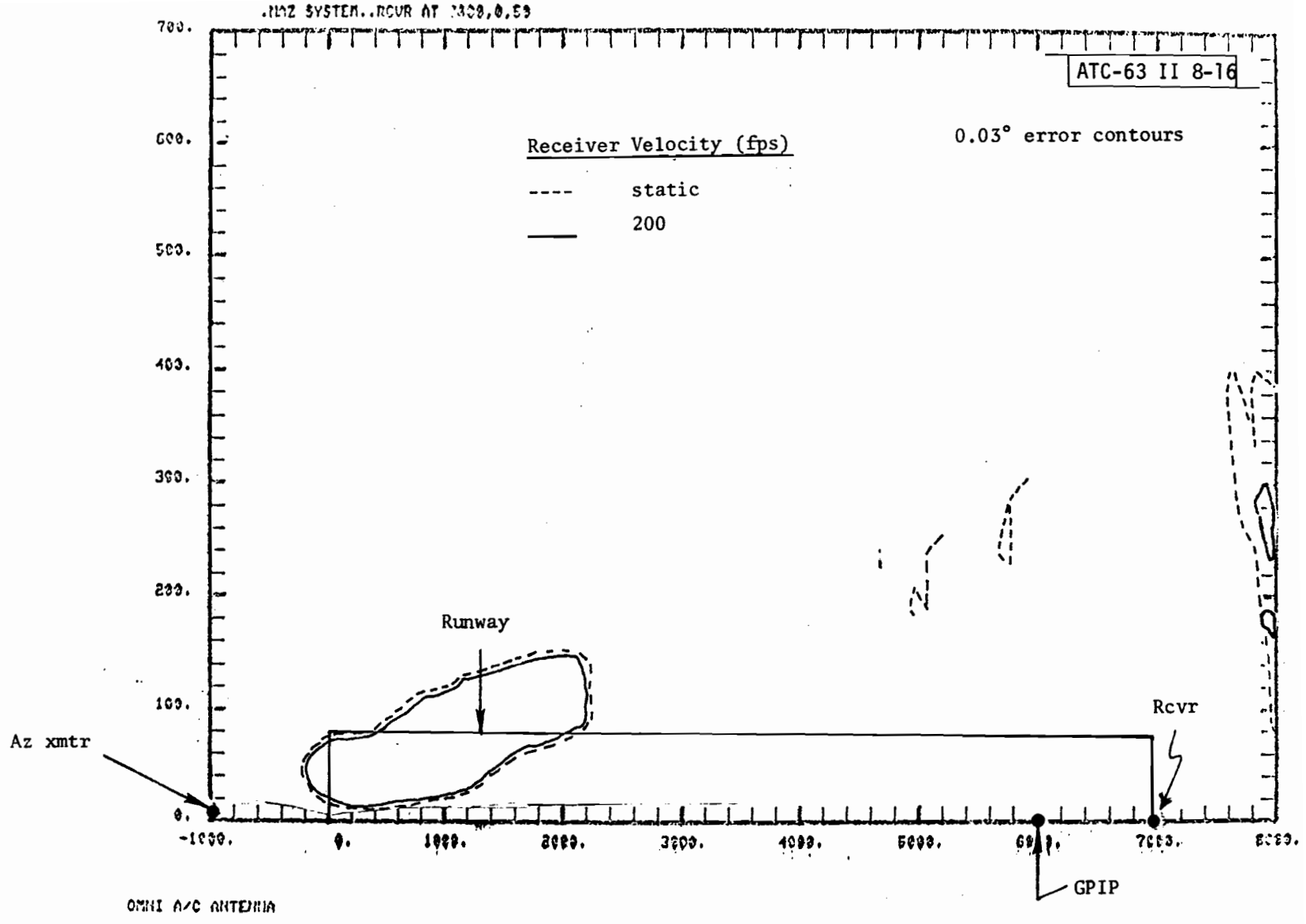

Fig. 8-16. Effect of receiver motion on basic narrow Az error contours for truck scatterer at receiver height of 50 ft.

Figure 8-17 shows the 0.03° error contours for a receiver at several heights. The principal error contours at 100 feet receiver altitude are from positions abreast the scattering aircraft. These evidently arise from fuselage reflections which are scattered upwards to the receiver. At these locations, the scattering aircraft is rotated inward ≈ 45°, so that the errors would persist over ≈ 70 feet along the flight path. For a receiver at 50 feet, the tail fin reflections yield a significant increase in the 0.03° error contour. Note that although the runway is shorter than in the wide azimuth studies, the error contours for B727 is almost as large as the wide azimuth B747 contour. This is because the wider beamwidth makes twice as large a region in-beam and also makes the errors twice as large at a given normalized separation angle.

If B747 aircraft could be found near the threshold of a narrow azimuth system, we see from Fig. 8-18 that a fairly substantial critical area may be needed for cat I/II operation.

8.3 Approach to Full Run Analysis

The objective was to make a preliminary set of full simulations for comparison with the contour program results. In the next phase of the program, a much larger number of full simulations will be performed to refine the estimates of this initial study. Thus, attention was focused on CTOL approaches at 200 feet per second approach velocity along a 2.86° (20:1) glide slope. The evaluation points for azimuth and elevation were spaced every 40 feet, corresponding to a 5 Hz data rate.

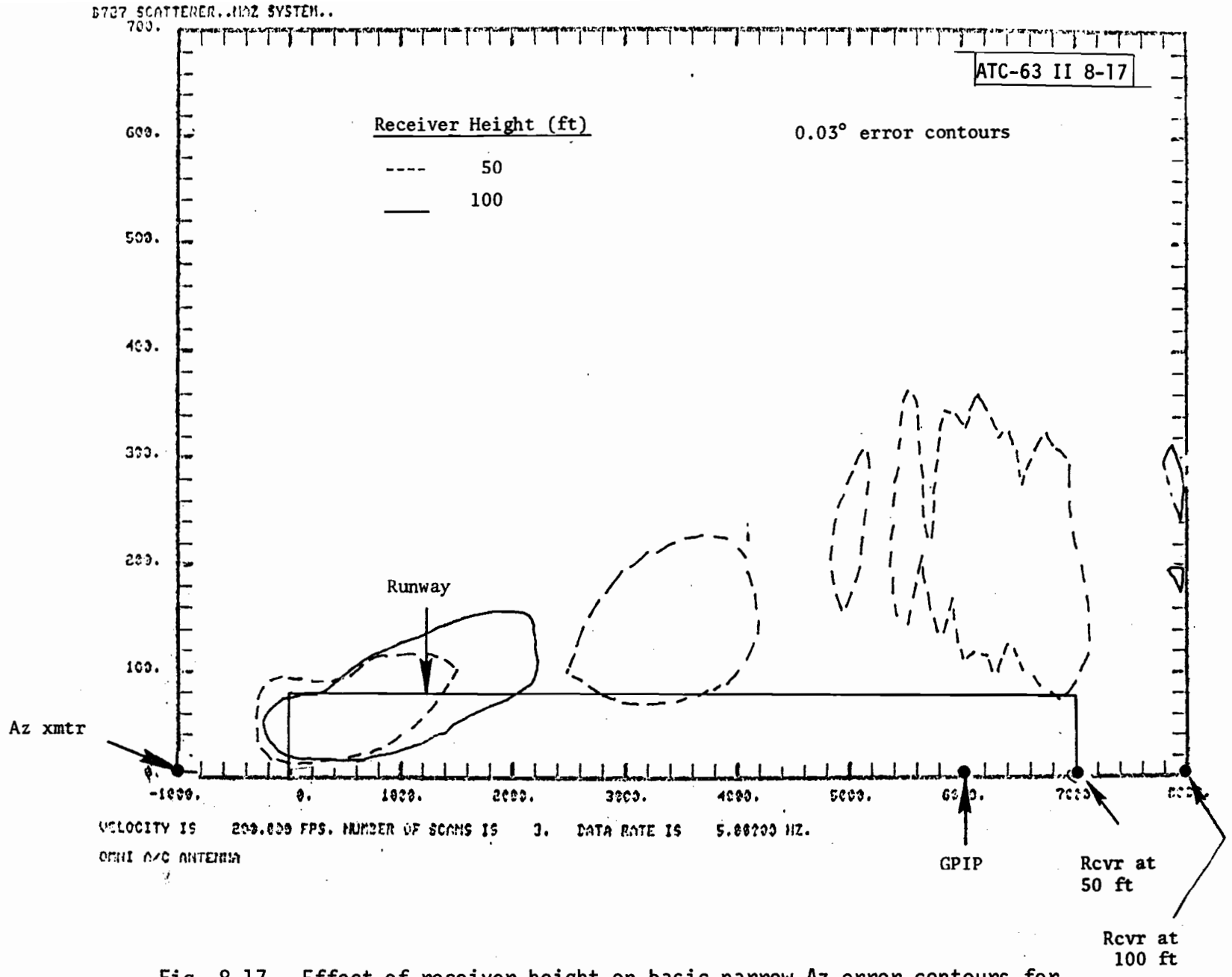

Fig. 8-17. Effect of receiver height on basic narrow Az error contours for B727 scatterer.

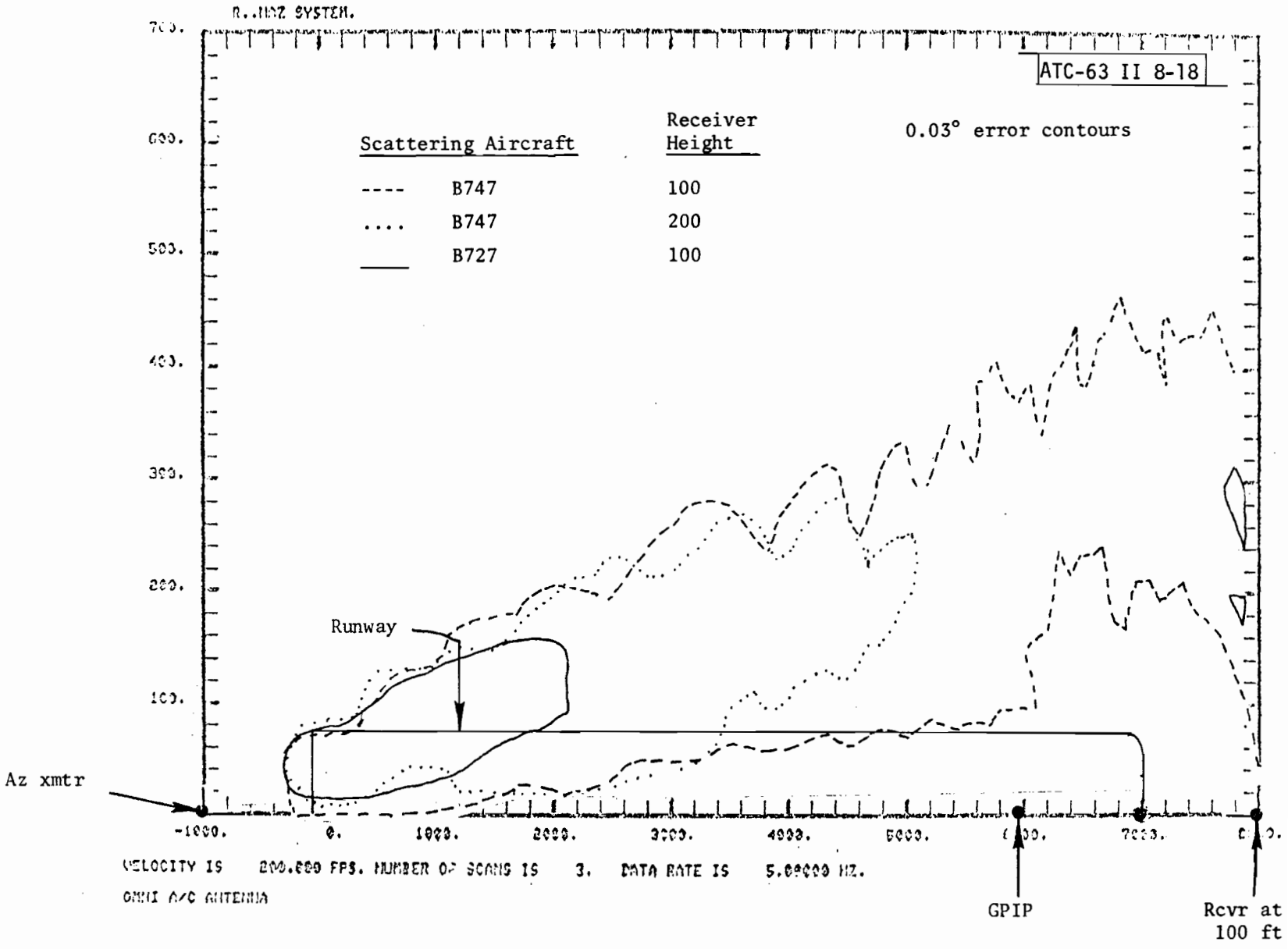

Fig. 8-18. Effect of scattering aircraft type on basic narrow Az error contours.

For the basic narrow studies, the flight path was taken to be a straight line parallel to the CL passing through the GPIP. For the basic wide studies, the aircraft flew along the basic narrow path down to 50 feet, and then immediately transitioned to a second line segment which terminated 8 feet above runway CL 1500 feet down the runway from threshold.

The aircraft locations were chosen so as to

(1) yield multipath at a number of different receiver altitudes

(2) have "plausible" locations which lie within or near appropriate error contours determined in the preceding section.

In nearly all cases, the "worst case" aircraft orientations were fairly close to parallel to runway centerline. Such an orientation would at most airports correspond to an aircraft on a parallel taxiway.

ICAO calls for a 300-foot separation of parallel taxiways from runway centerline in all cases, while the FAA permits a 250-foot separation at "local" airports* with a 400-foot separation required at all larger airports [61]. To meet the data needs for the ICAO submission, the initial phase has considered primarily aircraft whose center is located at least 300 feet off the runway centerline. In the case of elevation system critical areas, it was assumed that scattering aircraft locations whose offset from centerline was less than that of the EL-1 system would be banned from at least the first thousand feet in front of the EL-1 transmitter to avoid excessive shadowing errors.

*"Local" airports serve local service routines of the short haul variety normally not exceeding 500 miles.

8.4 Full System Run Results

(a) Basic Wide Aperture System Runs

Figure 8-19 shows the computer generated airport map for a basic wide aperture critical areas run with eight B747 aircraft scatterers. In Fig. 8-20, we relate these aircraft positions to the basic wide aperture system error contours. The information plotted out below the computer map in Fig. 8-19 shows that the peak multipath levels were encountered at the expected heights.

Figures 8-21 and 8-22 plot the level and separation angle of the largest six multipath components everywhere along the flight path. In the case of the azimuthal multipath, aircraft A1 and A5 do not appear on these plots because their levels were lower than that of aircraft A7 and A8. We see that all the aircraft have azimuthal separation angles of at least 1.5 beamwidths and multipath levels below -10 dB; hence we can expect the errors to be fairly small.

In the case of the elevation multipath, we see that the aircraft reflections are generally inbeam with levels between -8 dB and -16 dB. The abrupt changes in separation angle occur when the largest component from an aircraft switches from being a fuselage reflection to being a tail reflection. For aircraft which are quite close to the EL-1 transmitter (e.g., aircraft A6 and A7), fuselage reflections appear at positive separation angles even with the conical beams because the surface curvature causes most of the reflections to occur at the fuselage midpoint independent of the receiver position.

The angular errors along the flight path are shown in Fig. 8-23. The azimuthal errors are seen to be quite small. This suggests that the error contour plots are conservative with respect to the azimuth errors. This

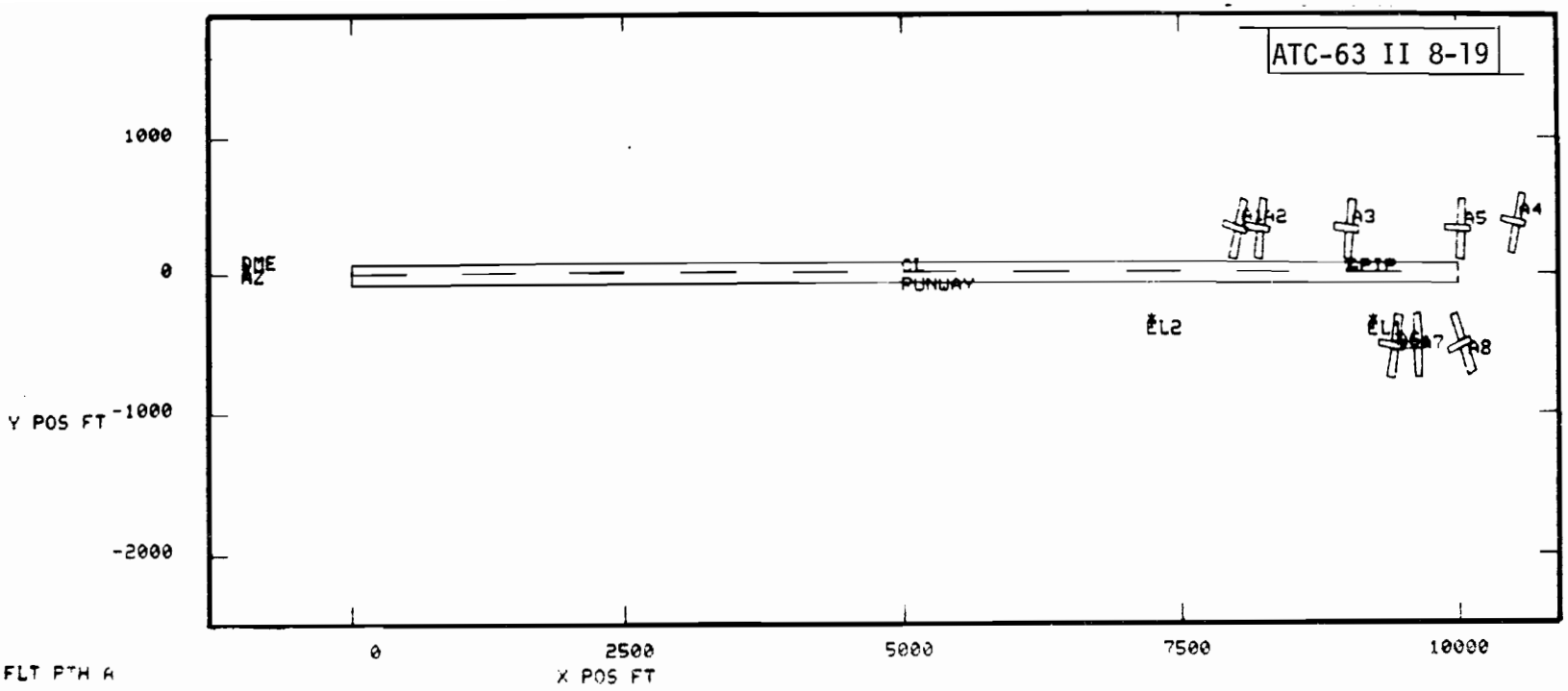

FLT PTH A

AZ SYSTEM

OBST	RANK	AMP	ALT	RDOP
G	1	-2	45 5	0
A1	7	16	9 0	-143
A2	4	14	26 8	-35
A3	2	12	49 5	-29
A4	5	15	101 9	-96
A5	8	19	60 0	-144
A6	9	67	233 8	-399
A7	6	16	54 0	-158
A8	3	13	46 5	-725

EL SYSTEM

OBST	RANK	AMP	ALT	RDOP
G	1	0	21 8	0
A1	3	9	14 9	-35
A2	9	28	48 5	-234
A3	8	21	47 5	-23
A4	6	13	111 9	-47
A5	7	20	197 8	0
A6	2	8	147 9	-5
A7	4	10	127 9	-15
A8	5	12	60 0	-231

AZ critical areas a/c

EL critical areas a/c

RANK = ranking by multipath level

AMP = ratio (in dB) of direct signal to largest multipath level of the given scatterer

ALT = receiver altitude (in ft) when largest multipath occurred

RDOP = scalloping rate (in Hz) when largest multipath occurred

Fig. 8-19. Airport map for study #W1 of basic wide aperture TRSB critical areas.

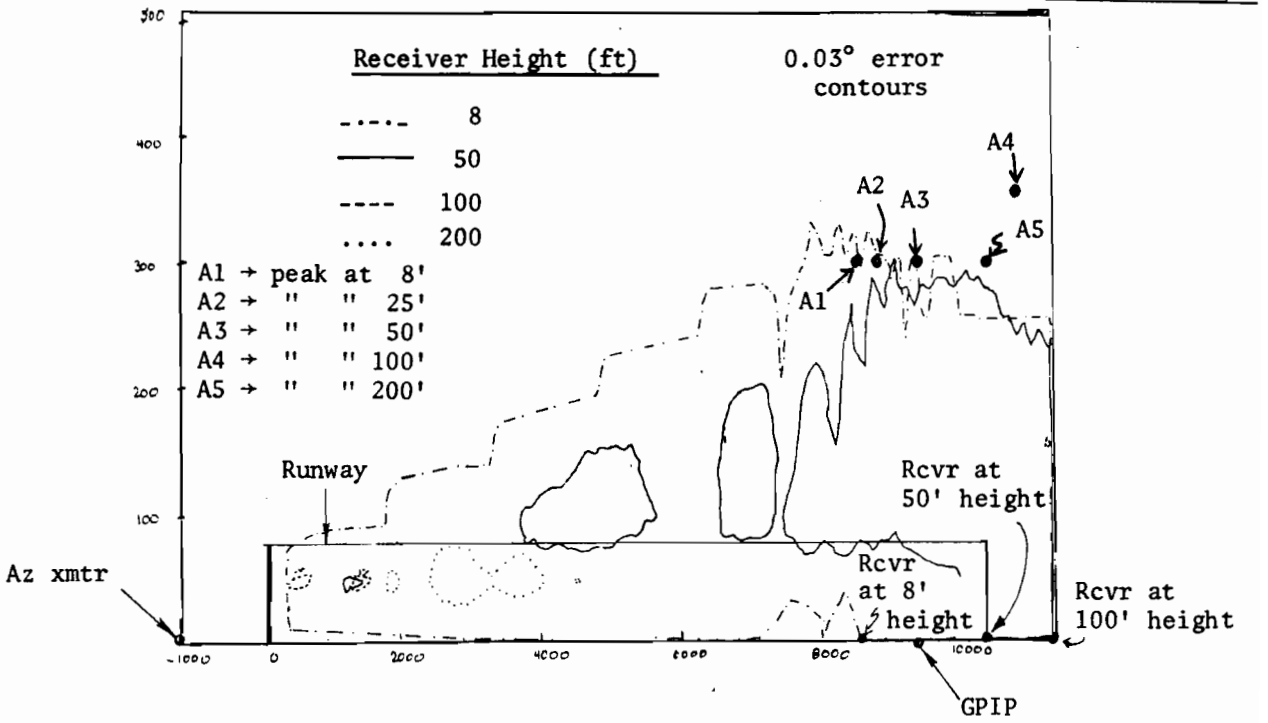

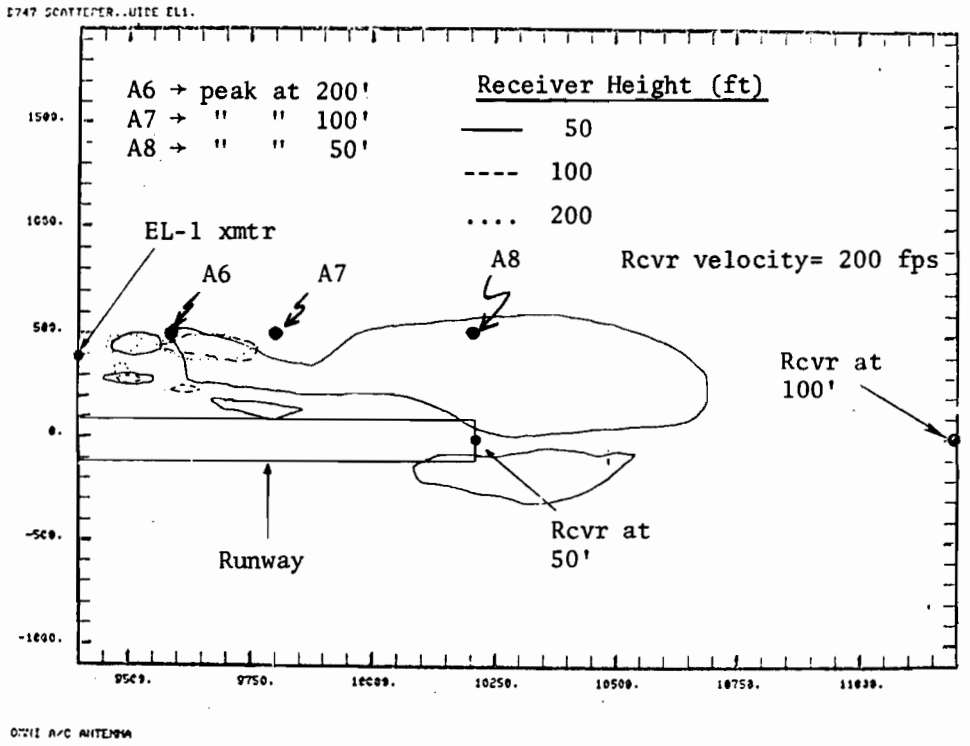

Fig. 8-20. Relation of study #W1 aircraft positions to basic wide aperture system error contours.

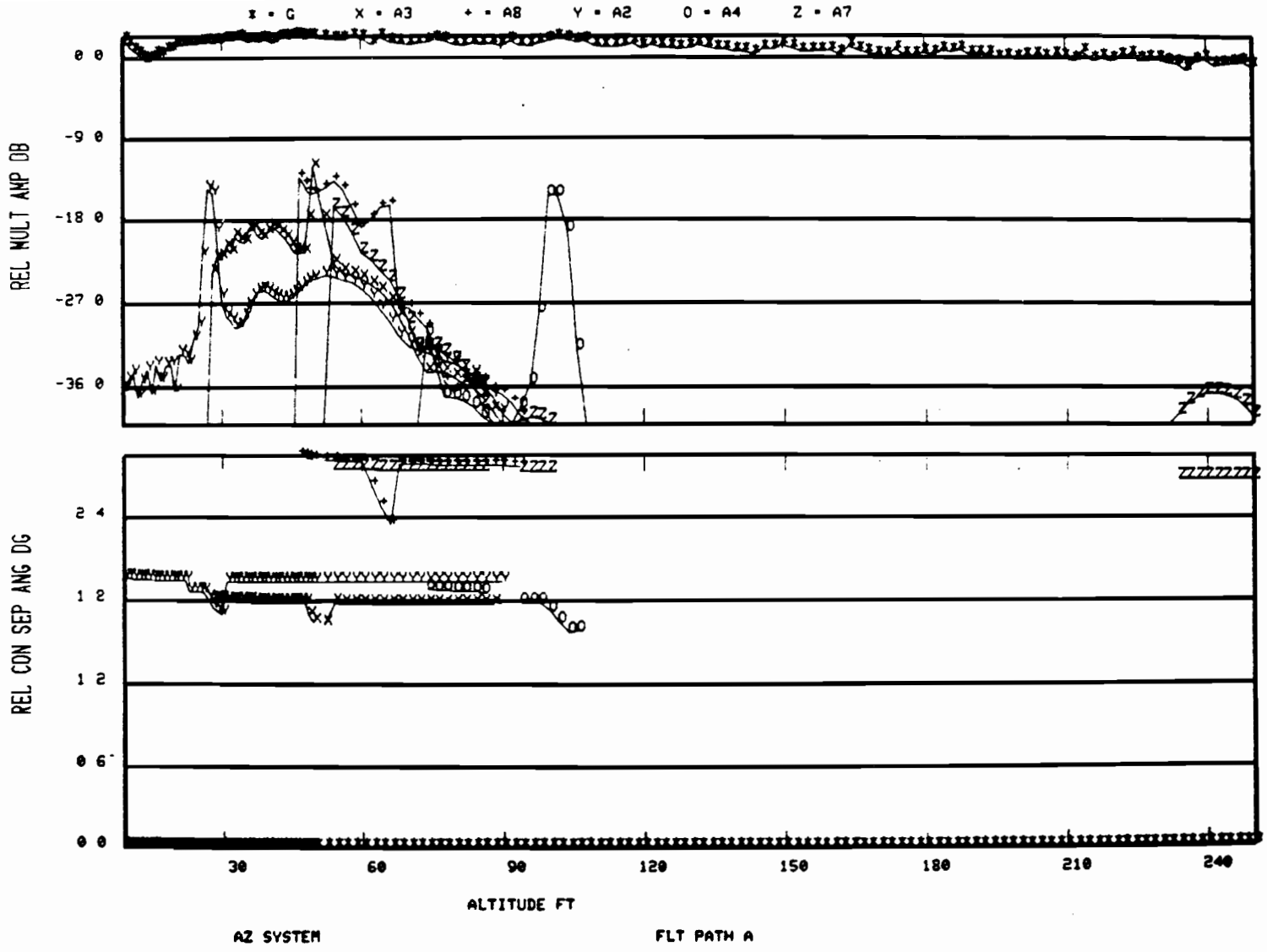

Fig. 8-21. Multipath diagnostics for basic wide aperture azimuth study #W1.

ATC-63 II 8-21

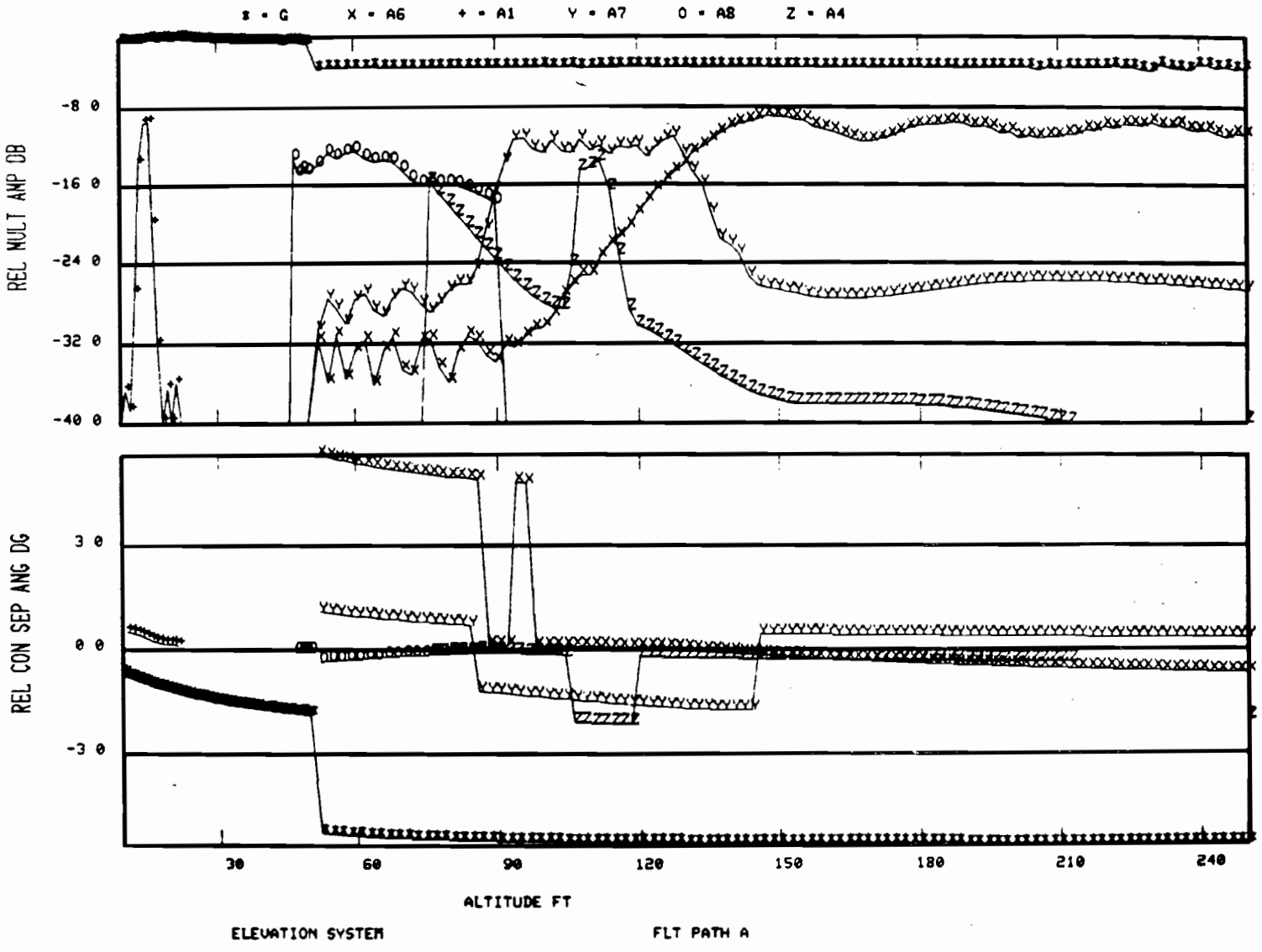

Fig. 8-22. Multipath diagnostics for basic wide aperture EL-1 study #W1.

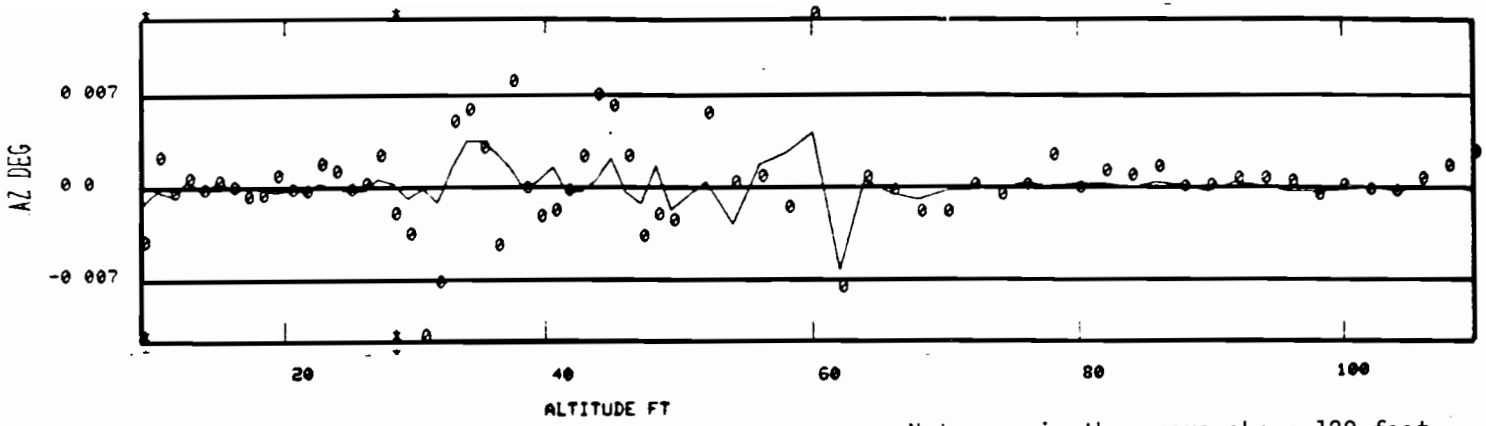

Note: azimuth errors above 120 feet were generally less than 0.005° static and 0.001° dynamic

0 = zero aircraft velocity (static) error

— = dynamic error

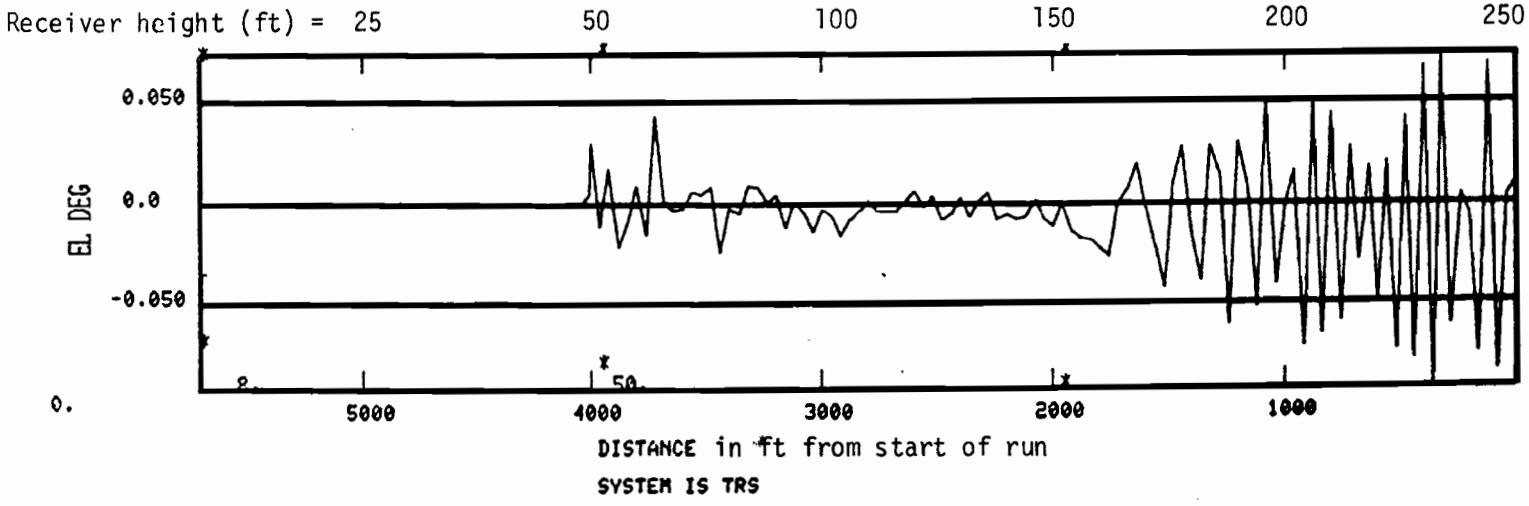

ATC-63 II 8-23a

Fig. 8-23a. Angular errors along flight path for basic wide aperture study #W1.

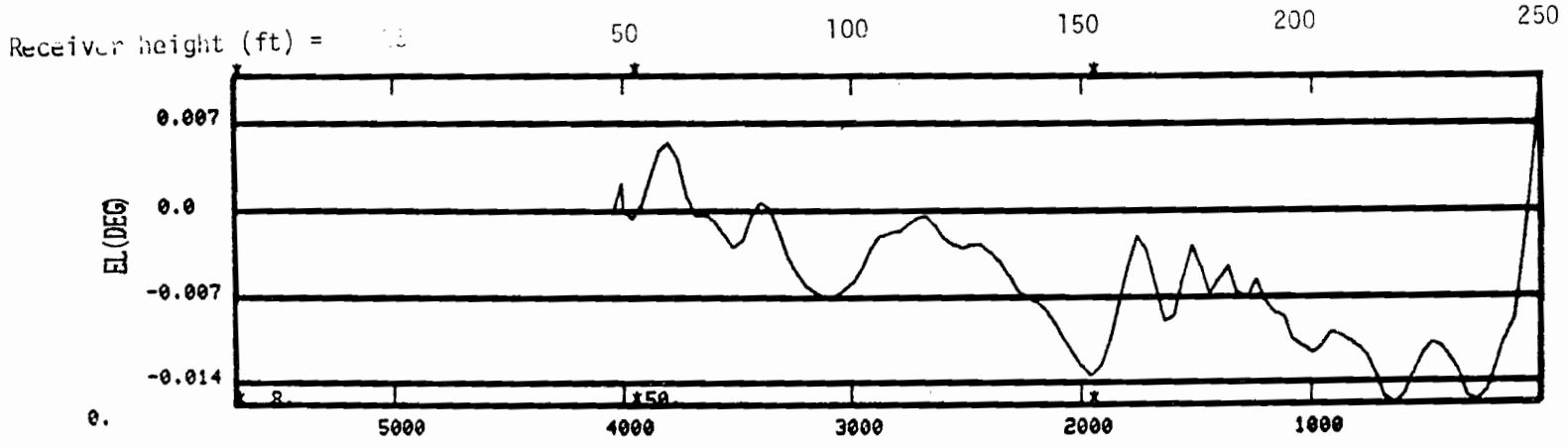

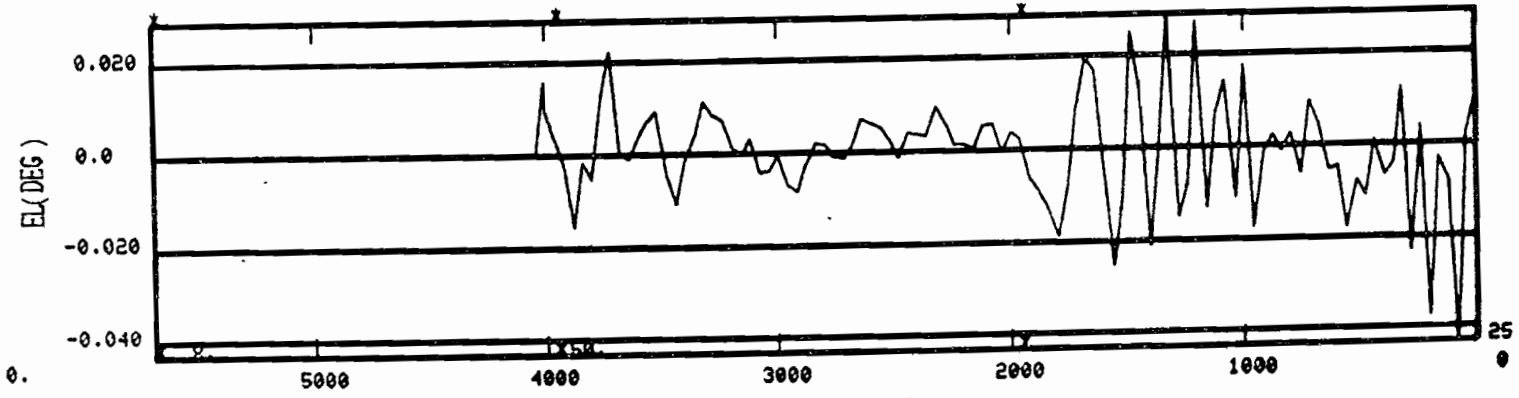

Fig. 8-23b. Path following and control motion EL1 errors for basic wide aperture #W1.

is felt to arise from the "worst case" summation of the various multipath components.

On the other hand, the elevation errors encountered agree much more closely with the contour plots. The nearly constant error at altitudes above 180 feet is due to aircraft A6. From the airport map data, we note that the scalloping rate for this aircraft reaches 5 Hz at 150-foot altitude. This suggests that the reduction in error near 180-foot altitude represents the commencement of effective motion averaging (or, the end of the first grating lobe). The short duration EL-1 error near 60 feet is believed to be a higher order grating lobe.

In Fig. 8-23b, we show the result of passing the elevation error signal of Fig. 8-23a through the "path following" and "control motion" filters used in the U.S. MLS program to emulate aircraft flight control systems. The path following output is a factor of 2 below the current MLS requirement of 0.1°, while the control motion errors are fairly close to the requirement of 0.05° 2σ. It is worth noting that with an ILS, the errors in this situation would have a spatial frequency (1/15) of that for TRSB and hence, be primarily path following as opposed to control motion.

In view of the quite low azimuthal errors when the scattering aircraft were at the outer boundary of the 0.03° error contour, a second azimuth full run was made with three scattering aircraft located in the middle of the error contours, as shown in Fig. 8-24. Since there were significant error contours only for aircraft altitudes $\leq$ 50 feet, this second run commenced at 60-foot altitude. Figure 8-25 shows the airport map for this case, while Fig. 8-26 shows the azimuthal multipath amplitude and separation angles. We observe substantially higher multipath levels with separation angles less than 1 beamwidth. Thus, we expect substantial errors in the azimuth function.

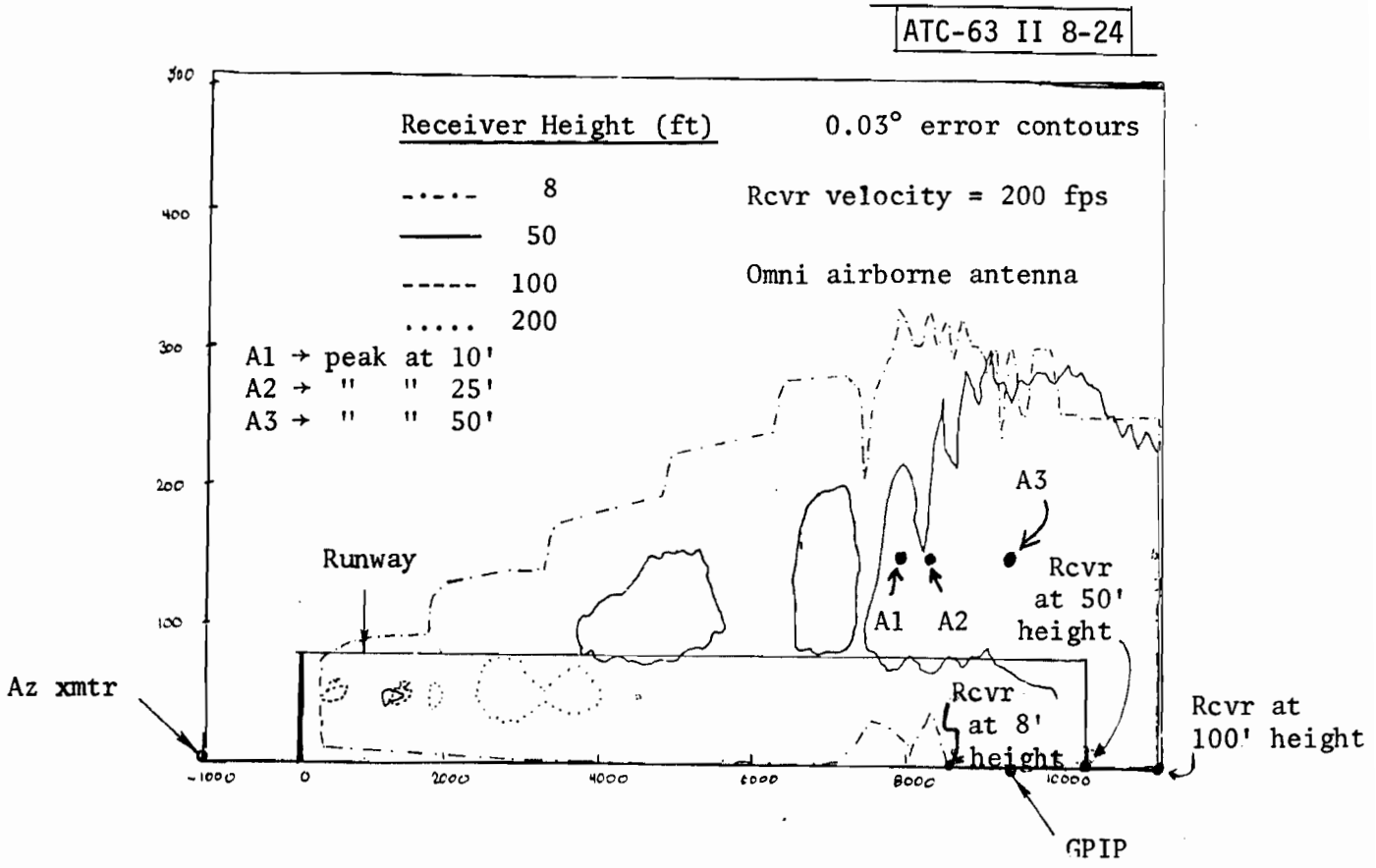

Fig. 8-24. Relation of scattering B747 aircraft positions for study #W2 to basic wide aperture azimuth error contours.

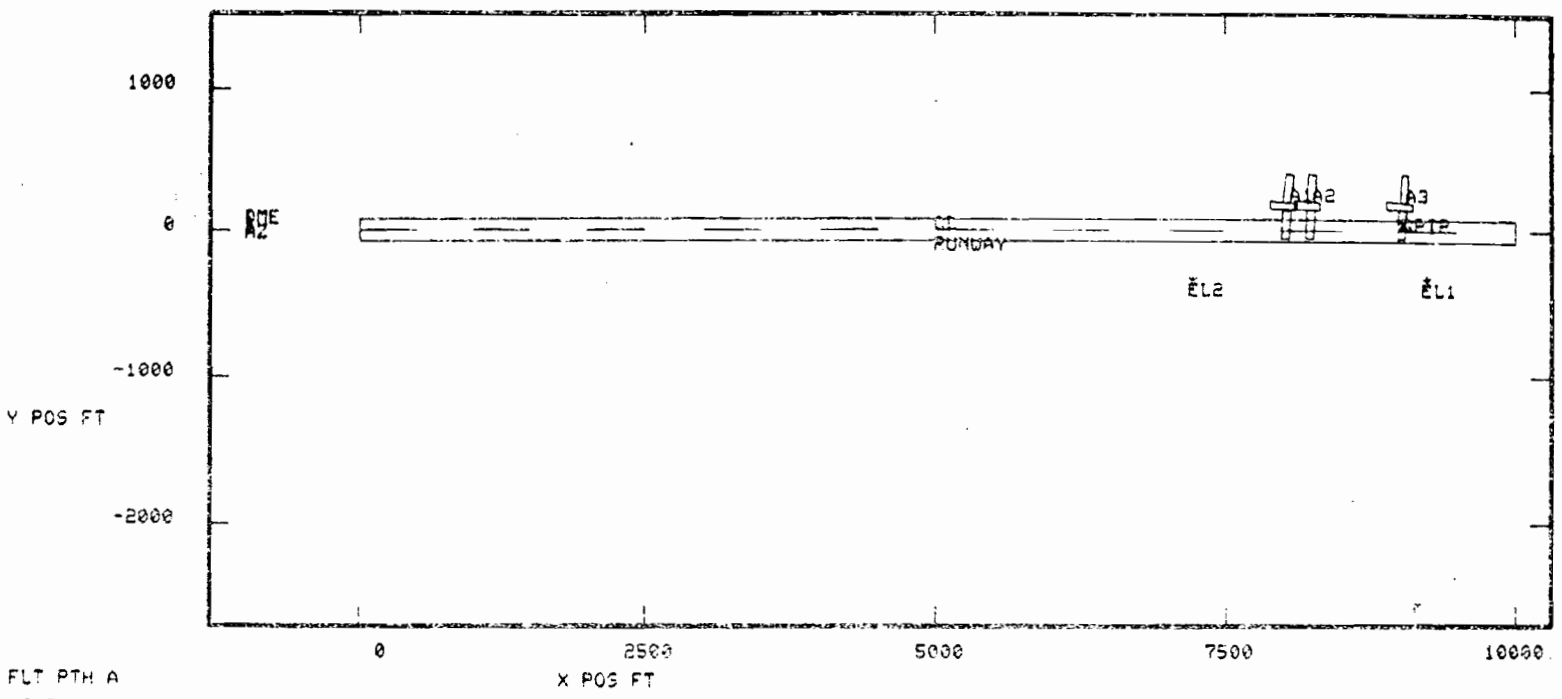

FLT PTH A
AZ SYSTEM

OBST	RANK	AMP	ALT	RDOP
G	1	-2	49 4	0
A1	2	10	14 7	-17
A2	4	11	23 3	-9
A3	3	11	49 4	-10
D	5	80	60 0	0

RANK = ranking by multipath level

AMP = ratio (in dB) of direct signal to largest multipath level of the given scatterer

ALT = receiver altitude (in ft) when largest multipath occurred

RDOP = scalloping rate (in Hz) when largest multipath occurred

Fig. 8-25. Airport map for study #W2 of B747 scatterers for basic wide aperture azimuth system critical areas.

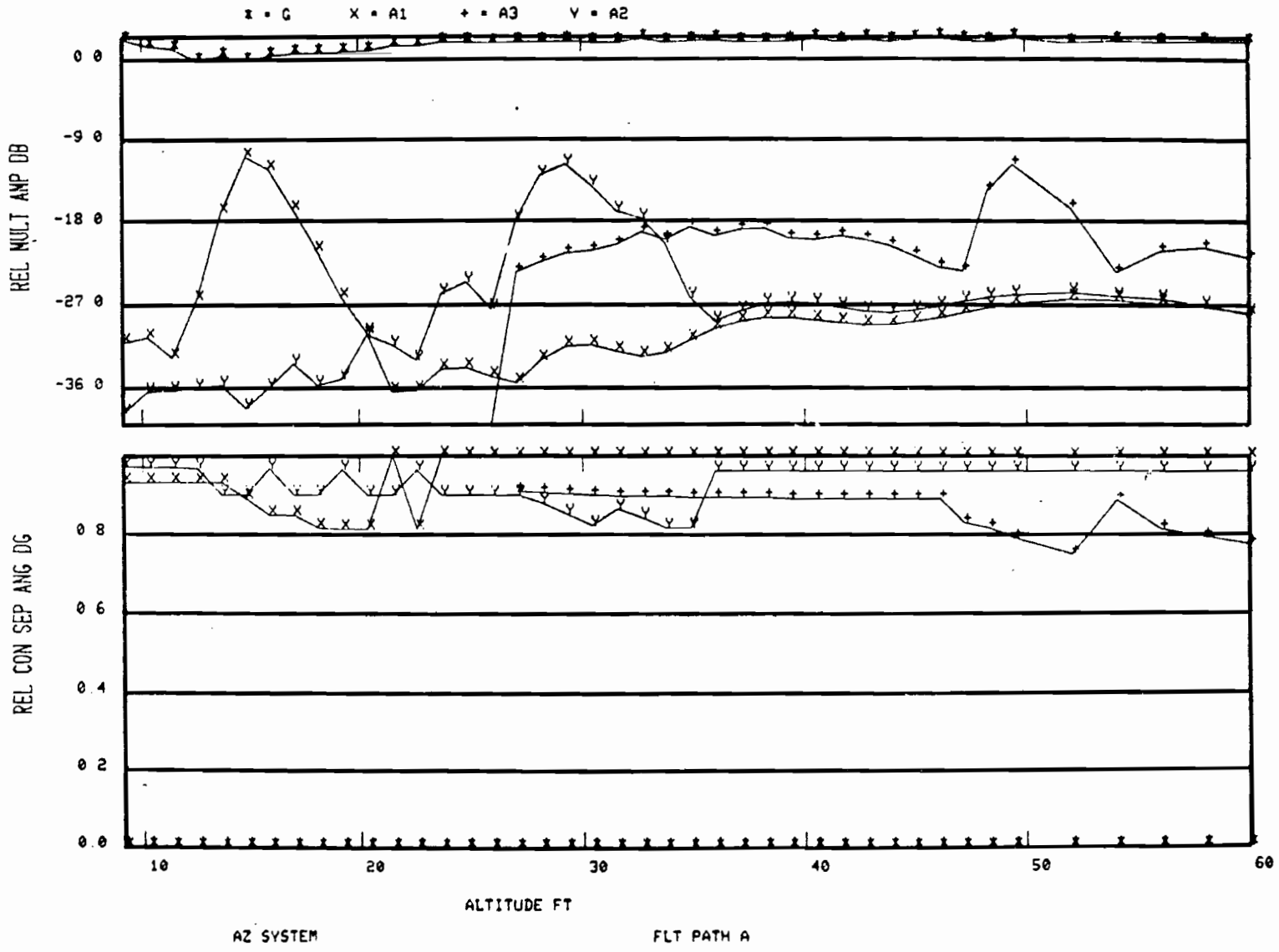

Fig. 8-26. Multipath amplitudes and separation angles for study #W2.

Figure 8-27 shows the azimuth errors at zero aircraft velocity and with a velocity of 200 ft/sec. Also shown is the path following filter (expressed as lineal displacement) and control motion filter output. The very large error that occurs at an altitude of 12 feet is due to a fuselage reflection from aircraft A1. The error is quite large because the various ground reflection paths have nulled the direct signal more than the fuselage reflection,* so that the effective M/D is increased by ≈ 6 dB over that shown in the multipath diagnostic. At this point, motion averaging was quite ineffective; however, in the remainder of the region, the motion averaging appears to have reduced the errors by the expected factor of $1/\sqrt{3}$.

On the basis of run #W2, it seems clear that a substantially larger beamwidth (e.g., 3°) could probably yield quite large errors even for aircraft with a 300-foot offset. Thus, it does not appear that the wide basic azimuth beamwidth could be increased by a large factor (e.g., 3).

(b) Basic Narrow Aperture System Run

Figure 8-28 is the computer generated map for a basic narrow aperture critical areas run with eight B727 aircraft scatterers, while Fig. 8-29 shows the relationship of the aircraft positions to the narrow basic error contours. Again we see that there is good correspondence between the peaks with the desired peak amplitude altitudes.

The multipath levels and separation angles of the six largest components are plotted in Figs. 8-30 and 8-31. The azimuthal levels are noticeably lower

---

*This phenomena is discussed in some depth in Ch. 9 of this report.

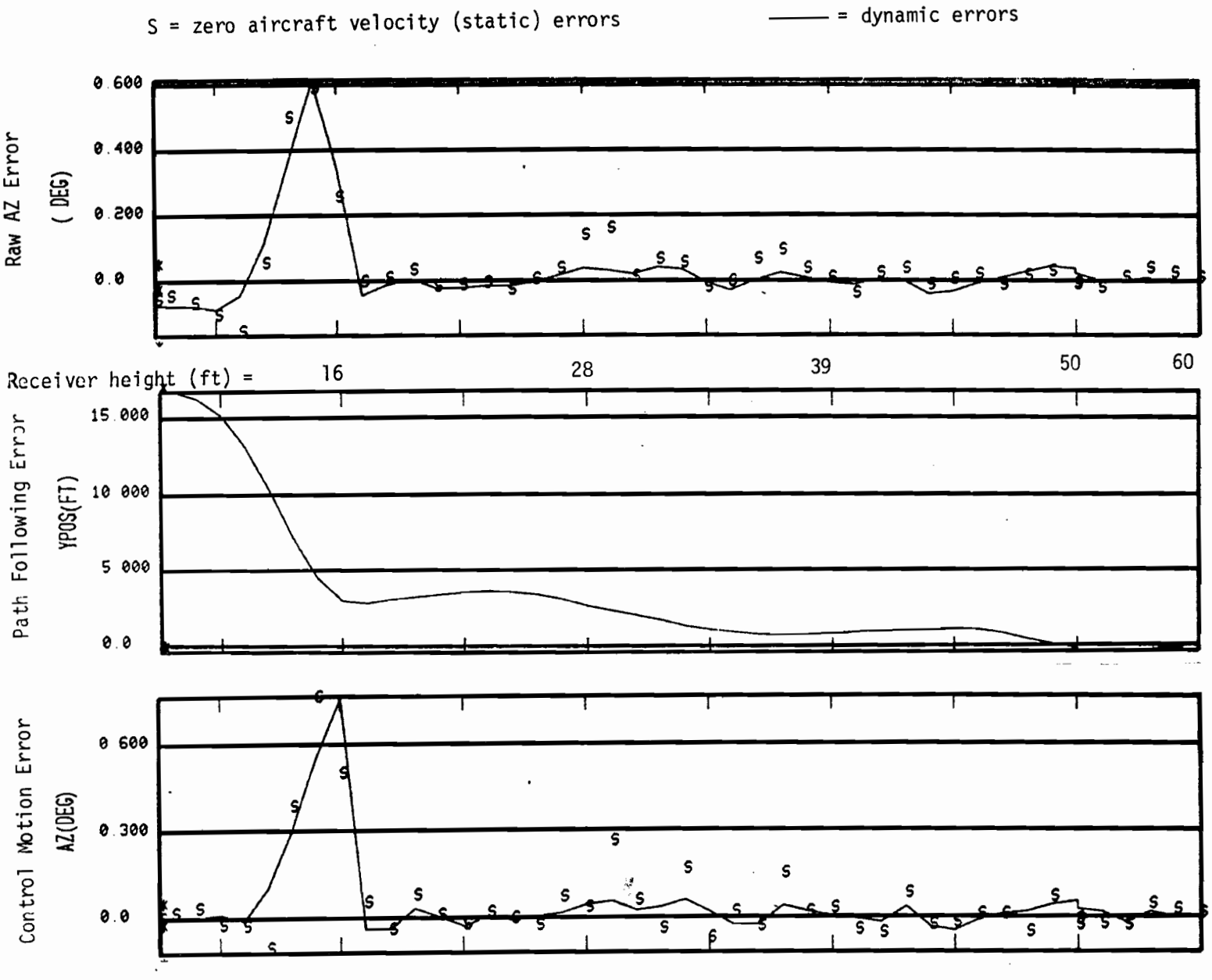

Fig. 8-27. Azimuthal angular and linear displacement errors for study #W2.

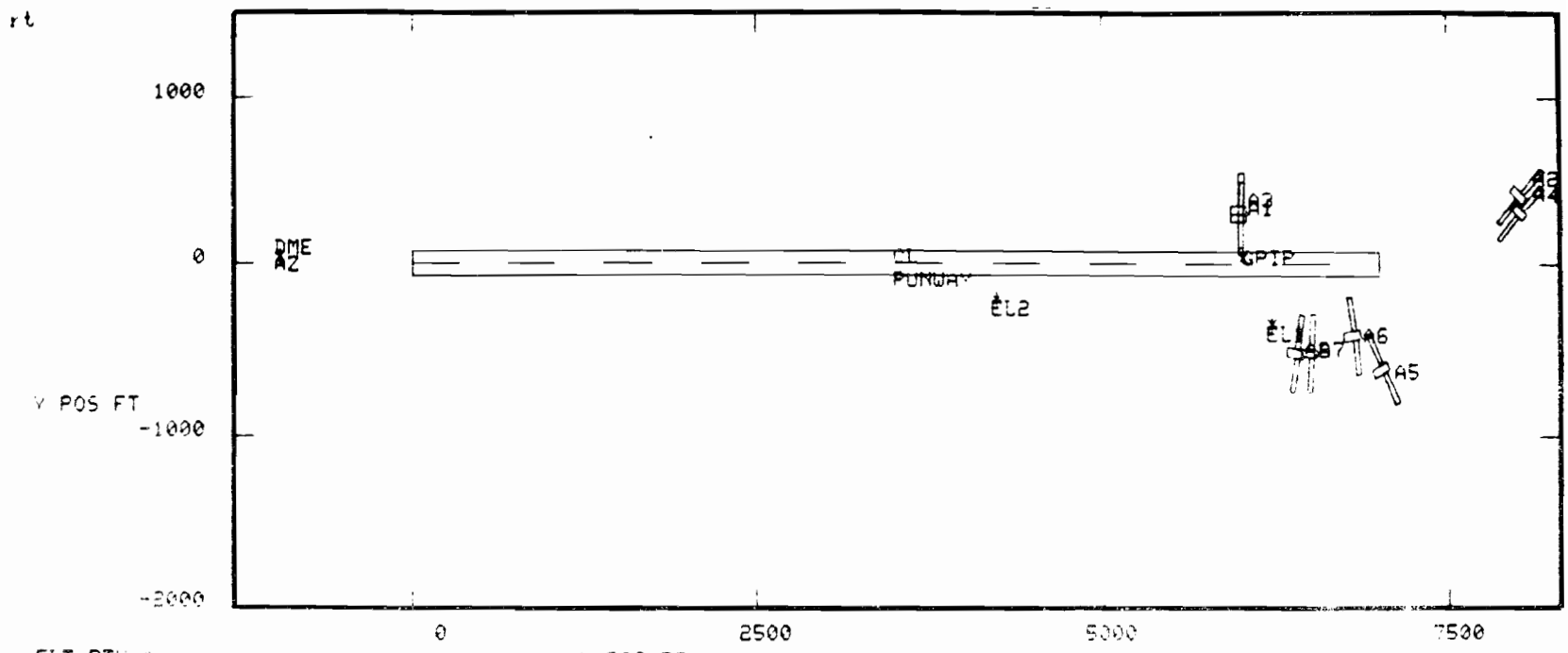

FLT PTH A

AZ SYSTEM

OBST	RANK	AMP	ALT	RDOP
G	1	-1	64 0	0
A1	7	31	167 9	-71
A2	4	20	102 0	-970
A3	6	31	195 9	-46
A4	3	19	99 9	-960
A5	5	21	66 0	-529
A6	2	19	91 9	-64
A7	8	49	141 9	-29
A8	9	69	251 8	-400

EL SYSTEM

OBST	RANK	AMP	ALT	PDOP
G	1	3	325 8	-0
A1	9	66	120 0	3017
A2	7	22	93 9	-1318
A3	2	66	173 9	2617
A4	5	20	37 6	-1246
A5	6	20	62 0	-592
A6	4	12	106 0	-22
A7	2	11	62 0	-86
A8	3	11	191 9	-4

AZ critical areas a/c

EL critical areas a/c

Fig. 8-28. Airport map for study #N1 for basic narrow aperture TRSB critical areas.

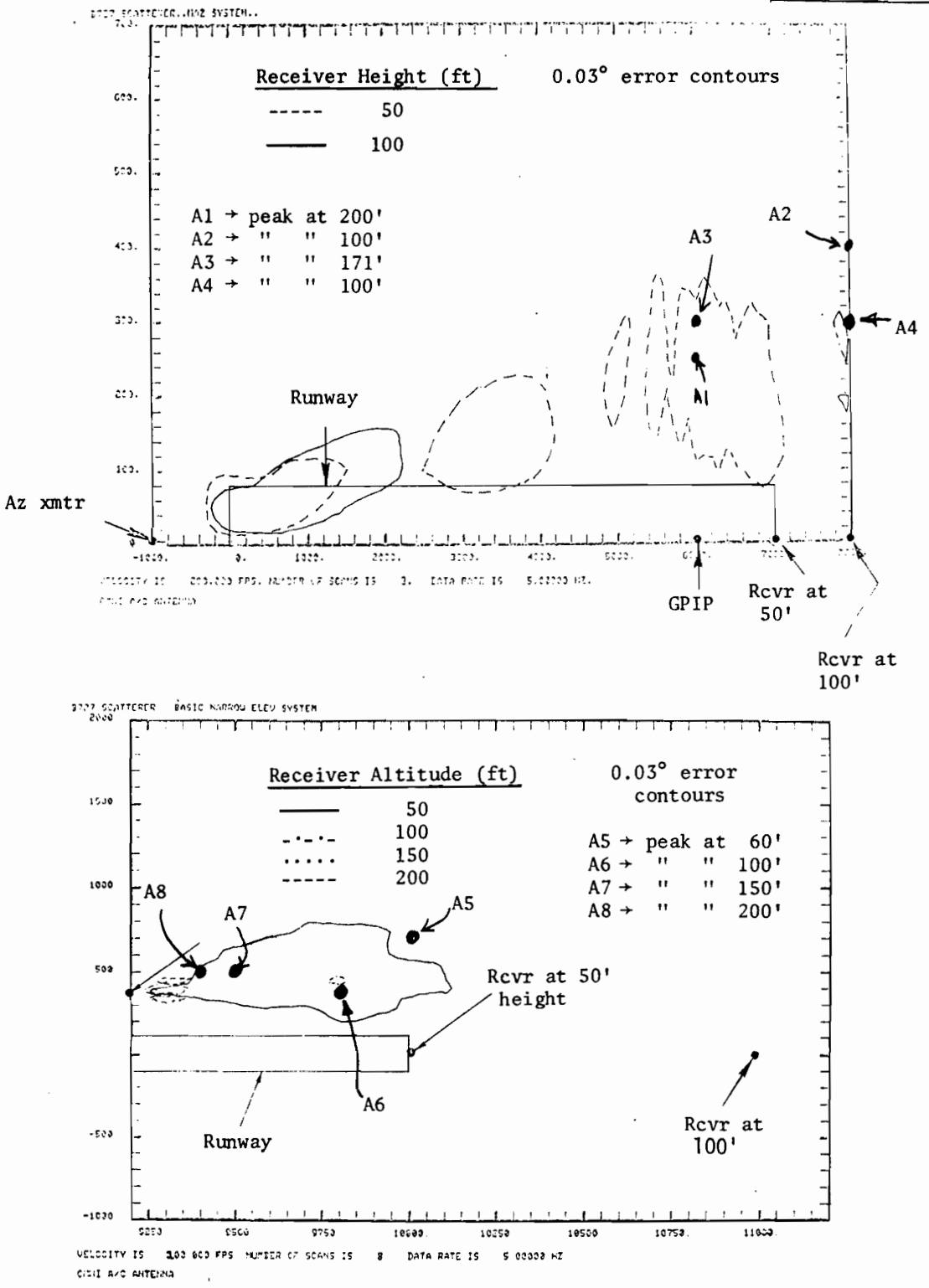

Fig. 8-29. Relation of B727 scatterer positions to narrow basic system error contours for run #N1.

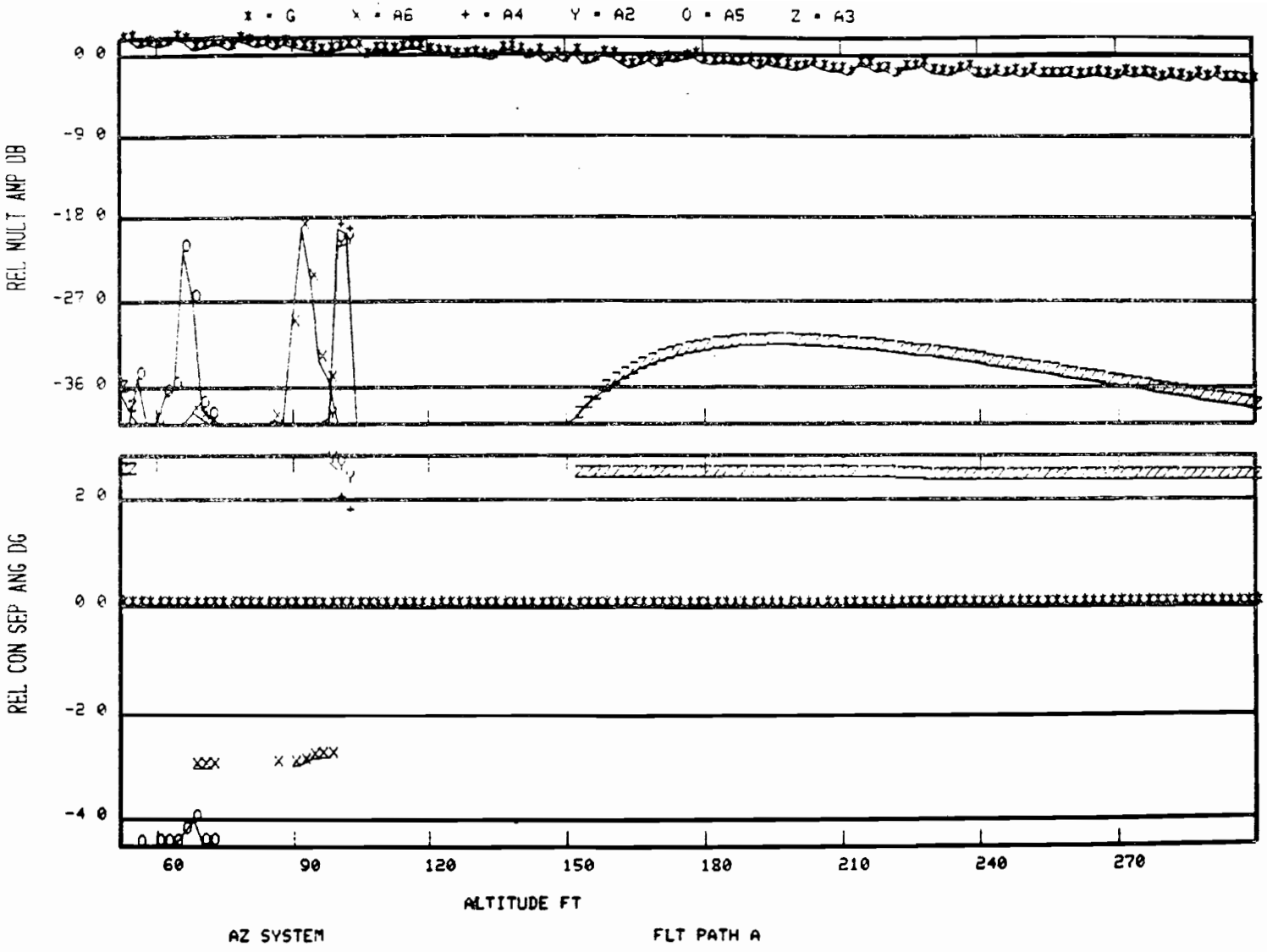

Fig. 8-30. Multipath diagnostics for narrow aperture azimuth study #N1.

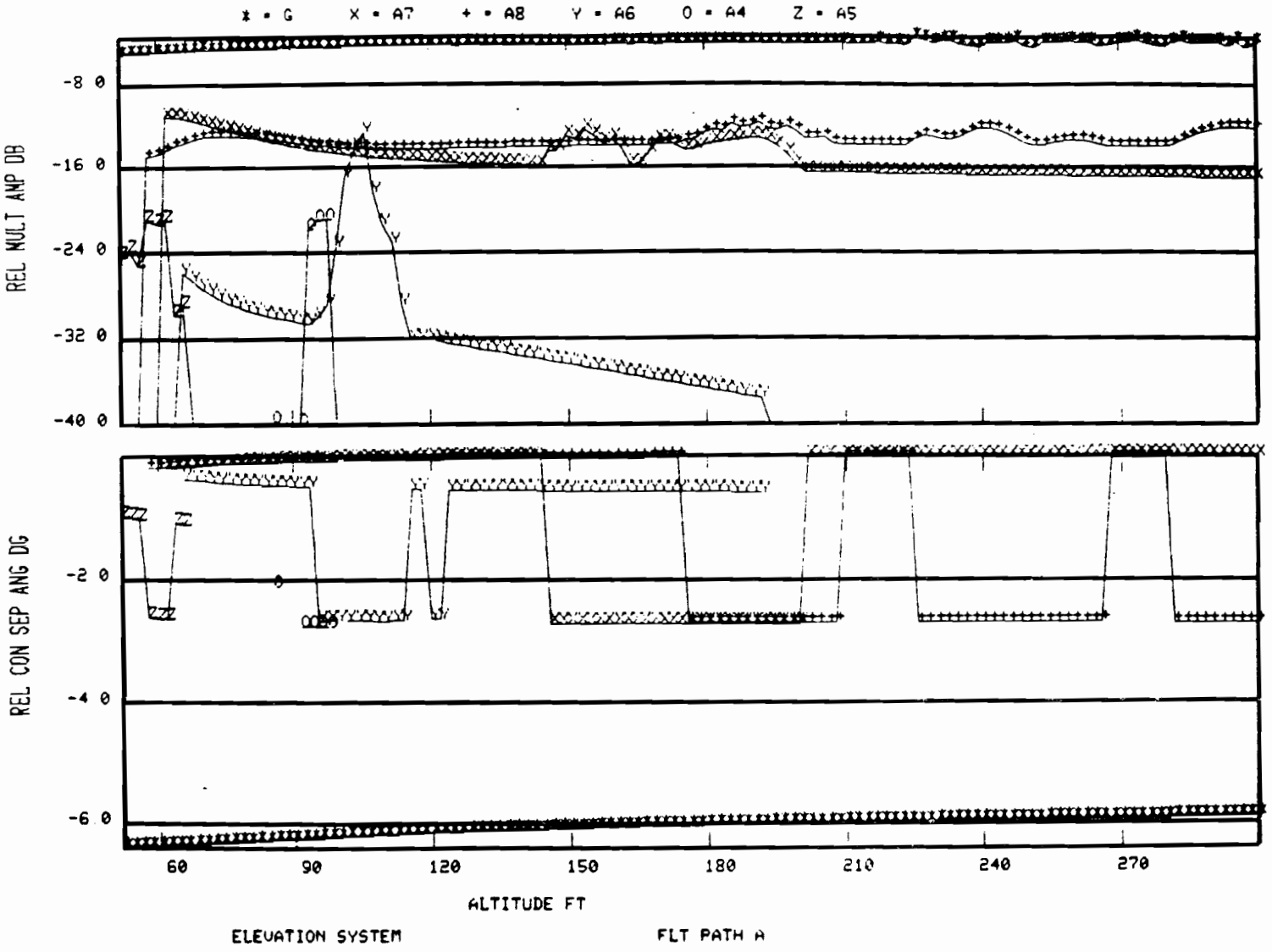

Fig. 8-31. Multipath diagnostics for narrow aperture EL-1 study #N1.

and of shorter duration than those from the B747 in the previous study, but the elevation levels are fairly similar. As was the case earlier, abrupt changes occur in the elevation separation angles as the plotted component from a given aircraft changes from the tail fin (at close to zero separation angle) to the fuselage (at close to 3° separation angle).

The angular errors are shown in Fig. 8-32. Again the azimuthal errors are small, primarily because the multipath durations were so short that "worst case" phase conditions did not occur and motion averaging was more effective than "on the average."

The elevation multipath was of considerably longer duration, so that the errors are more nearly comparable to the error contours. The errors above 200-foot altitude arise from reflections from aircraft A8, while the errors below 90 feet represent the error due to simultaneous specular reflections from aircraft A5, A7 and A8.

8.5 Tentative Conclusions Regarding Critical Areas for Reflection Effects

In this section, we give some tentative estimates for the TRSB critical areas needed to avoid significant reflection effects. The basic criteria used here has been the 0.03° error contours as tempered by the full run results of the preceding section. In particular, for those cases (azimuth in particular), in which the contours seem overly conservative, we have used engineering judgement and the full contour plots (such as Figs. 8-8 and 8-14) to arrive at proposed boundaries.

Our basis for this was as follows:

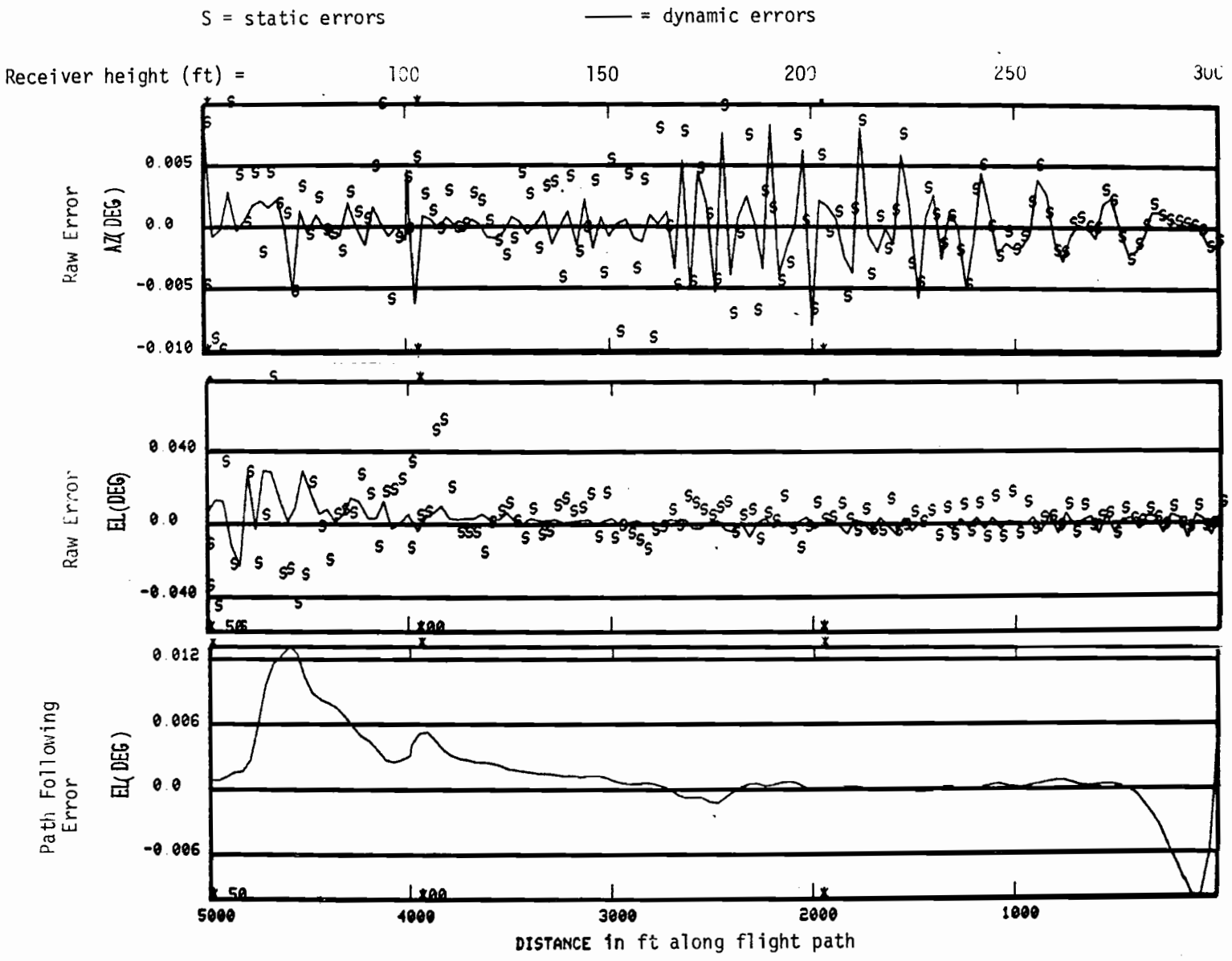

Fig. 8-32. Angular errors along flight path for basic narrow aperture study #N1.

(1) Although the error contour value of 0.03° is less than the MLS functional requirement specification of 0.05° for control noise, there are certain equipment errors of currently unspecified magnitude which must also be considered. (i.e., the "propagation contribution" will be less than 0.05°). Also, more than one scatterer will probably be present at most future airports where critical areas would be of concern to the airport operator.

(2) It can be dangerous to rely too heavily on the results of one or two runs at C-band due to the very rapid changes in error characteristic which can occur at C-band with small lateral and vertical displacements of the receiving aircraft.*

(3) The results of the preceding sections clearly suggest that MLS "folklore" such as "multipath < 10 dB down can be ignored," "aircraft reflections will occur over a flight path segment = twice aircraft length" and/or extrapolations based on ILS behavior cannot be reliably used to define the critical areas.

We recognize that the criteria used here are not as well defined as those used in the ILS studies [38], but they are believed to be appropriate for the amount of quantitative data available at this time.

---

*During the next phase, we plan to explore the spatial inhomogeneity problem in considerable depth using an improved perturbation smoothing envelope. Also, a number of other scattering aircraft locations will be investigated.

(a) Basic Wide Aperture Azimuth Critical Areas for Reflectors

In Fig. 8-33, we show the preliminary specification for the wide aperture azimuth critical areas. We will address each of the various regions in turn, including a discussion of how the deficiencies in the current estimates will be rectified in the coming months.

The cat I/II specification is based on the contour maps together with the observation that the errors which occur at 50-foot altitude typically do not extend far up the flight path. This is because for aircraft altitudes at or above the scattering aircraft tail fin, the multipath levels and errors drop off sharply for scattering aircraft located near the threshold. This leaves a residual area extending several thousand feet in front of the azimuth transmitter. The extent away from centerline was kept at 100 foot to avoid near field effects where the beam pattern is not yet well formed.

The additional area denoted by arrows for cat III operation is based on the contour maps and the results of the two full runs. At a 300-foot offset, the full run errors were inconsequential with or without receiver motion; however, the errors at 150-foot offset were quite large. Thus, the area shown is inside the error contours, but outside the positions in run #W2.

The relatively poor correspondence in some cases between the "worst case" azimuth error contours and the full run azimuth errors will be investigated in detail in subsequent runs using (improved) perturbation sampling. Another area to be investigated concerns multipath received from behind the aircraft which is scattered by trucks near or forward of the threshold; it was assumed in Fig. 8-33 that a cat III aircraft would restrict coverage to at most $\pm$ 120°

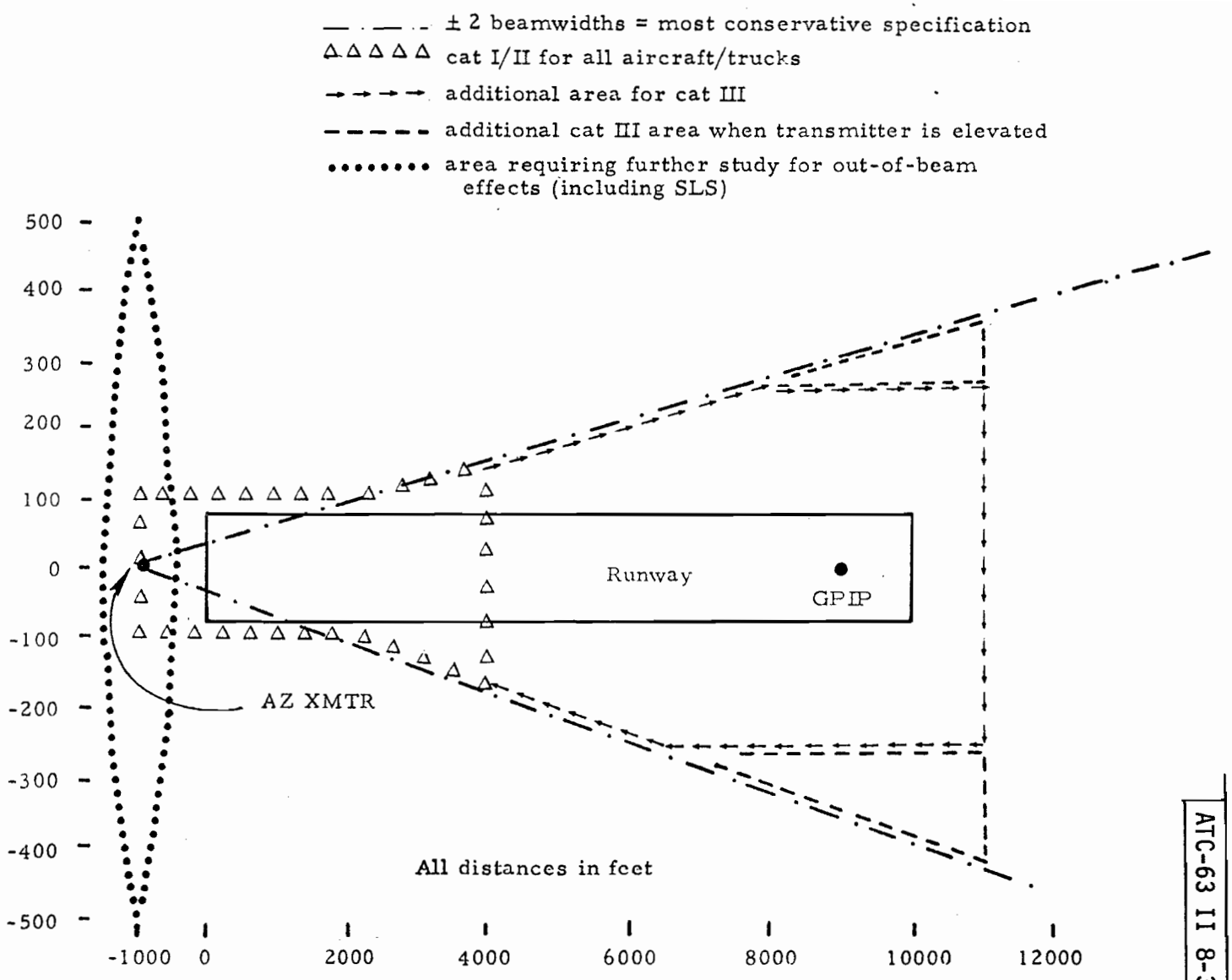

Fig. 8-33. Preliminary WAZ critical areas specification.

on either side of the nose. In that respect, if a more highly directional aircraft antenna can be assumed, the region forward of the runway threshold can be eliminated.

For an elevated transmitter, the "worst case" errors at the 2° boundary were close to 0.12°. Thus, it seems likely that the critical area boundary would have to be extended outward as indicated by the dashed line. Full runs will be made for this case during the next phase.

The analysis in the preceding sections has focused exclusively on the "inbeam" aspect for critical areas. However, one must also consider the possibility of very large out-of-beam levels persisting for long periods. In terms of critical areas, this might occur with trucks near the azimuth transmitter (e.g., with positions analogous to the MLS screen tests). The dotted line indicates a region where trucks might have to be excluded to avoid generating M/D ratios greater than unity due to Fresnel integral overshoot effects that occur when the subtended truck dimensions are approximately two Fresnel zone radii. Also, one might have excessive SLS signal levels being reflected into the desired coverage zone such that guidance would be denied to aircraft on final approach. These points will be investigated in the next phase by plotting out contours of effective multipath level ($\tilde{\rho}$) for truck and aircraft positions near the transmitter.

For ILS, the term "critical area" has always been associated with an aircraft on final approach in part because ILS only furnishes proportional guidance over a fairly narrow angular sector centered on the centerline. Since MLS is intended to furnish wide angle proportional guidance, there

arises the possibility that additional areas may need to be kept clear in order to insure adequate guidance.

For the azimuth system, there does not seem to be any additional requirement for receivers on curved approaches insofar as reflection effects go (however, shadowing probably will necessitate a region). This statement is based on running contour maps analogous to those of section 8.2 for an aircraft at ranges of 5-10 nmi and elevation angles of 1°-3°. In no case were there error contours $\geq$ 0.03°, whereas errors as large as 0.10° could probably be tolerated.

(b) Basic Wide Elevation #1 Critical Areas for Reflectors

Figure 8-34 shows the preliminary estimates of the critical areas required for the EL-1 system to avoid reflection errors. These regions are based primarily on the error contours inasmuch as they seem to agree well with the full runs. The region shown for cat III assumes:

(1) B747 scattering aircraft

(2) omni aircraft antenna

(3) need for high quality guidance down to 50 feet

If either smaller scattering aircraft (e.g., B727) or a directional airborne antenna (beamwidth $\leq$ 30°) may be assumed, the region then decreases to that indicated by triangles.

The cat I/II region also assumed B747 scatterers and an omni airborne antenna. However, it is assumed that high quality guidance need only be provided down to 75-foot altitude. If only B727 type aircraft are present, there are no 0.03° error contours for receiver altitudes $\geq$ 100 feet. Use of a directional airborne antenna would not significantly change these regions.

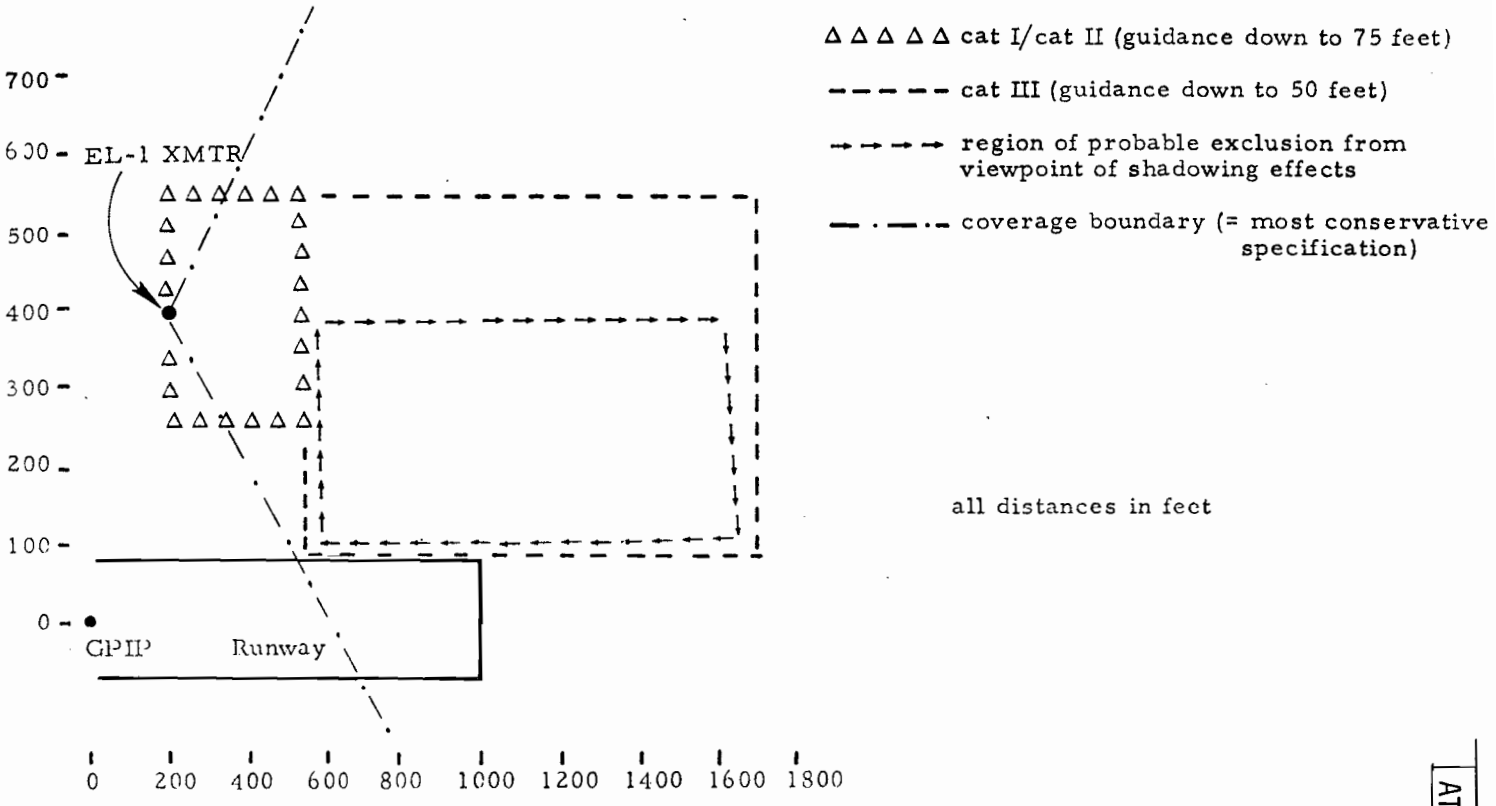

Fig. 8-34. Preliminary critical areas for wide aperture EL-1 system.

Also shown in Fig. 8-34 is a region that almost certainly will be kept clear of aircraft to avoid shadowing and/or obstruction clearance violations. Thus we see that much of the area required to avoid reflection effects would also be kept clear for other reasons as well.

No allowance has been made in Fig. 8-34 for the clearances needed to avoid reflection errors when not on final approach. From the contour maps in Fig. 8-9, we conclude that for receiver elevation angles $\geq 2.86°$, specular reflections on curved approaches would not necessitate any increase in the critical areas beyond that shown in Fig. 8-34. If aircraft elevation angles as low as 1° were of concern, one would have to extend the regions forward (i.e., along runway CL) 1000-2000 feet. However, in such a case one could anticipate an even larger region which must be kept clear to avoid shadowing errors as well.

(c) Basic Narrow Aperture Azimuth Critical Areas for Reflectors

Figure 8-35 shows the preliminary estimates of the critical areas for the narrow aperture azimuth array. Since the operational utilization of this system is not yet well defined, we have attempted to show how the critical area varies with the major operational choices.

The cat I/II outline with Δ's assumes B727 type scatterers and a requirement for guidance down to the cat II MGA of 50 feet. The region shown is based on the contour maps with a substantial reduction near the threshold based on the narrow basic full run. This reduction is operationally significant since the most conservative specification would include many taxiways near the threshold. Thus additional full runs will be made in the next phase to further confirm this narrow strip near threshold.

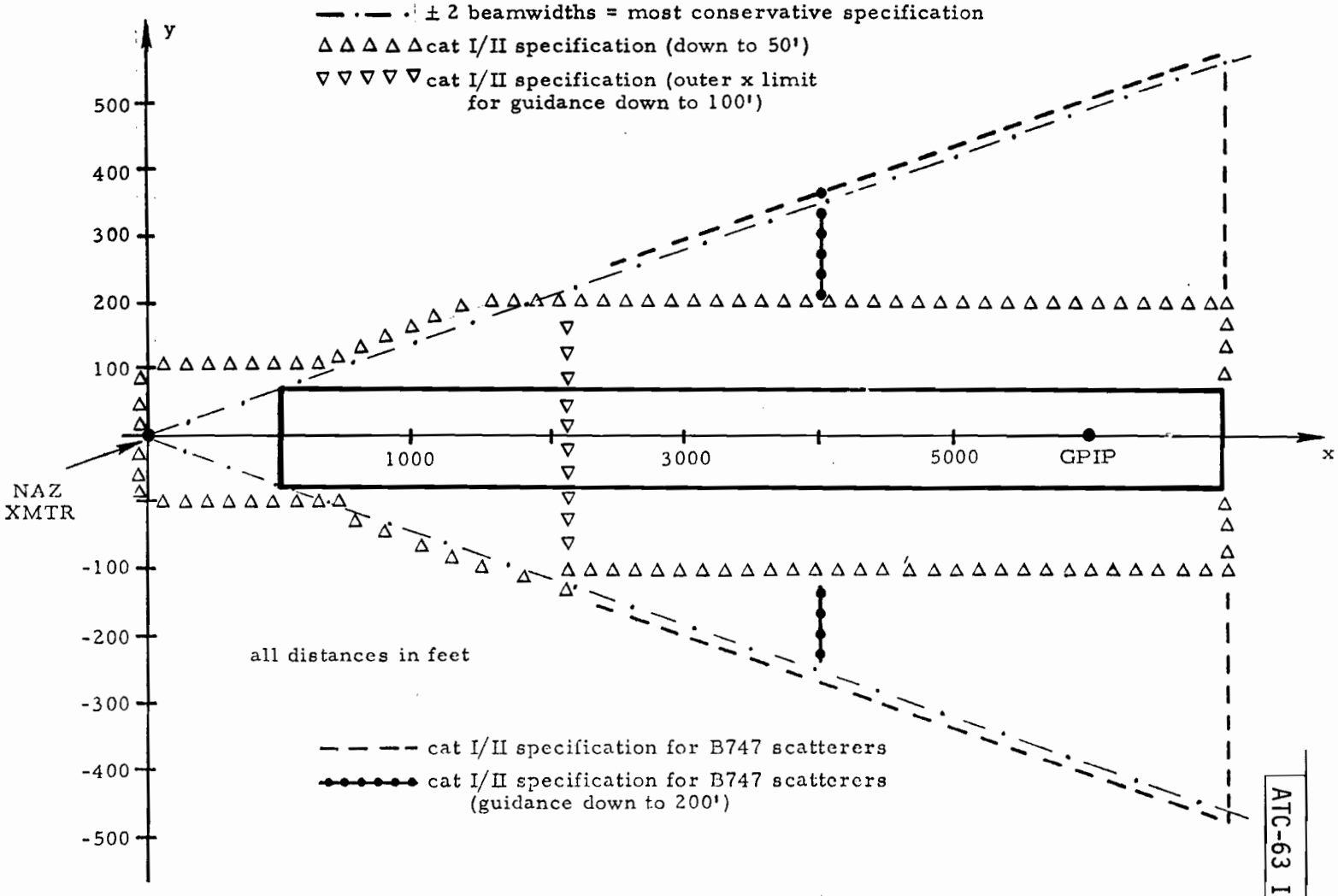

Fig. 8-35. Preliminary specification of narrow basic azimuth critical areas.

ATC-63 II 8-35

If guidance need only be provided down to 100 feet, then the x extent of the cat I/II region may be terminated by the inverted triangles. This is based on the contour maps and the full run simulation.

For the short runways contemplated as narrow azimuth sites, it seems unlikely that B747 aircraft would be present. However, if the trend to short fuselage, wide-bodied aircraft continues, one might have B747 type aircraft present in the future. The cat I/II region indicated for B747 is based on the contour maps of section 8.2. If guidance down to 200 feet is all that is required, the region near the threshold can be eliminated as indicated by the solid squares. It is expected that these B747 regions can be reduced somewhat when full run results are available.

(d) Basic Narrow Aperture Elevation Critical Areas for Reflectors

Figure 8-36 shows the preliminary specification for the narrow aperture elevation system critical areas. This specification was based primarily on the contour maps inasmuch as they agreed fairly well with the full system runs.

The area indicated with open squares assumes that high quality guidance is desired down to 50-foot altitude and that B727 type scatterers are present. However, in many cases, high quality guidance may only be required down to 100-foot altitude. For such cases, the critical areas extent can be sharply reduced as indicated by the Δ's.

With B747 type scattering aircraft, the critical area must be extended outward as indicated by the solid squares, even when the MGA is 100 feet.

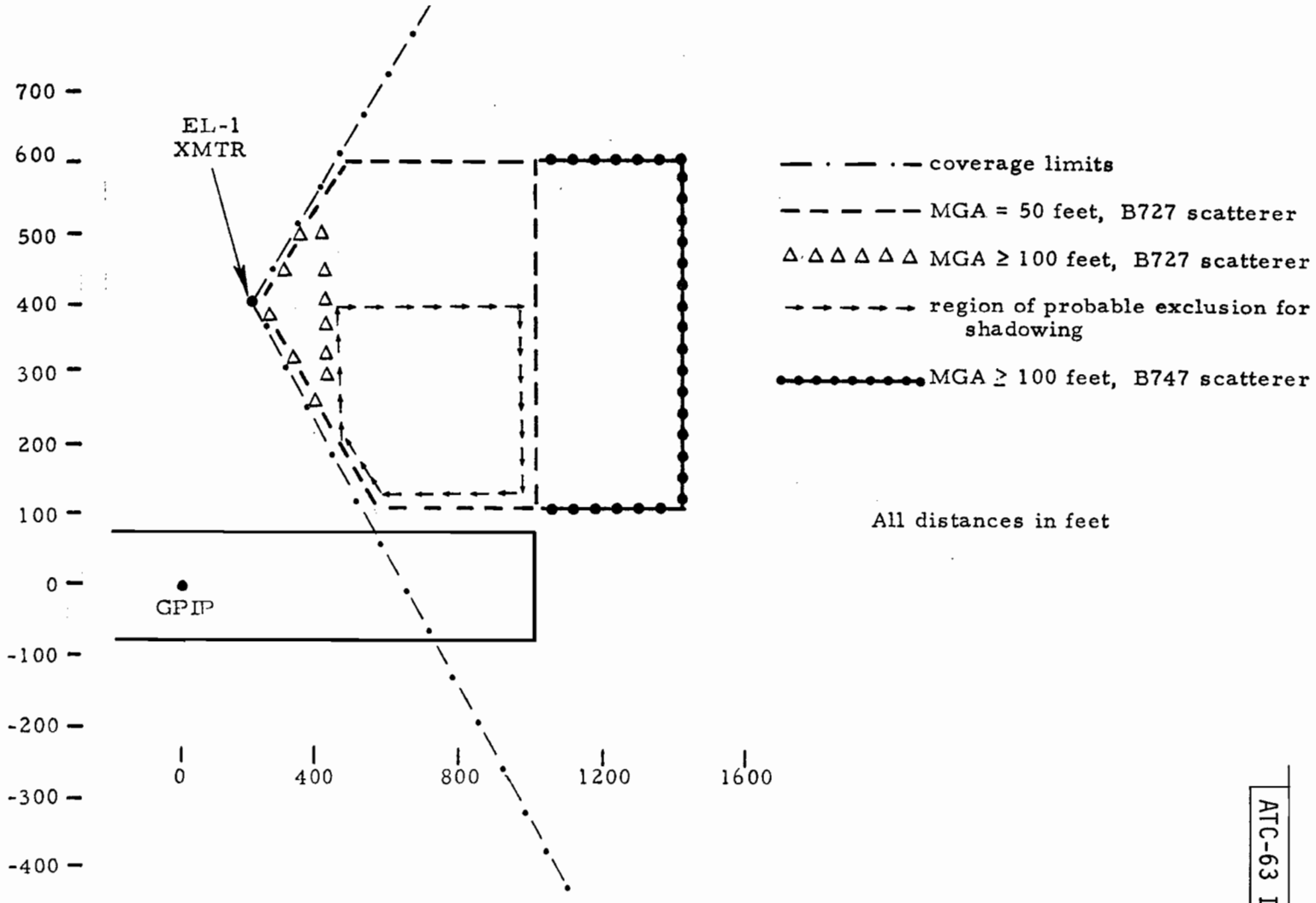

Fig. 8-36. Preliminary specification of narrow basic EL-1 critical areas.

IX. POLARIZATION STUDIES

Considerable discussion has arisen in the U.S. over the choice of polarization for MLS (see e.g., references[37,68-79]). The principal claim made by the proponents of a change in polarization is that MLS multipath performance may be unacceptable with vertical polarization (VP), but would be acceptable if horizontal polarization (HP) or circular polarization (CP) were adopted as the MLS standard. The Lincoln studies during the first phase of the Lincoln MLS program have focussed on two issues:

1. which aspects of TRSB multipath performance are most likely to be marginal with VP,
2. what level of multipath performance can be expected with HP or CP in existing airport environments.

To address the first issue, a series of systems analysis studies were made, the results of which are summarized in Section 9.1.

The results of Section 9.1 highlights the importance of several factors not addressed in depth in many studies to date. One of these, the distribution of building surfaces facing the runways at representative airports, has been studied in a survey of eight major U.S. civilian airports. The results of this airport survey are briefly summarized in Section 9.2. In Section 9.3, we summarize some of the conclusions reached to date in this area and identify the key areas still to be resolved.

9.1 Assessment of Expected TRSB Multipath Performance

In this section, we summarize the results of some systems studies to identify those aspects of TRSB multipath performance which are of greatest concern. The key tool in this analysis was a "multipath power budget" akin to the usual signal-to-noise ratio power budget. The idea is that one computes the multipath to direct (M/D) ratio as the sum of a number of different factors and then compares it to the M/D ratio required for the TRSB system to operate satisfactorily in the given environment.

The prime concern is with specular reflections from aircraft and buildings. It follows from Chapters II and III that the effective M/D level can be written as the product of seven factors:

$$\rho = R_{eq} \times C_{distance} \times C_{roughness} \times C_{size} \times C_{secondary} \times C_{gnd\ ant} \times C_{a/c\ ant} \qquad (9\text{-}1)$$

where:

R_{eq} = Fresnel reflection coefficient which is a function of surface dielectric properties, angle of incidence and polarization (=1 for metallic surfaces with either linear polarization, otherwise < 1)

$C_{distance}$ = ratio of direct path distance/multipath distance (<1 always)

$C_{roughness}$ = coefficient taking into account surface roughness (=1 for perfectly flat surfaces, 1 otherwise). For corrugated surfaces, this factor is typically less than one in any single reflection direction; however, reflections come off at a number of discrete angles. The magnitude between the various components depends on polarization, corrugation type and dimensions.

C_{size} = coefficient related to the building size. In Fig. 9-1, we show this size factor as a function of normalized building size for the special case where the building height = subtended width and the specular point is located at the building center. The values for other combinations of height and width can be obtained as the geometric mean of the values in Fig. 9-1 for the height and subtended width, respectively. For aircraft, the loss (typically at least 8 dB) due to ray divergence is regarded as a part of this coefficient.

$C_{secondary}$ = factor accounting for the influence of the various secondary paths involving building/aircraft reflections and ground reflections, as was illustrated in Fig. 3-6.

$C_{gnd\ ant}$ = ratio of ground antenna gain toward multipath specular point versus that toward the direct path where this difference arises in the plane of the scan (e.g., by power programming), the difference is termed "coverage control". When the gain difference arises in the plane orthogonal to the scan plane, we have "pattern control" Pattern control is of greatest direct aid for elevation arrays since the specular point and receiver are typically at very similar elevation angles in most azimuthal multipath situations. However, the elevation pattern of the azimuth array does enter into the $C_{secondary}$ factor, as will be discussed subsequently.

$C_{a/c\ ant}$ = ratio of airborne antenna gain toward multipath source relative to the gain toward the ground transmitter.

Since Eq. (9-1) involves the product of seven dimensionless factors, we can add up the various contributions in dB relative to unity to determine the value of ρ.

Next we turn to the required M/D ratio. In the case of out-of-beam multipath, the answer may be determined in a straightforward manner from the characteristics of the receiver acquisition/validation circuitry. For current TRSB processor, this circuitry has the following characteristics:

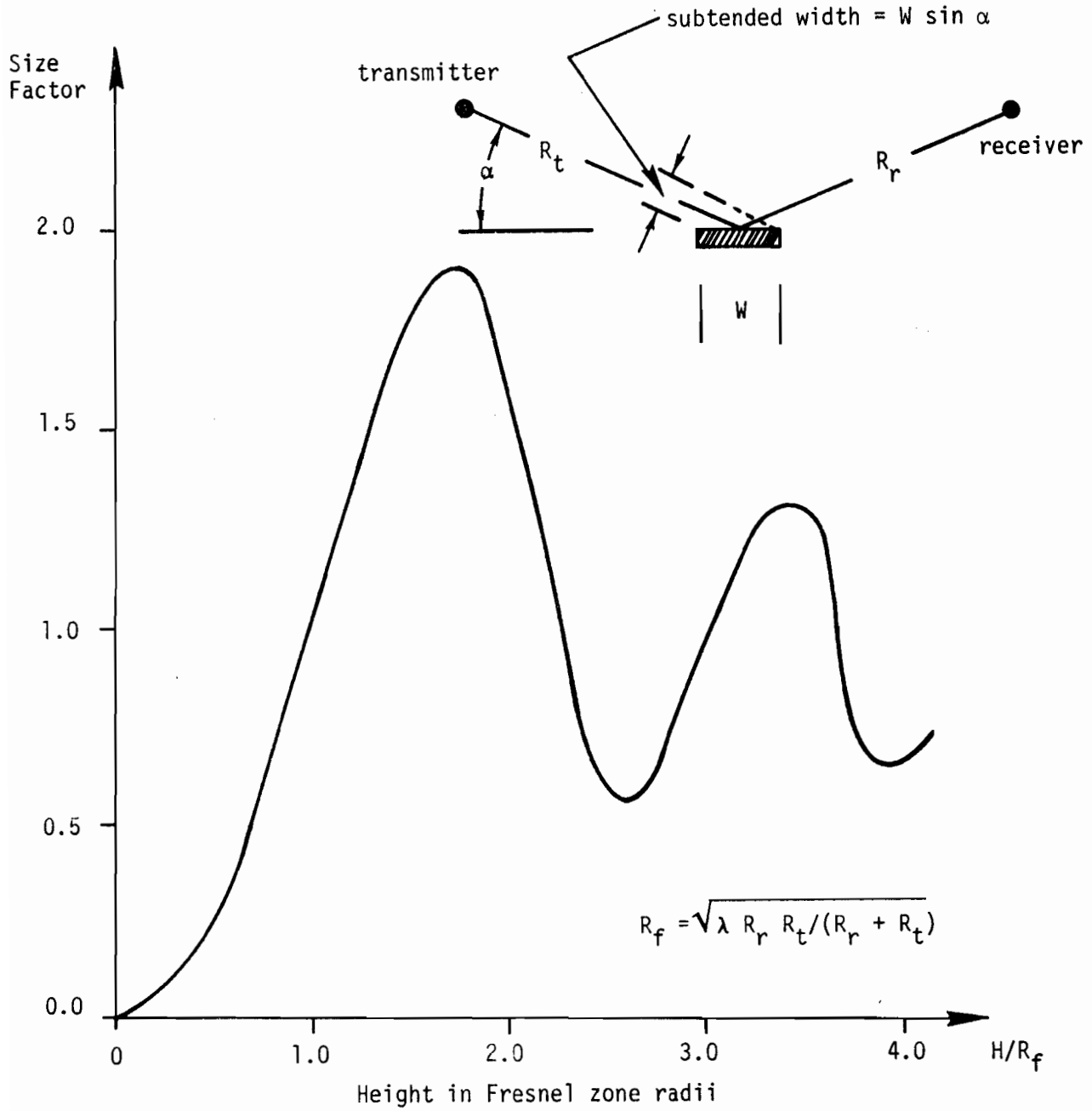

Building height = H = subtended width

Specular point located at building center

Fig. 9-1. Size factor for building.

Peak Out of Beam M/D Level	Effect on: Acquisition	Tracking
ρ_m < 0.707 (-3 dB)	none	none
0.707 $\leq \rho_m \leq$ 0.9 (-1 dB)	delays acquisition	no effect
0.9 $\leq \rho_m \leq$ 1.1 (+1 dB)	no acquisition	causes track loss after 7 seconds
1.1 < ρ_m	false acquisition	loss of track after 7 seconds

From the above, we see that only out-of-beam levels above +1 dB are of the highest concern with levels above -1 dB causing operational inconvenience in terms of missed approaches. Also, it should be noted that these values reflect the specific receiver implementation used in the field tests. Next, generation receivers are expected to tolerate much higher multipath levels (e.g., +5 dB) when in track.

For inbeam errors, it is convenient to make some approximations to yield a formulation analogous to that for the M/D ratio. It follows from the results of Chapter VI that

$$\varepsilon_{rms} \approx \underbrace{\rho}_{\substack{\text{M/D} \\ \text{level}}} \underbrace{0.7\theta\, e^{-1.07\,\theta^2/\theta_B^2}}_{\substack{\text{antenna} \\ \text{factor}}} \underbrace{f(\theta,\rho)}_{\substack{\text{receiver} \\ \text{factor}}} \underbrace{A(\omega_s)}_{\substack{\text{motion averaging} \\ \text{improvement factor}}} \qquad (9\text{-}2)$$

Equation (9-2) is essentially Eq. (6-3) specialized to the case of -3 dB threshold with an additional term to take into account certain TRSB receiver validation features which reduce the error slightly to a level below that expected by "adding up the envelopes" as in Fig. 4-1. From Chapter VI, it appears that this factor is typically 0.8 to 0.9. The leading term of 0.7 represents the rms value of a sinusoid.

The error given by Eq. (9-2) must be related to the error criteria for the MLS. This necessarily involves assumptions regarding the spectral content of the error signal. Here, we make assumption akin to that of Chapter 5: the errors given by (9-2) are taken to be independent white random variables corresponding to the average of M contiguous to-fro scans. If these variables are generated at a 5 Hz data rate, their spectrum is then flat over the range 0 to 2.5 Hz. The TRSB error specifications are defined in terms of the rms output of certain analog filters. Thus, we have the relationship

$$\frac{\varepsilon_{rms}}{2.5}\left[\int_0^{2.5} H^2(f)\, dt\right]^{1/2} \leq C/2 \qquad (9\text{-}3)$$

as the relationship between allowable rms error and the 2σ error specification C. For the assumed error model the limiting specification is the control noise specification since it has the smallest value of C and the largest value of the integral. Taking $H(f) \sim 1.6/\sqrt{f^2 + 2.533}$ as an upper bound to the specified control motion filter, we obtain

$$0.78\, \varepsilon_{rms} \leq C/2 \qquad (9\text{-}4)$$

Given a control motion error specification for a given operational category, one can then use (9-4) to determine ε_{rms}. Then, Eq. (9-2) may be inverted to yield an upper value for ρ.

In Table 9-1, we show the results of one set of such calculation for the two cases of greatest concern in the polarization area. No allowance was made for airborne antenna gain due to the paucity of information regarding C-band

Table 9.1 Example of "Multipath Power Budget" for TRSB

	Azimuthal Out of Beam			Elevation in Beam
Fresnel reflection coefficient	-1 to -3 dB	dielectric (wood, glass, etc.), angle of incidence ≈10°	-4 dB	dielectric, angle of incidence is ≥ 20°
Roughness factor	0 dB	smooth surface	0 dB	
Size factor	0 dB	large vertical surface	0 dB	
Path distance factor	0 to -1 dB	aircraft at 5-10 miles	-1.6 dB	aircraft near threshold on 3° glideslope with multipath at -2.5°
Ground lobing	± 3 dB	a/c at 1° elev., 7 dB/deg elev. pattern slope at horizon (SBWG "D" configuration ant.)	0 dB	ground reflections are out of beam
Transmitter — pattern control	0 dB	(incorporated in ground lobing)	-4 dB	SBWG pattern differential gain at angles ≥ 20°
Transmitter — coverage control	0 dB	no power programming with azimuth angle	0 dB	
Airborne antenna gain	?		?	
M/D at receiver	+2 to -8 dB		-9.6 dB	
Error spec (2σ in dB re 1°)		-26 dB		0.05° control motion
ε_{rms}/error spec.		-3.9 dB		
Antenna factor		+11.5 dB		1° beamwidth, 0.5° separation angle
Receiver factor		+2 dB		
Motion averaging factor		+8 dB		$\sqrt{M}$ where M=8 samples
Desired M/D at receiver	-1 to -4 dB	Bendix receiver characteristics	-8.4	Desired M/D at receiver
Margin	+7 to -6 dB	Margin	+1.4 dB	

antenna patterns on actual aircraft. In Figs. 9-2 and 9-3, we show the L-band beacon antenna patterns measured on B727 and Cessna 150 models[71]. In both cases, we see that there could be several dB of multipath enhancement for

(a) direct signal at nose and multipath at an angle > 10° from the nose (e.g., as might occur on final approach)

and/or

(b) direct signal not at nose and multipath within 5° of direct signal azimuth (as might occur during a curved approach)

Figures 9-2 and 9-3 have been included here simply to show there could be a problem [the L-band antenna locations (fuselage underside) are an unlikely choice for MLS C-band antennas]. A number of studies are in progress to determine good C-band antenna locations. Figures 9-4 and 9-5 illustrate patterns for C-band antenna locations under active study. These patterns seem quite flat in the region of greatest interest. On the other hand, there is great interest in obtaining near omnidirectional MLS airborne coverage from a single antenna, which may compromise the pattern flatness as a function of azimuth.

If we assume these gains are 0 dB, then from Table 10-1 we see that the performance margin could be very small (or negative) for the conjectured environment. We would stress, however, that even if the margin is negative for some aircraft, the aircraft should not get into an unsafe position.

1. the out-of-beam multipath would either prevent acquisition or (at worst) generate an unflyable false course.

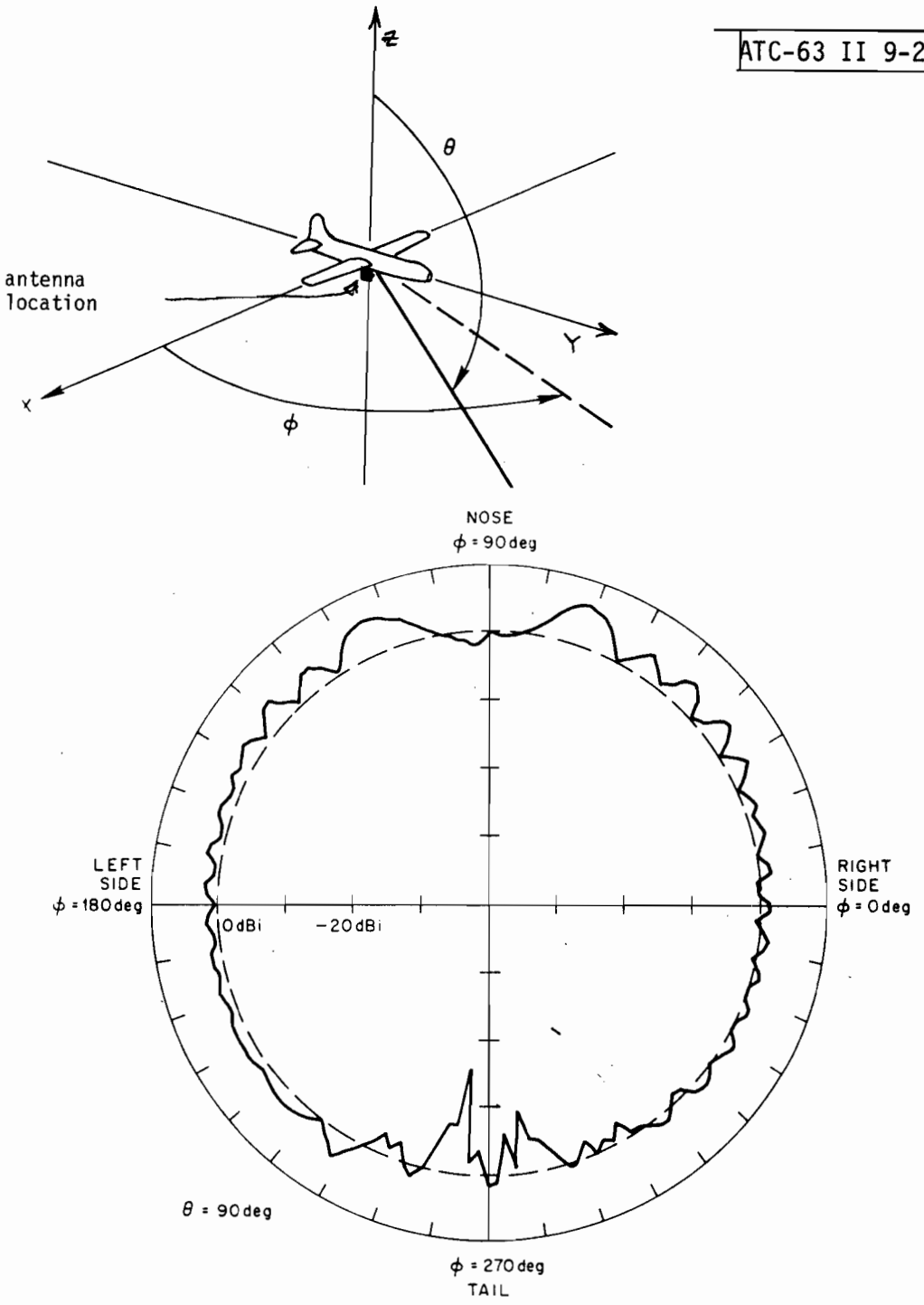

Fig. 9-2. Cessna 150 L-band antenna pattern in XY-plane (flaps up).

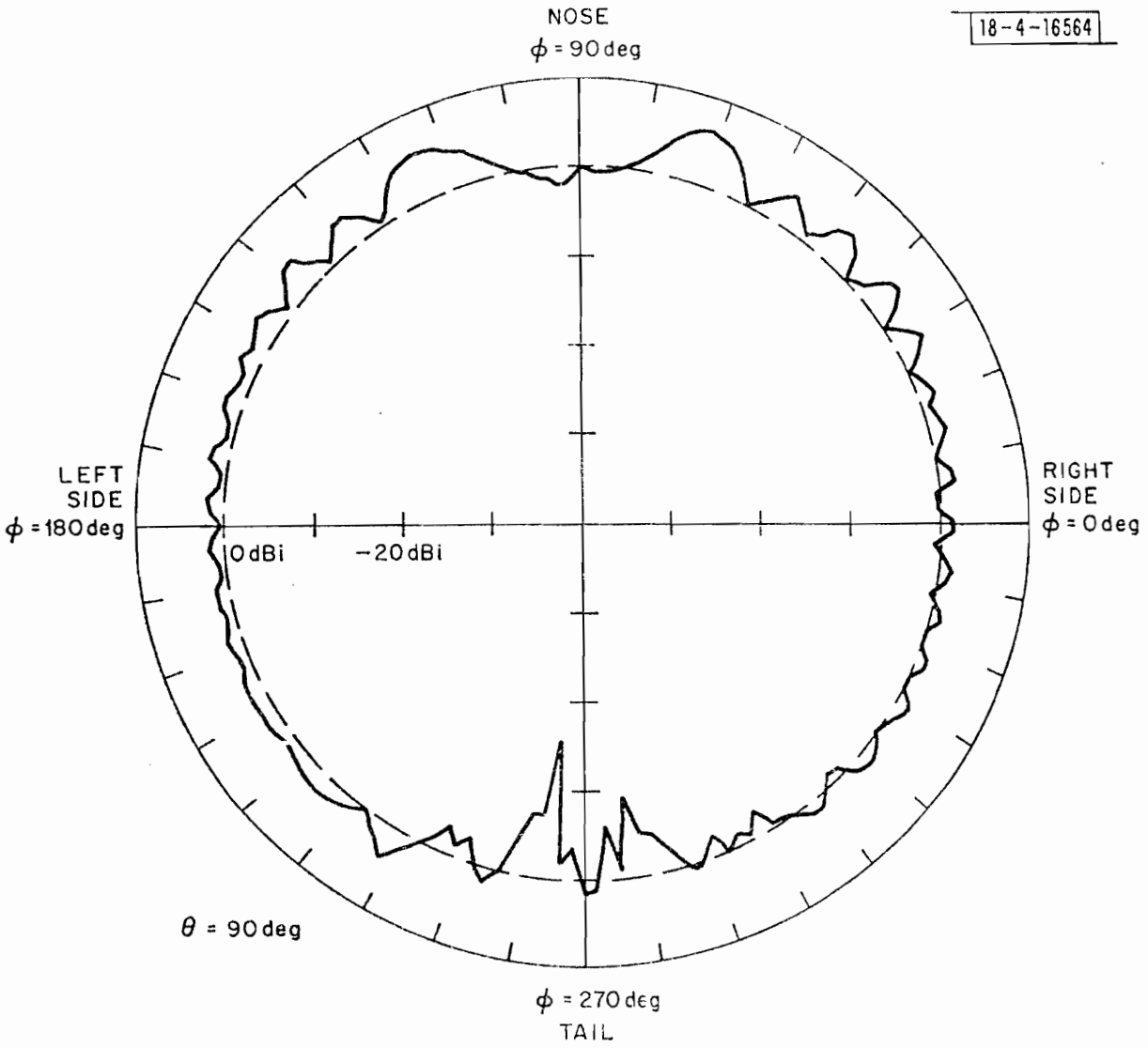

Fig. 9-3. Boeing 727 antenna pattern in XY-plane (antenna on fuselage underside midpoint; gear down).

ATC-63 II 9-4

ANTENNA - MONOPOLE
POLARIZATION - VERTICAL
PATTERN - HEADING
LOCATION - STIATION 305 TOP FUSELAGE

BOEING 737

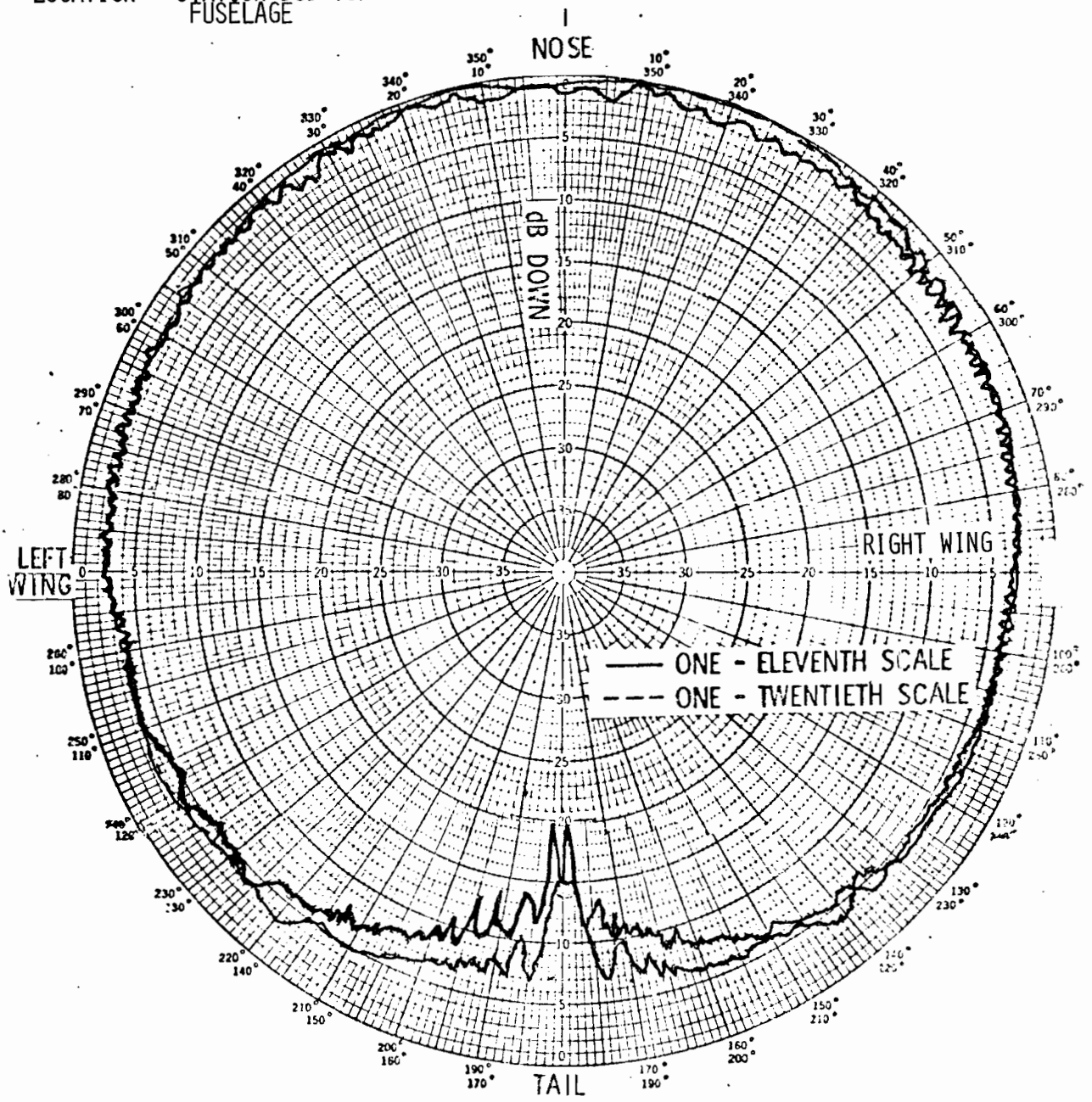

Fig. 9-4. Scale model measurements of B737 antenna pattern by NASA.

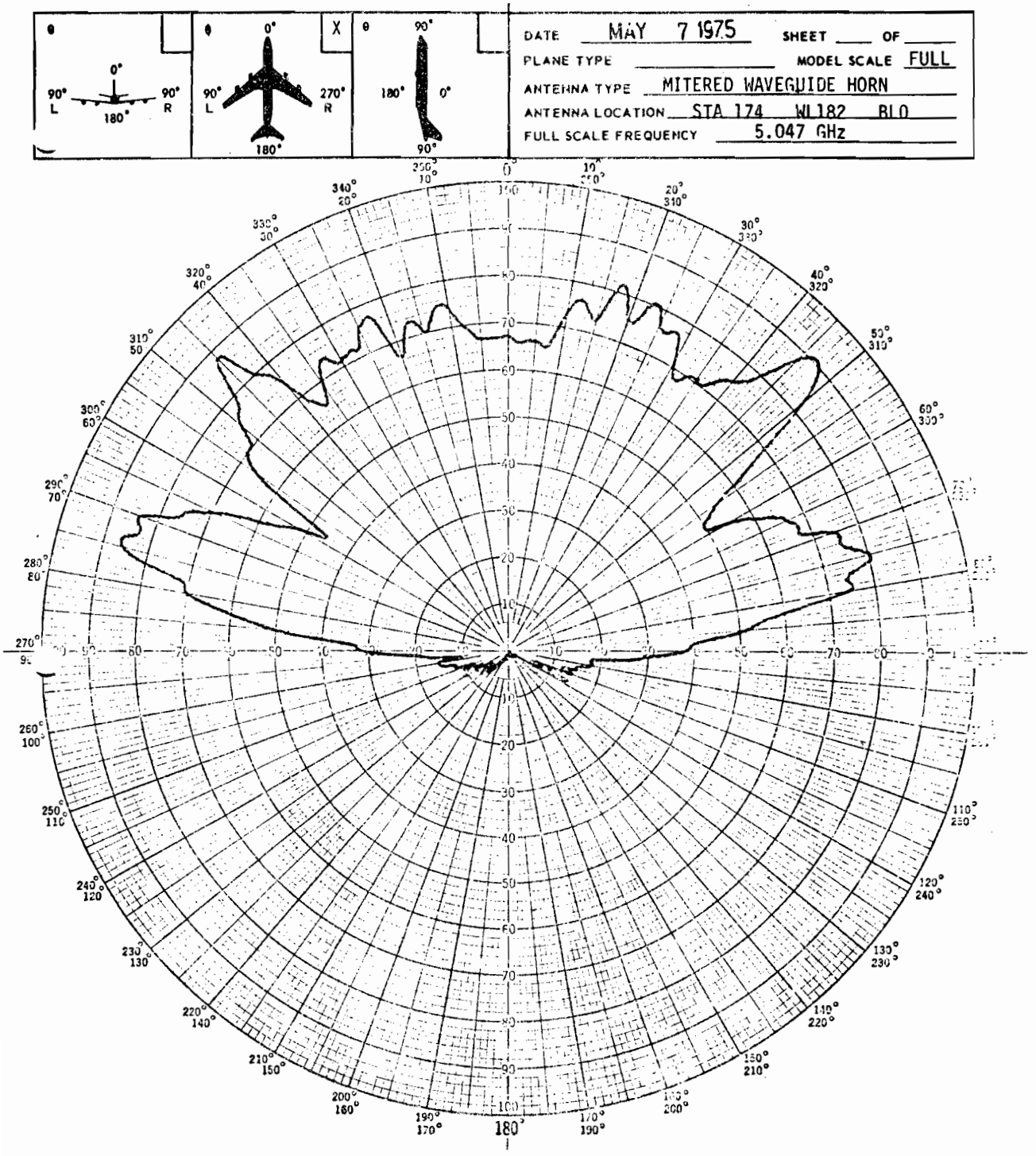

Fig. 9-5. Boeing measured pattern for horn antenna inside B707 radome.

2. in-beam elevation multipath would generate a noisy signal for a few seconds.

Nevertheless, neither of the above situations represents a desirable situation for "normal" MLS operation.

We will examine several factors in greater detail to see what could be accomplished by polarization change and/or TRS feature changes, such as antenna pattern specifications or coverage control. Before doing this, we want to show why azimuthal inbeam and elevation out-of-beam were considered lesser problems. This argument is summarized in Table 9-2.

At this point, it is useful to explore the sensitivity of the power budget to various factors in the budget. First we consider the factors related to choice of polarization.

1. Fresnel Reflection Coefficient and Roughness

These two are considered jointly here because measurements are made of both factors simultaneously and because it is difficult to separate them in the case of corrugated surfaces. In Table 9-3, we summarize the results of the data review in this area.

The data for dielectrics and smooth metal is well understood, and changes relatively slowly with changes in dielectric constant and/or frequency (e.g., L-band to Ku band). However, the corrugated metal sensitivity to surface changes and frequency (especially C vs Ku band) is not as well understood at this point. Thus, the values given in Table 9-3 for corrugated metal should not be regarded as definitive or even "representative" (except in the case of CP).

Table 9.2 Additional Example of "Multipath Budget" for TRSB

	Azimuth In Beam (B727 aircraft reflections at cat I/II DH for basic narrow system)			Elevation Out of Beam (vertical surface)
Fresnel reflection coefficient	0 dB	metal surface	- 4 dB	dielectric surface
Roughness factor	0 dB	smooth metal	0 dB	smooth metal
Size factor	-17 dB	divergence of rays from B727 fuselage	0 dB	large hanger
Path distance factor	0 dB	aircraft near threshold	-3 to -9.5 dB	sep. angle = 2° aircraft at elev. angle of 6° and 3°, respectively
Ground Lobing	-3 dB	typically, ground reflections attenuate fuselage reflections		
XMTR pattern control	-3 dB	when near decision height, scatterer is at a lower elevation angle than receiver	-4 dB	to yield out-of-beam, hanger must be near decision height and hence be at azimuth ≥ 20°
XMTR coverage control	0 dB		0 dB	
Airborne antenna gain	?		?	
M/D at receiver	-26 dB		-11 to -17.5 dB	
Error specification (2σ in dB re 1 deg)	-22.7 dB		_	
ε_{rms}/error spec.	-3.9 dB		_	
Antenna factor	+6.4 dB	2.1° separation angle, 2° beamwidth	_	
Receiver factor	+2 dB		_	
Motion averaging factor	+4.8 dB	$\sqrt{M}$ where M=3	_	
Desired M/D at receiver	-13.43 dB		-1 to -4 dB	Bendix receiver
Margin	+13 dB	Margin	+7 to +16.5 dB	

Surface	Polarization	Angle of incidence: $5° < \theta_i < 10°$ Theory	Meas.	$10° < \theta_i < 20°$ Theory	Meas.	$20° < \theta_i < 60°$ Theory	Meas.
Smooth dielectrics	VP	-1	-1 to -2 ①⑧	-2 to -3	-2 ⑧	-6 to -10	-3 to -10 ②⑧
{wood asbestos, concrete, glass}	HP	-3 to -7	-1.5 to -7 ⑤⑧	-7 to -15	-9 to -20 ③⑧	-15 to -30	-9 to -15 ⑧④
	CP*	-2 to -5	—	-5 to -9	—	-10 to -20	—
Smooth metal	VP, HP	0	+3 ⑤	0	—	0	—
	CP*	-20	—	-20	—	-20	—
Corrugated metal	VP	-1 ⑥	0 to -1 ①⑦	-2 to -3 ⑤	-6 ⑦	-3 to -6 ⑥	-5 ⑦
	HP max spec.	-15 ⑥	-1.5 to -15 ①⑦	-5 ⑥	-15 ⑦	-3 ⑥	-10 ⑦
	HP max any angle	-3 ⑥	-5 ⑦	-5 ⑥	-5 ⑦	-3 ⑥	-5 ⑦
	CP*	-20	—	-20	—	-20	—
	Physical Occurrence	AZ, El at long range only (not common)		Az El at medium range		Az El at DH	

Notes:

* ≈ 3 dB ellipticity

① ITTG corrugated metal and fibre [18]

② " concrete, brick, corrugated asbestos

③ " concrete

④ " brick

⑤ " metal

⑥ three cases numerically calculated by J. Mink

⑦ UK corrugated metal [27]

⑧ " brick and concrete

⑨ " concrete

TABLE 9-3

FRESNEL REFLECTION FACTORS AT C-BAND (in dB)

Practically, it is quite difficult to achieve perfect circular polarization, so an ellipticity ratio ε = +3 dB was assumed in generating these plots (ε = 0 or -3 dB would yield lower CP levels in most cases).

Comparing the three polarizations, we see that both HP and CP offer an improvement over VP in nearly all cases. However, whether or not this improvement is "significant" depends heavily on the assumed environment. If the threat is dielectric surfaces, then in Table 9-1 we would have an isotropic margin of $\approx$ 3 to 15 dB for azimuth out-of-beam and 4 to 15 dB for elevation inbeam multipath with an isotropic airborne antenna.

On the other hand, with smooth metal and many cases of corrugated metal, HP evidently would not provide a significant advantage over VP. And, from Tables 9-1 and 9-3, we see that there is a need for additional margin in the cases of greatest concern.

Circular polarization provides such an improvement for these metallic surface reflections that they should cause no trouble for either situation in Table 9-1. Unfortunately, for dielectrics, CP does not provide such dramatic improvement. However, as long as $\theta_i > 10$, Tables 9-1 and 9-3 suggest that CP would provide an adequate margin for both of the key MLS multipath situations as long as the airborne antenna factor can be held to less than +3 dB.

We see that much of the advantage or lack thereof hinges on the surfaces that may be encountered in the "real world". In Section 9.2, we will get a better handle on the expected distribution of surface types.

Next, we consider some factors under the control of the system designer which represented "soft" numbers in Tables 9-2 and 9-3.

2. Azimuthal Ground Lobing Factor

It will recall from Chapter III (see Fig. 3-6) that this arises because the observed azimuth M/D level depends on ground reflections as well as the two paths considered classically. If, for example, the "direct" signal is reduced by ground reflections when the multipath is enhanced, it is clear that a problem could arise.

The need for a substantial rolloff in the elevation pattern of the azimuthal array at the horizon is a basic tenet of good MLS design to avoid ground lobing. Additionally, the contractors have all advocated siting the antenna close to the ground to avoid nulls at low angles. Thus, it might be thought that this was a nonexistent problem.

However, it was observed that:

(a) the elevation pattern proposed by some MLS contractors could yield significant lobing at low angles. Also, it was not clear that this rolloff (which evidently is based on a phased array of column radiators) would be achieved by the doubly curved reflector which is to be the "basic" TRS azimuth array.

and

(b) although the azimuth antenna may be sited fairly close to the the centerline runway surface* (e.g., phase center at 4'-5'), when the aircraft is off centerline, the antenna phase center could be 7'-10' above the reflecting terrain since the terrain to the side of the runway often is 3'-5' below the runway CL elevation. This height differential also leads to the possibility of ground reflections enhancing the multipath.

---

*There exists some question as to how easily a low siting can be achieved in practice when lights (see ref [3.70]) etc., are considered.

This factor does not represent a propagation "invariant", but rather it is a cost/performance tradeoff decided by the system chooser. To give some feeling for the numbers involved, Fig. 9-6 shows an upper bound to this ground lobing factor as a function of horizon pattern rolloff.

3. Airborne Antenna Gain

Presumably a close to isotropic airborne antenna pattern could be achieved by use of several antennas, etc., by all users if they were willing to pay the price. However, it seems unlikely that this will occur in practice. The question that must be faced by the ground system designer is how much margin should be allocated to this factor in the "multipath" budget.

A key parameter in assessing this for an actual airborne antenna pattern is the separation angle between the multipath and direct path as seen from the airborne antenna. For an aircraft far away from the hangar and transmitter (e.g., as during acquisition and/or the curving portion of an approach):

$$\phi_{sep} \approx \frac{y_{offset}}{R} (\cos \alpha - \sin \alpha / \tan \theta)$$

where y_{offset} = hangar offset from centerline

R = range of aircraft from transmitter

α = azimuth of aircraft relative to centerline

θ = azimuth of hangar relative to centerline

To get some feeling for the numbers involved, we consider two examples:

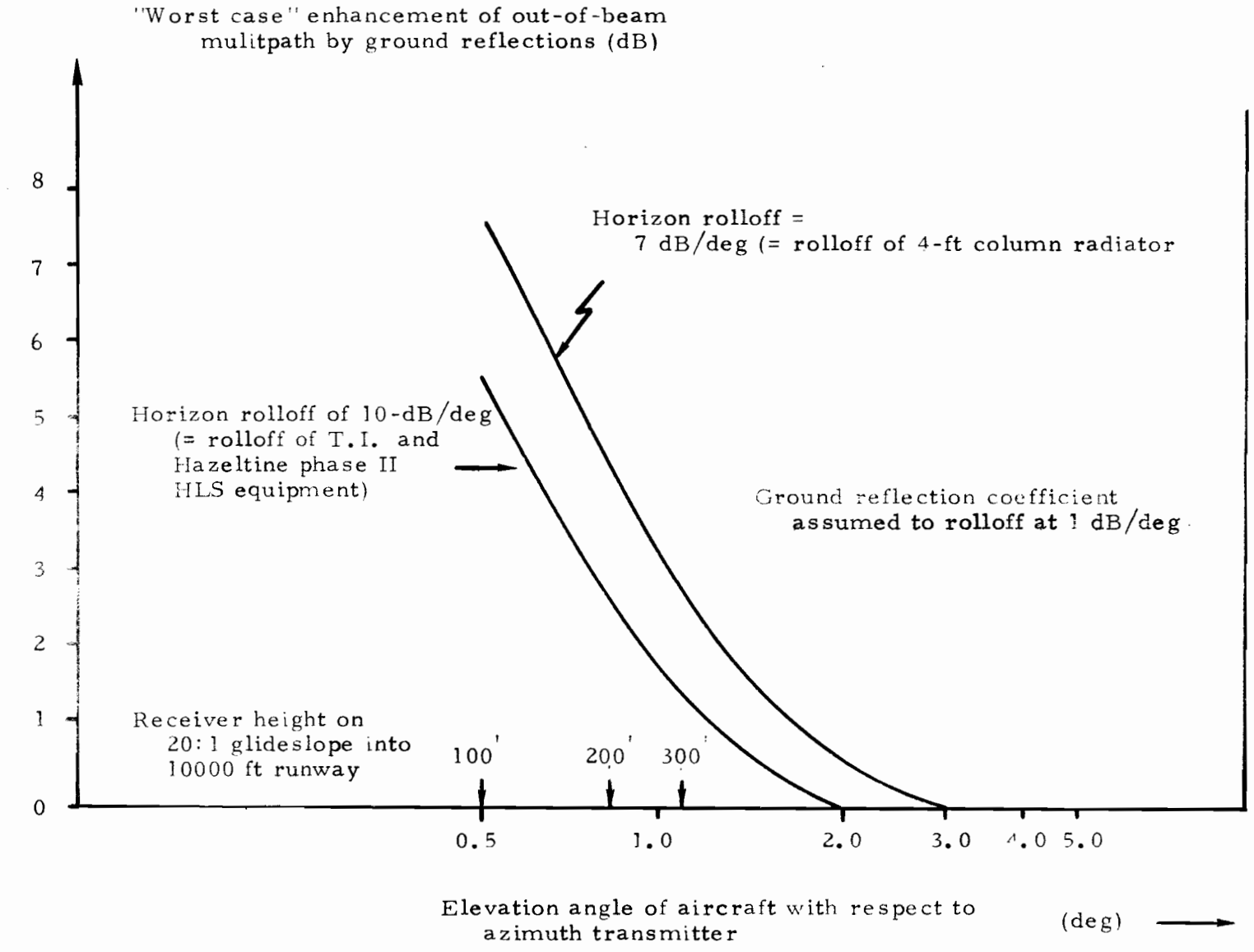

Fig. 9-6. Ground reflection enhancement of out-of-beam multipath for several azimuthal antenna elevation pattern slopes.

Case 1

Parallel hangar at +30° azimuth with 1500-foot offset generating multipath for aircraft at -30° azimuth.

R(nmi)	α_{sep}(deg)
5	4.9
10	2.4
20	1.2

Case 2

Nonparallel hangar located at +14° azimuth with 1,000-foot offset generating multipath at -40° azimuth

R(nmi)	α_{sep}(deg)
5	6.3
10	3.1
20	1.6

In Figs. 9-2 and 9-3 we observed several dB changes in airborne antenna gain over 5° intervals. Thus, there could be a problem if patterns no better than Figs. 9-2 and 9-3 are realized with MLS antenna installations.

On final approach, the direct signal is generally with $\pm$ 10° bearing with respect to the aircraft nose, while multipath could be expected at all bearings up to $\pm$ 60°.

9.2 Properties of Building Surfaces at Civilian Airports

In the preceding section, we have seen that the building surface composition plays a key role in determining the multipath level for a given polarization. Aircraft of a given type are quite uniform in this respect, but buildings differ quite substantially. To obtain a better handle on the expected mix of surface types, a survey was made of the buildings posing

multipath threats at eight major civilian airports (JFK, PHL, ORD, LAX, SFO, MIA, TUL, MSP). The results are summarized in Table 9-4 (drawn from ref [36]). We see that corrugated surfaces are by far the most common with nonmetallic dielectrics comprising the bulk of the remaining buildings.

Periodic corrugated surfaces have the peculiar property of yielding specular reflections at several angles of reflection for a given angle of incidence[72-75]. The angles of reflection related to the angle of incidence by

$$\sin \theta_{r,k} = \sin \theta_i + k \lambda/d \qquad k=0, \pm 1, \pm 2 \tag{9-5}$$

where d/λ is the spatial period of the corrugation in wavelengths and k, the mode number, assumes values for which the right-hand side of (9-5) is less than unity.

The power reflected in a given mode depends on the angle of reflection, polarization, corrugation type and mode. For metallic surfaces, the sum of the reflected power in the various modes is equal to the incidence energy, but the distribution of power between the various reflected modes can differ significantly for the various polarizations. In Figs. 9-7 to 9-9, we show the results of calculations made by Dr. J. Mink (ECOM) for the sinusoidal and rectangular corrugations encountered most commonly in the airport survey. For circular polarization, it was found that virtually all the power reflected had reverse sense polarization, so that the effective reflection coefficient would be less than -20 dB for a 3 dB ellipticity ratio.

TABLE 9-4

SURFACES CATEGORIZED FOR EACH AIRPORT IN FAA SURVEY [66]

Airport	Buildings	Surfaces	Corru-gated	Cinder Block	Brick	Concrete	Smooth Metal
JFK	19	28	13	3	7	1	4
PHL	12	17	11	3	2	1	
ORD	14	19	14	1	4		
LAX	11	15	9	1		4	1
SFO	4	4	3		1		
MIA	17	20	10	6	1	3	
TUL	10	12	9	2	1	1	
MSP	6	8	5	1		1	1
	93	123	74†	17	16	11	6

†24% essentially flat (and are expected to reflect similar to flat surfaces)

12% sinusoidal with spatial period 2.75 inches and height 0.25 inches

15% trapezoidal with spatial period 8.0 inches, top and bottom segments 2.0 inches wide and height 0.75 inches

8% rectangular with spatial period 6.0 inches, top width = 4.0 inches and height 1.5 inches

remainder requires 17 categories, most of which appeared at one or two airports.

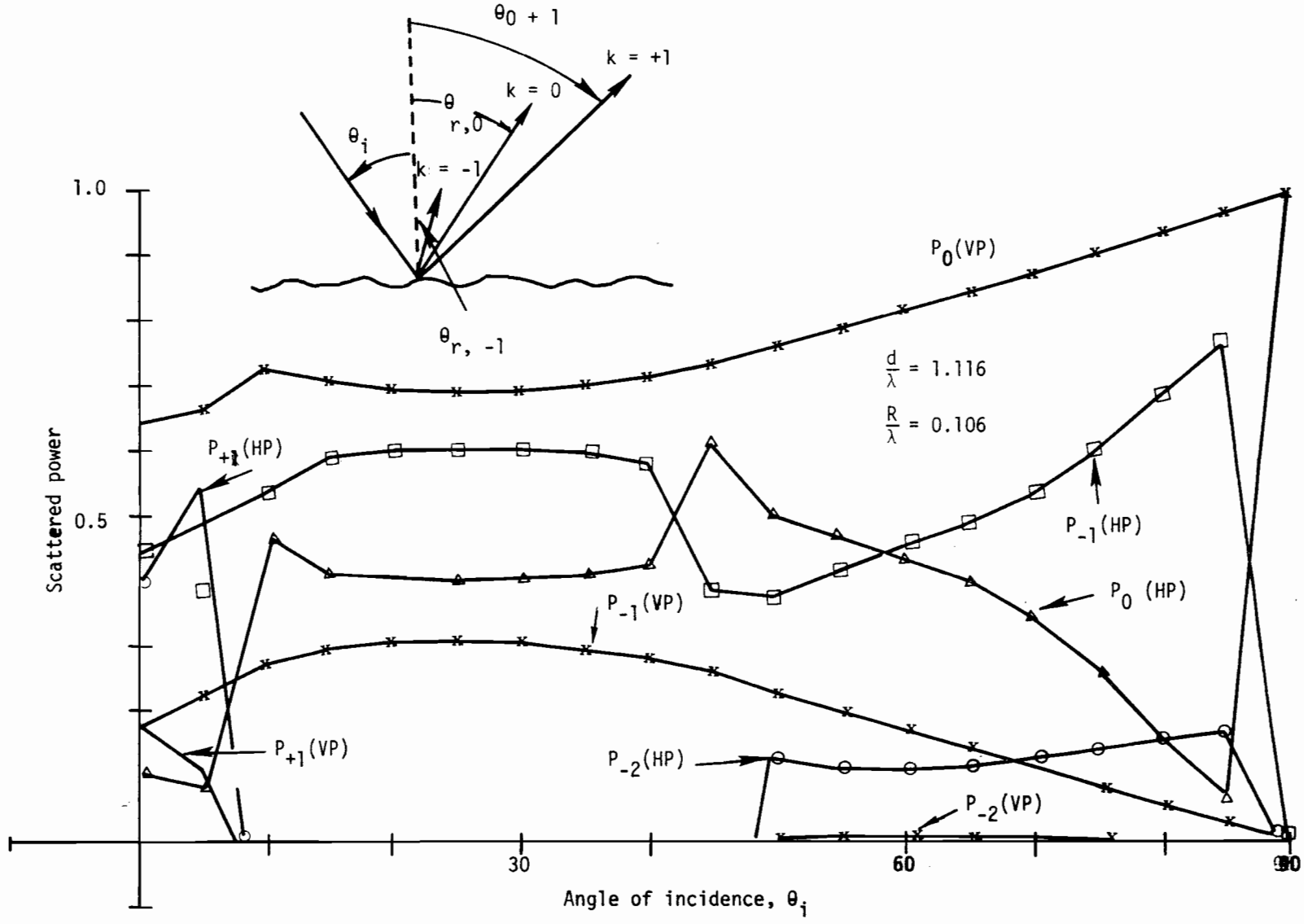

Fig. 9-7. Computed power in various reflection modes for the most common sinusoidal corrugation in the airport survey.

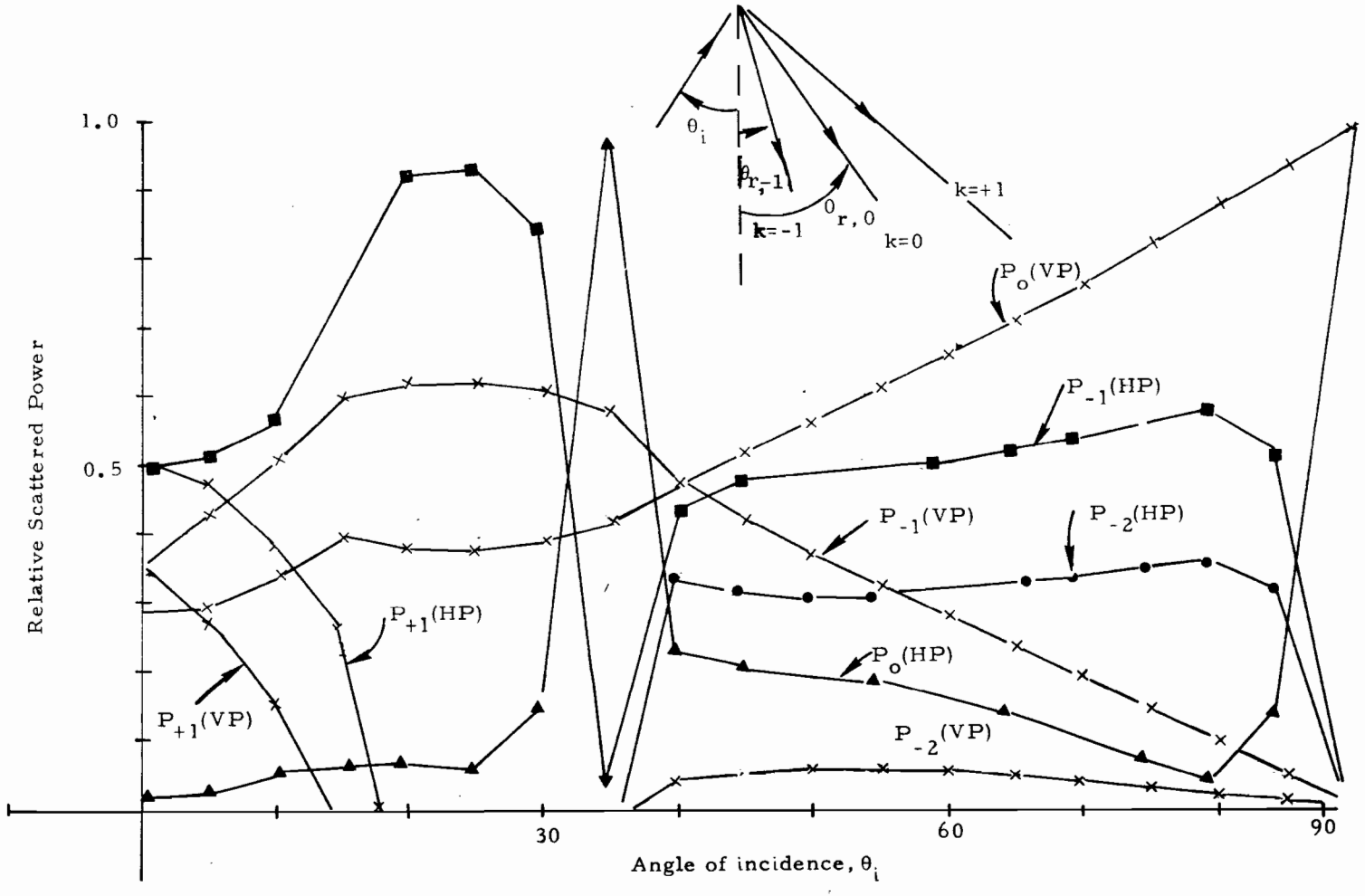

Fig. 9-8. Computed power in various reflection modes for the second most common sinusoidal corrugation encountered in the airport survey.

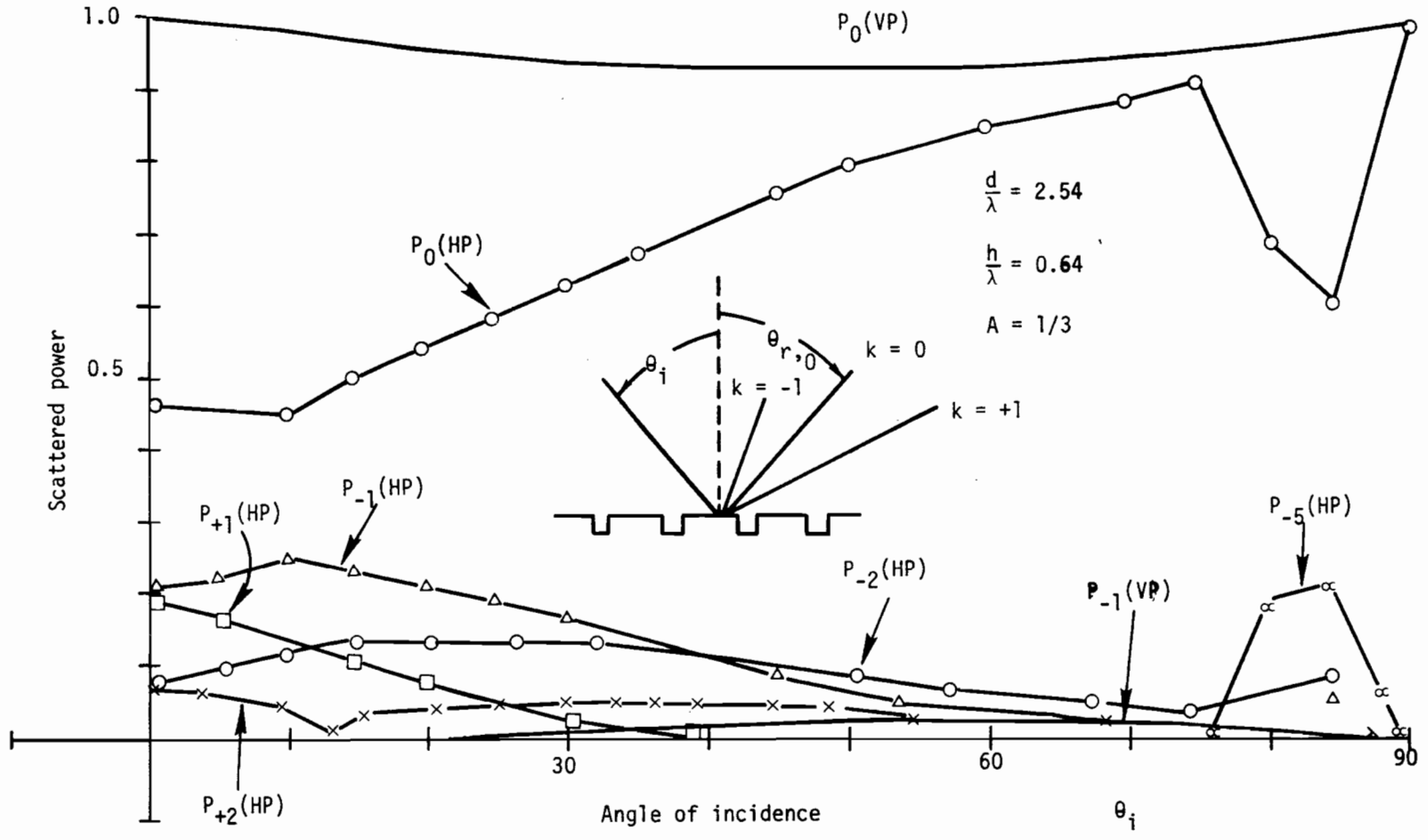

Fig. 9-9. Computer power in the various reflection modes for the most common rectangular corrugation encountered in the airport survey.

Figures 9-7 to 9-9 suggest that HP generally yields less power in the zero-th order mode than does VP; but it is not clear at this point whether the increased power in the other modes for HP would lead to new problems. Preliminary studies suggest that often the HP power goes into a (relatively harmless) mode in which the reflection goes back towards the transmitter; however, a much more detailed study considering representative building locations is in order.

It appears from Tables 9-1 to 9-4 that a change from vertical polarization to horizontal polarization would produce 3 to 6 dB or reduction in received M/D ratio for 80% of the surfaces encountered in the airport survey as long as only the zero-th order mode from a corrugated surface is of greatest concern. However, in the 20% of cases which should reflect much like a flat, metal plate and hence represent the greatest problem, only circular polarization would yield a substantial reduction in M/D levels. And, in the remaining corrugated surfaces (46% of the sample), CP would also yield a very large (e.g., 20 dB) improvement.

For the remaining 36% of the cases, CP would furnish some improvement (3 to 6 dB) over VP, but not as much as HP. Thus, if the objective is to achieve the greatest lower bound on received M/D ratio reduction for the surveyed airports by a change of polarization, it seems that circular polarization represents the best choice.

9.3 Preliminary Conclusions and Issues to be Resolved

As a result of the systems studies reported in this chapter together with the critical areas studies of the preceding chapter, we have drawn the following preliminary conclusions:

(1) the only possibly important multipath challenges to successful TRSB operation are building reflections yielding inbeam elevation multipath or out-of-beam azimuthal multipath.

(2) for the nominal case, there is generally a positive multipath margin; however, several factors could conceivably vary enough from the "nominal" case to result in negative multipath margins.

(3) if a greater margin is to be obtained by change of polarization, circular polarization appears to offer the greatest benefit since it yields an improvement over vertical polarization in all cases whereas horizontal polarization yields no improvement for cases involving flat or nearly flat metal surfaces [these essentially flat surfaces yield the worst multipath challenge and are relatively common (20% of the cases in a survey of 8 major airports)].

(4) the principal remaining uncertainties are:

   (a) airborne antenna pattern differential gain characteristics

   (b) quantifying the likelihood of surfaces with worse than "nominal" reflection characteristics also having bad geometrical orientations

   (c) the extent to which system purchasers will incorporate system options such as greater elevation array centerline emphasis and/or azimuthal coverage control in their equipment.

Most of the conclusions above follow in a straightforward manner from the results of the preceding sections. A few comments should be made, however, about the TRSB options involved in point (4). Concerning pattern control, it is fairly straightforward with some antenna implementations to obtain an increased centerline emphasis and/or a nonsymmetrical antenna pattern with less gain on the side toward the offending hangar. Although this might be thought to be at the expense of usable guidance near the coverage limits, it should be noted that reflections from a given sector necessarily imply shadowing in that same sector. We have not addressed the cost required to achieve several more dB of pattern control.

For the azimuth out-of-beam-case, coverage control in the sense of coverage limitation always represents a viable possibility. An interesting alternative for the problem described here is to utilize power programming as a function of azimuth angle as was done with the Texas Instruments hopover feature. This involves smoothly reducing the power in the "bad" sector by several dB (e.g., 6-10 dB) and then increasing the transmitted power once past the bad sector. The level of complexity is less than that for MCT and it has the advantage of continuing to furnish usable guidance in the "bad" sector. We have not addressed the integrity aspects (monitoring) of power programming.

X. STUDY OF TRSB "D" ELEVATION SYSTEM AT FRIENDSHIP INTERNATIONAL AIRPORT

One of the principal applications for the computer simulation described in the earlier chapters is its use in site studies to determine the appropriate MLS configuration (e.g., basic "wide" or "narrow") and siting. In this chapter, we describe the results of such a study in support of proposed tests of the Texas Instruments TRSB "D" elevation system at runway 15 at Friendship International Airport (Baltimore, Md). Our objective here is to provide a concrete real world example of

1. using the receiver test programs to give an initial optimization of the performance of the installed system,

and 2. performing full system simulations using a model for the airport environment (buildings, aircraft, and ground terrain) developed from FAA furnished airport maps and building plans.

The objective of the proposed tests was to demonstrate the ability of MLS to function well at a site which would be very difficult for an ILS glideslope due to the limited terrain available. The T.I. system has a beamwidth 2-3 times larger than that contemplated for phase III prototype equipment; thus it was proposed to use MCT to yield better low angle accuracy. However, this use of MCT differs somewhat from that considered in flare studies in that no receiver correction is to be made for the MCT truncation error.

The next section describes the optimization of MCT parameters for the T.I. D system. Section 10.2 describes the airport terrain model.

The results of three representative system runs are given in Section 10.3. It appears that with an appropriate choice of transmitter location, adequate accuracy would be achieved on the 2.86° glideslope with ground reflection multipath yielding predominantly a path following error $\leq$0.06° which is well within the MLS functional requirement specification of 0.1°. However, at lower angles (e.g., 2°) on a transmitter location in front of rising terrain, very large errors (0.7°-0.4°) may occur due to ground reflection multipath.

10.1 Optimization of Texas Instruments' "D" System MCT Performance

A model for the Texas Instruments demonstration D EL1 system (using MCT) was developed* so as to optimize its performance in scenarios based on runway 15 at Friendship Airport (Baltimore, MD). Figure 10-1 shows the beam pattern for this antenna with no MCT. Since the beamwidth is approximately 2.9°, the general rule of thumb that ground reflection multipath should be kept 2 beamwidths away from the direct signal suggests that significant ground reflection errors would be encountered for aircraft elevation angles below 2.9°. To achieve useful guidance down to the desired angle of 1.3°, Texas Instruments proposed using MCT to reduce the ground reflection multipath effects. Figure 10-2 shows received envelopes in absence of multipath for several receiver elevation angles.

This system differs from that considered in flare studies in that the receiver probably will not apply a low angle correction to reduce scan truncation effects. Consequently, a study of the multipath characteristic was needed to determine the best choice of MCT initiation angle. Figure 10-3

*The "development" consisted of changing the beam pattern in the general TRSB model described in Chapter II and disabling the MCT correction feature.

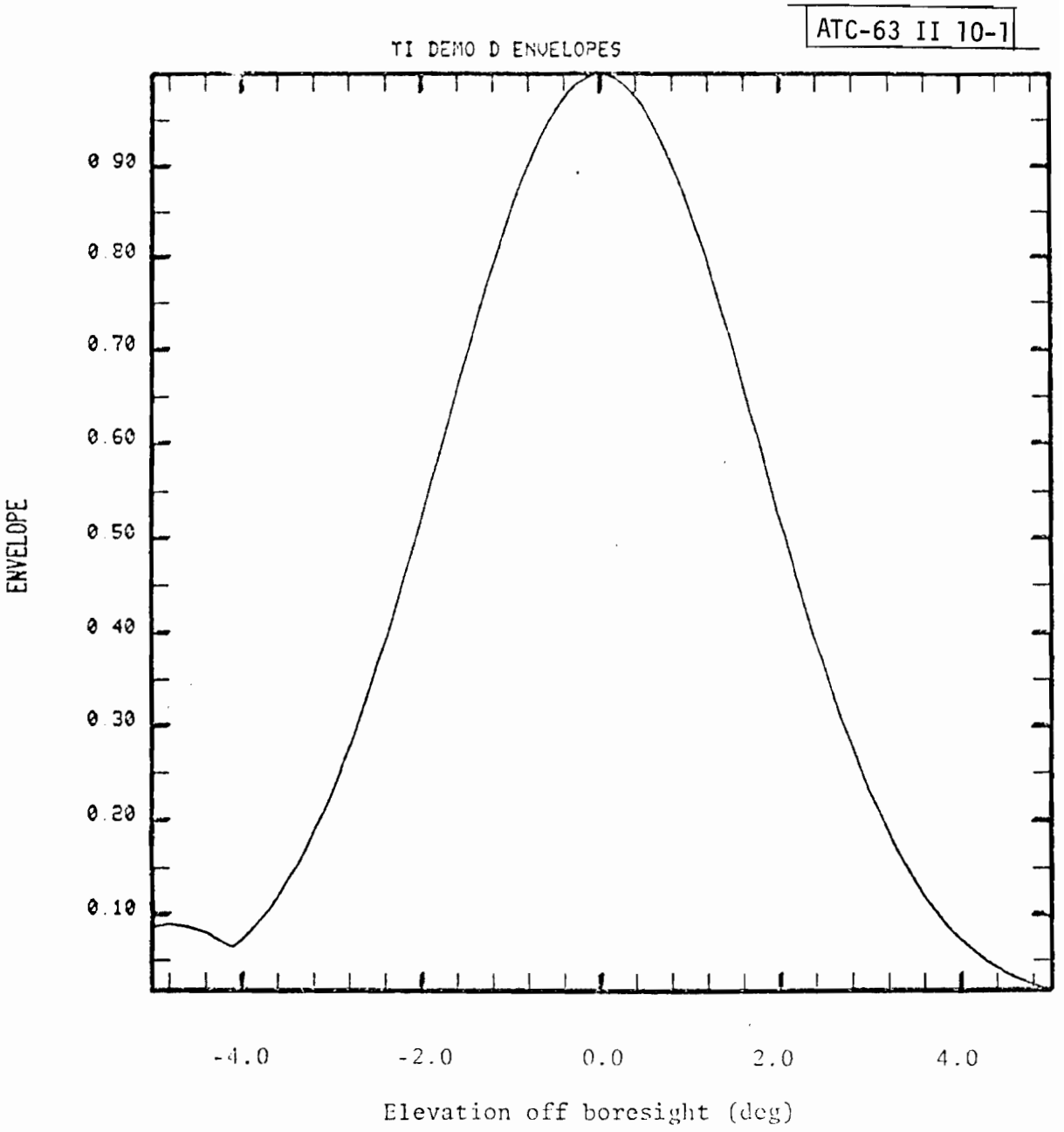

Fig. 10-1. TI demo D elevation pattern without MCT.

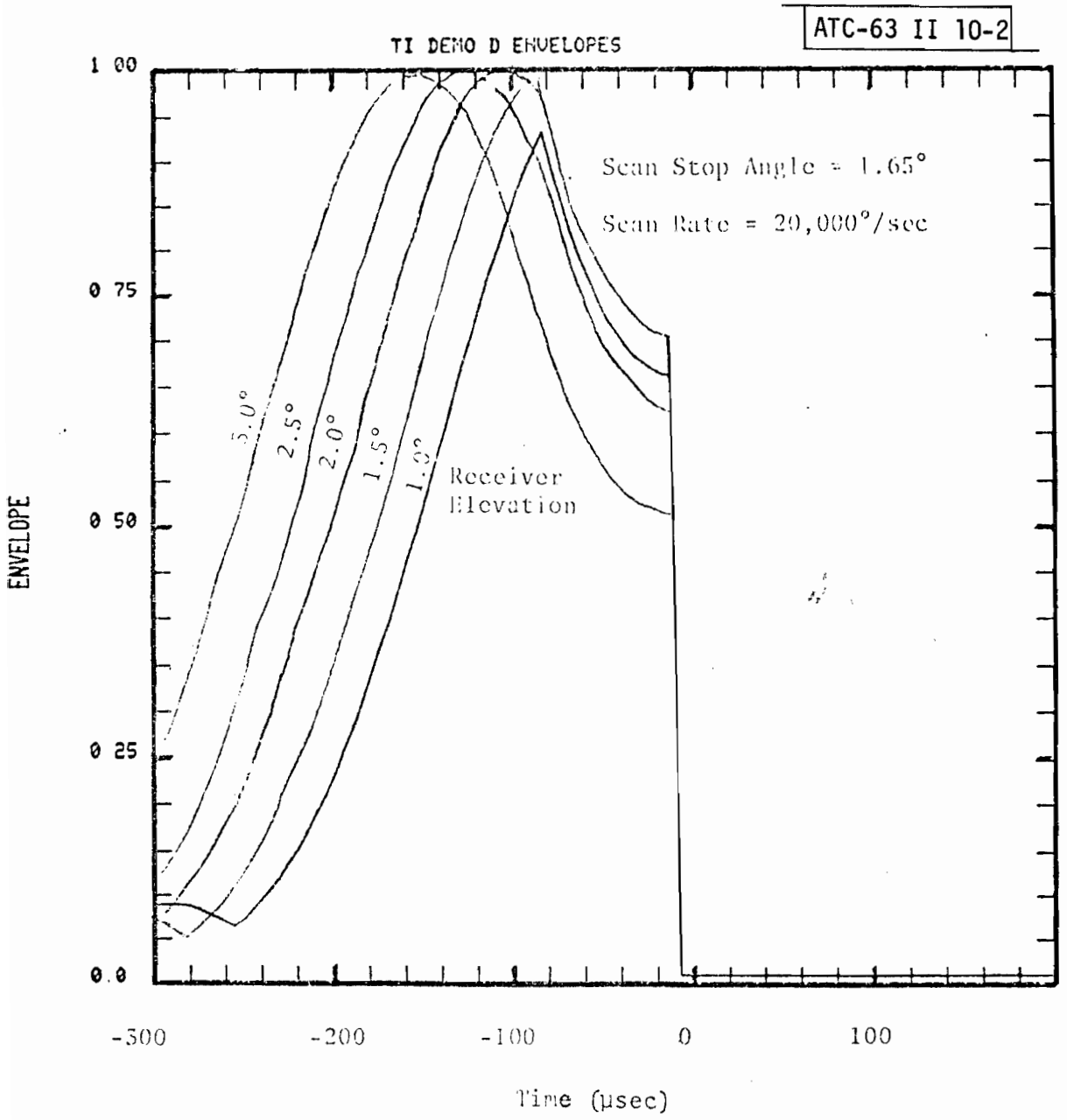

Fig. 10-2. TI demo D elevation patterns with MCT.

gives the peak multipath error for zero degrees rf phase for a single multipath component as a function of separation angle and the MCT initiation angle.

Figure 10-3 clearly shows the tradeoff between MCT truncation error and ground reflection multipath error. When the MCT initiation angle is above the aircraft angle, the multipath error has essentially been eliminated, but there is a large truncation error. For MCT initiation angles at or below the aircraft angle, the truncation error is negligible, but there is an appreciable multipath error for separation angles up to ≈ 2 beamwidths.

Texas Instruments has proposed using the system with MCT starting at an elevation angle of 1.65°. From Figure 10-3, we see that:

(a) for an aircraft at low elevation angles (e.g., 1.4°) over flat terrain, using an MCT stop angle of 1.65° reduces the peak error due to a -6 dB ground reflection from ≈0.5° to ≈0.25°.

(b) for an aircraft on a glideslope of 2.86° over flat terrain, an MCT stop angle of 1.65° reduces the peak error due to a -6 dB ground reflection from ≈0.02° to ≈0.00°.

In the full system simulations, it was assumed that the MCT initiation angle was 1.65°.

The azimuthal pattern assumed for the array is shown in Figure 10-4. The phase center of the array was taken to be 6 feet above the local ground.

Although the airborne antenna on the DC-6 under consideration is a forward looking horn inside the radome, for the purposes of this simulation it was assumed that the airborne antenna was omnidirectional. Since the

Geometric relationship between MCT performance parameters.

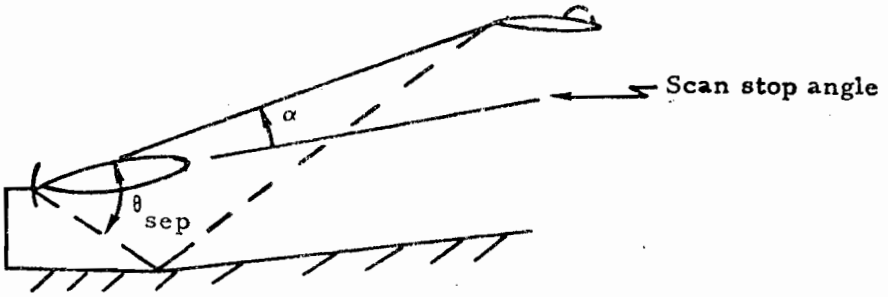

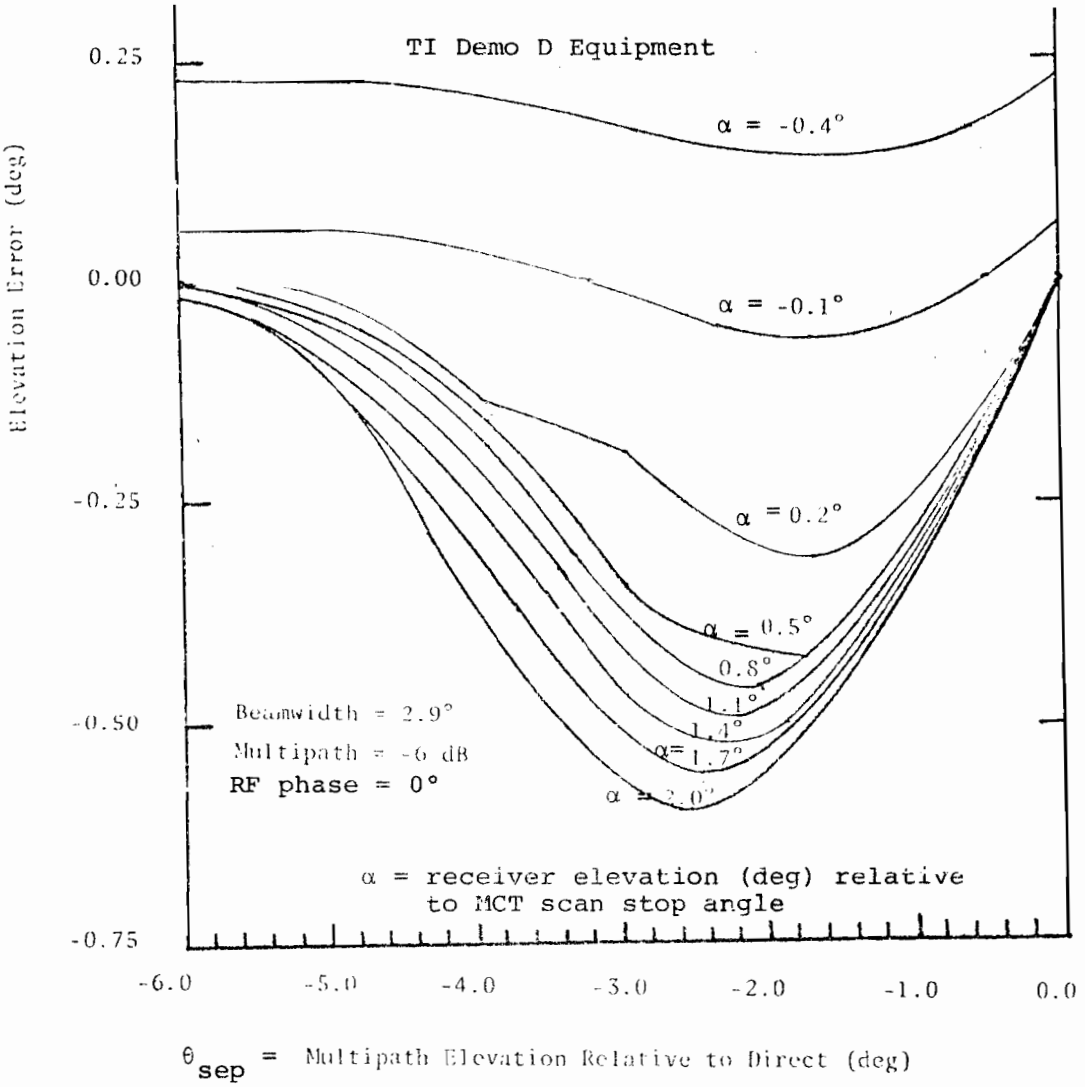

Fig. 10-3. Elevation error vs separation angle: no MCT correction in receiver.

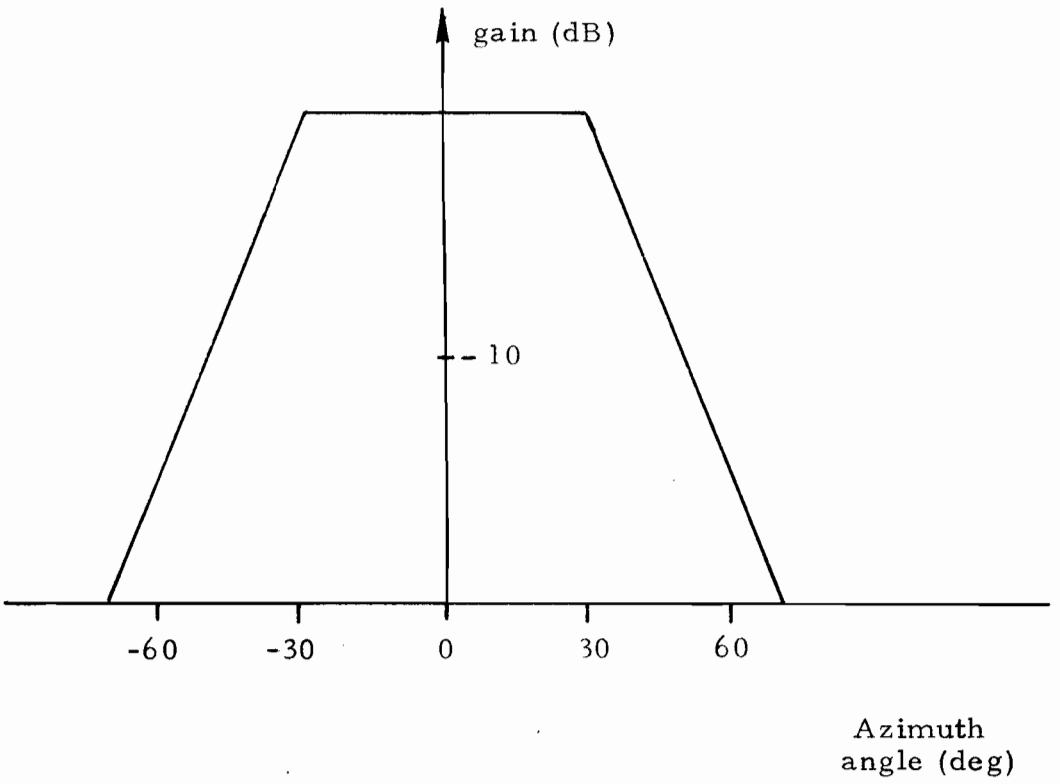

Fig. 10-4. Azimuth pattern assumed for TI demo D elevation system.

elevation multipath predominantly came from ground at this location, there should be little difference between directional and omni aircraft antenna performance.

10.2 Airport Multipath Environment

Figure 10-5 is a map of the end of runway 15 at Friendship International Airport, Baltimore, Maryland. The FAA suggested an MLS site on the opposite side of the runway from the present ILS glideslope. We see that this site is next to a very steep dropoff into a gully paralleling the runway, and thus would be impractical for ILS glideslopes which rely on the terrain to generate the beam. This flexibility of MLS is of aid here in that it places the MLS on the opposite side of the runway from the holding area, so that aircraft waiting to take off should be able to hold much closer to the runway threshold during IFR conditions.

A site survey by FAA personnel found that:

1. hill #1 is heavily vegetated, such that (based on experience in the DABS program), negligible multipath is expected from it.
2. the buildings in area #1 are not visible from the contemplated EL1 site.
3. the buildings in area #2 have brick walls approximately 12 feet high. Hand calculation showed they will yield negligible multipath levels.

These features of the actual airport were not represented in the simulation.

Building drawings obtained from the Westinghouse Corp. showed that:

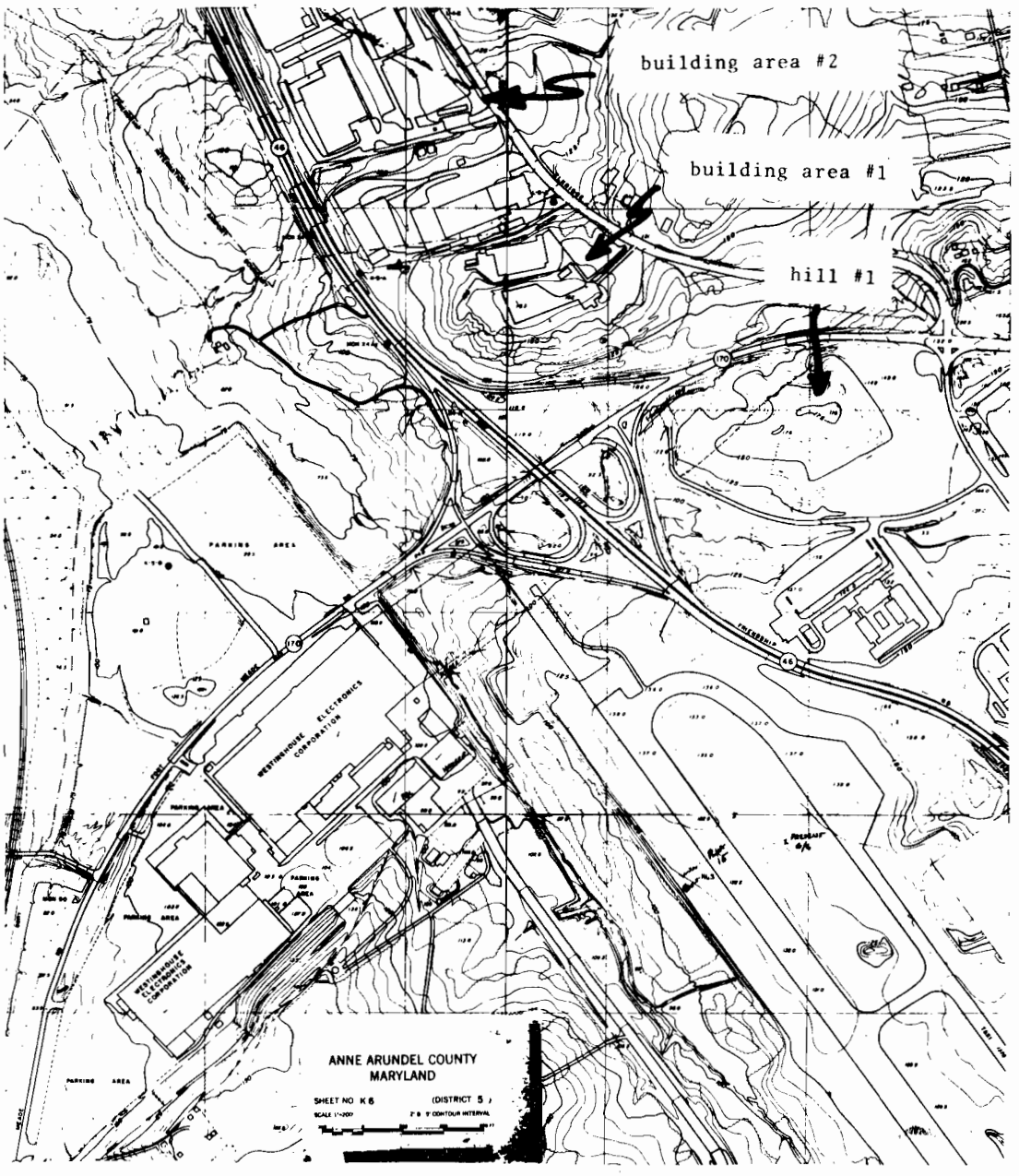

Fig. 10-5. Runway 15 at Friendship International Airport (Baltimore, Maryland).

1. although the hangar is fairly high ($\approx$ 50 feet), the side which would yield EL1 reflections for an aircraft making a straight-in approach is a cylindrical section whose angular span is 64°. Since all points on this are inclined at least 58° with respect to the vertical, it turns out that the reflections will pass well over the top of the hangar.

2. the penthouses on the aerospace building are visible from the EL1 site and are fairly high (50 feet). One penthouse is wood covered with fiberglass, while the other is metal covered with fiberglass. To be conservative, the entire building was represented as a smooth metal surface.

3. the other buildings in the Westinghouse area are either too low to be visible and/or are shielded by the hangar and aerospace building penthouses.

No information was available regarding the location of aircraft during IFR conditions. To be conservative, three B747 aircraft were positioned on the taxiway in the positions shown in Figure 10-6.

The ground near the EL1 antenna is rather complicated in that portions slope upward toward the threshold and/or sideways toward the gully. For purposes of the computer simulation, the ground was modeled by five rectangular plates and two triangular plates shown in Figure 10-6. The coordinates of the various plate corners are given in Table 10-1. This rather large number of surface elements was used because the T.I. D system is rather sensitive

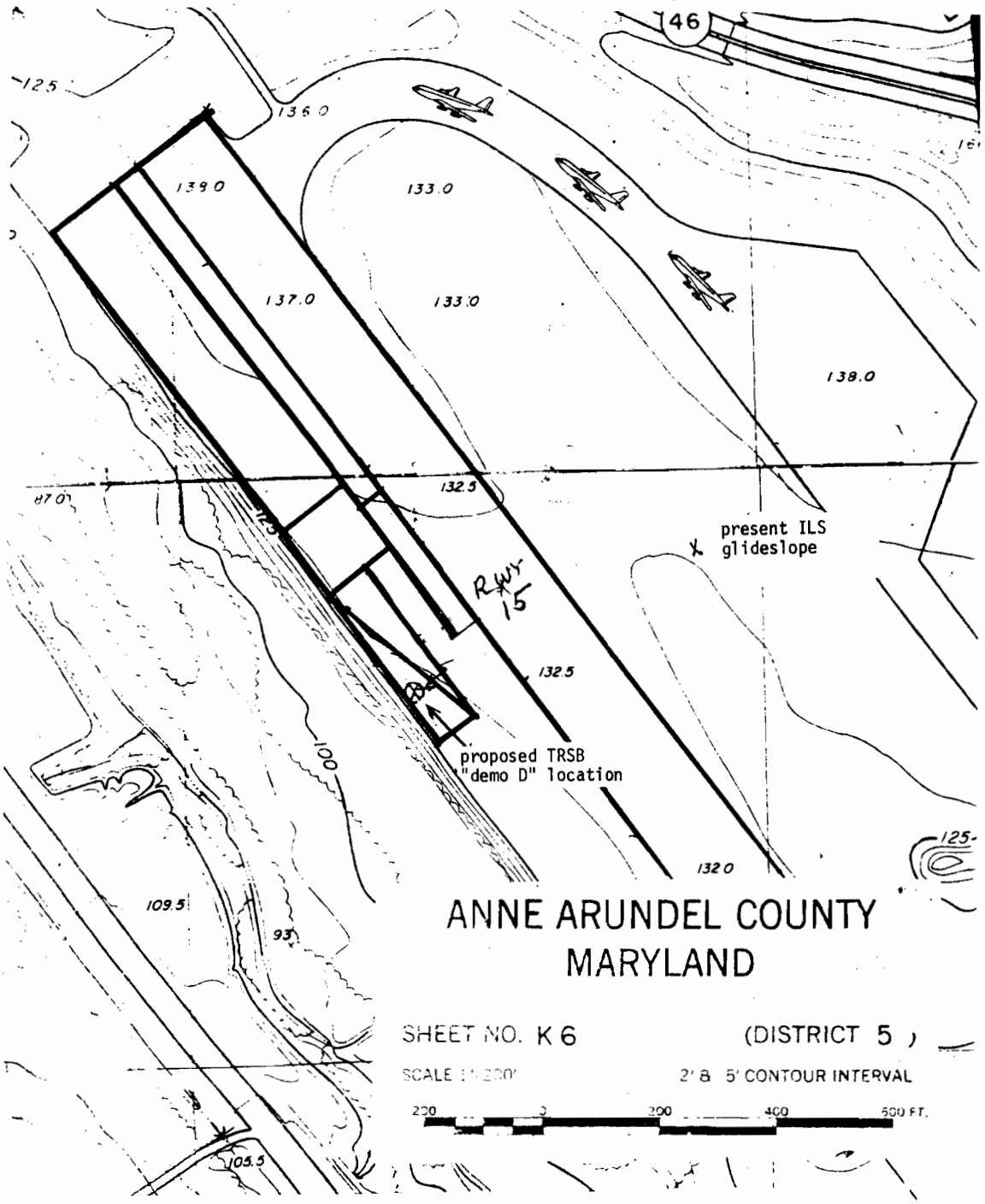

Fig. 10-6. Locations of aircraft, ground terrain plates and EL-1 transmitter for MLS simulation of Baltimore runway 15.

TABLE 10-1

PLATE LOCATIONS FOR GROUND TERRAIN

Rectangle	corner 1			corner 2			corner 3		
	x	y	z	x	y	z	x	y	z
1	0	-75	5 (132.5)	0	75	5 (132.5)	2000	75	10 (137.5)
2	1200	125	5 (132.5)	1200	260	0.0 (127.5)	1350	260	2.5 (130)
3	1350	260	2.5 (130)	1350	125	7.5 (135)	2000	125	7.5 (135)
4	1025	75	5 (132.5)	1025	125	4 (131.5)	1300	125	7.5 (135)
5	1300	125	7.5 (135)	1300	75	105 (137.5)	2000	75	10 (137.5)
Triangles									
1	912	175	2.5 (130)	1200	260	2.5 (130)	1200	175	5 (132.5)
2	912	175	2.5 (130)	912	260	-2.5 (125)	1200	260	2.5 (130)

x is distance along centerline in feet (runway end = 2000')

y is distance from centerline in feet

z is distance above 127.5' field elevation

( ) denotes field elevation

to upsloping terrain for an aircraft on a 3° glideslope;* for instance, an upslope of 5 feet in 3,000 feet could reduce the separation angle from 6° to 4°, which in turn (see Figure 10-3) would yield quite substantial errors.

The terrain off the runway is currently 6-inch high grass, which should yield rather low reflections (the UK measurements suggest a reflection coefficient of ≈0.35). However, to be conservative, it was assumed that the ground might be covered with flat, fresh snow whose dielectric constant was $\varepsilon = 3 + j0.6$. The runway was taken to be flat concrete with dielectric constant $\varepsilon = 7 + j0.0$.

10.3 Simulation Results

Two full scale simulation runs were made: a standard approach on a 2.86° glideslope (20:1) which is the current ILS glideslope at runway 15 and a straight-in level flight at 2,000 feet covering elevation angles from 1.3° to 8°. Each of these will be described in some detail below.

The location along the runway was dictated by the desire to have the MLS glideslope coincide with the current ILS glideslope. The ILS is located at x = 900 at a field elevation of approximately 130 feet, which yields a GPIP on the runway of 900 + 2.5 x 20 = 950 feet (since the runway is at field elevation 132.5). Two possible locations for the D system were considered:

(1) on the 130-foot field elevation contour, which yields

x = 1020 and y = 225 for coincident glideslope

*An MLS basic system would not be sensitive to this, since the beamwidths are on the order of 1 to 1.5° versus the 2.9° of the T.I. D system.

(2) with an offset of y = 250 at the 127.5-foot field elevation,

which yields x = 970 for coincident glideslopes

For the glideslope runs, runs were made for both transmitter locations, while the level flight simulation only considered position (1).

(a) Simulation of Final Approach Along a 2.86° Glideslope

An aircraft approach velocity of 200 feet/second* was assumed with the multipath being computed every 40 feet along the glideslope from (9950, 0, 455) to (1950, 0, 55). Figure 10-7 shows the computer drawn airport map of the runway environment for transmitter position 1 (x = 1020, y = 225). The aircraft are denoted by the symbols A1, A2, A3 while the Westinghouse building is symbol B1. The various ground terrain plates, rectangular and triangular, are denoted by the symbols R and T, respectively.

The table below the airport map gives the peak multipath amplitude of the direct signal (in dB) wrt to each scatter (G = ground), the altitude (in feet) at which this occurred and the scalloping rate (in Hz) at the peak amplitude point.

Figure 10-8 gives a more detailed view of how the multipath amplitude (ρ) and separation angle (ϕ_{sep}) varied along the flight path. There is a small contribution from the building at 450 feet altitude, but that the ground reflections are much larger throughout the flight. The aircraft reflections never exceed -40 dB and hence are not shown in Fig. 10-7. The ground reflection characteristics are essentially constant because the specular point hardly varies for an aircraft on a constant glideslope.

*The error was hardly affected by aircraft velocity since the dominating ground reflections have a very low scalloping rate.

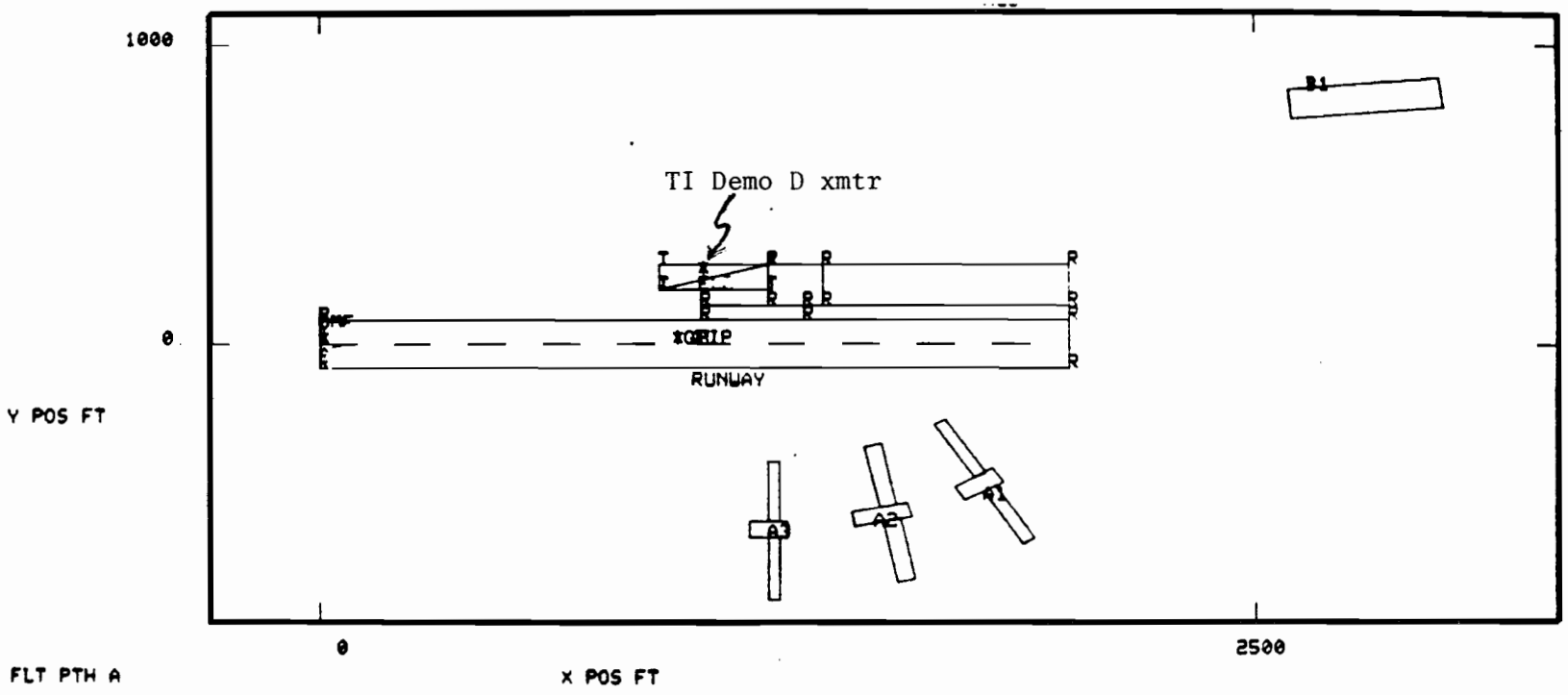

EL SYSTEM

OBST	RANK	AMP	ALT	RDOP
G	1	2	65 0	0
B1	2	36	454 6	-51
A1	3	20	454 6	0
A2	4	80	454 6	0
A3	5	80	125 0	-993

Fig. 10-7. MLS computer simulation airport map: transmitter location #1.

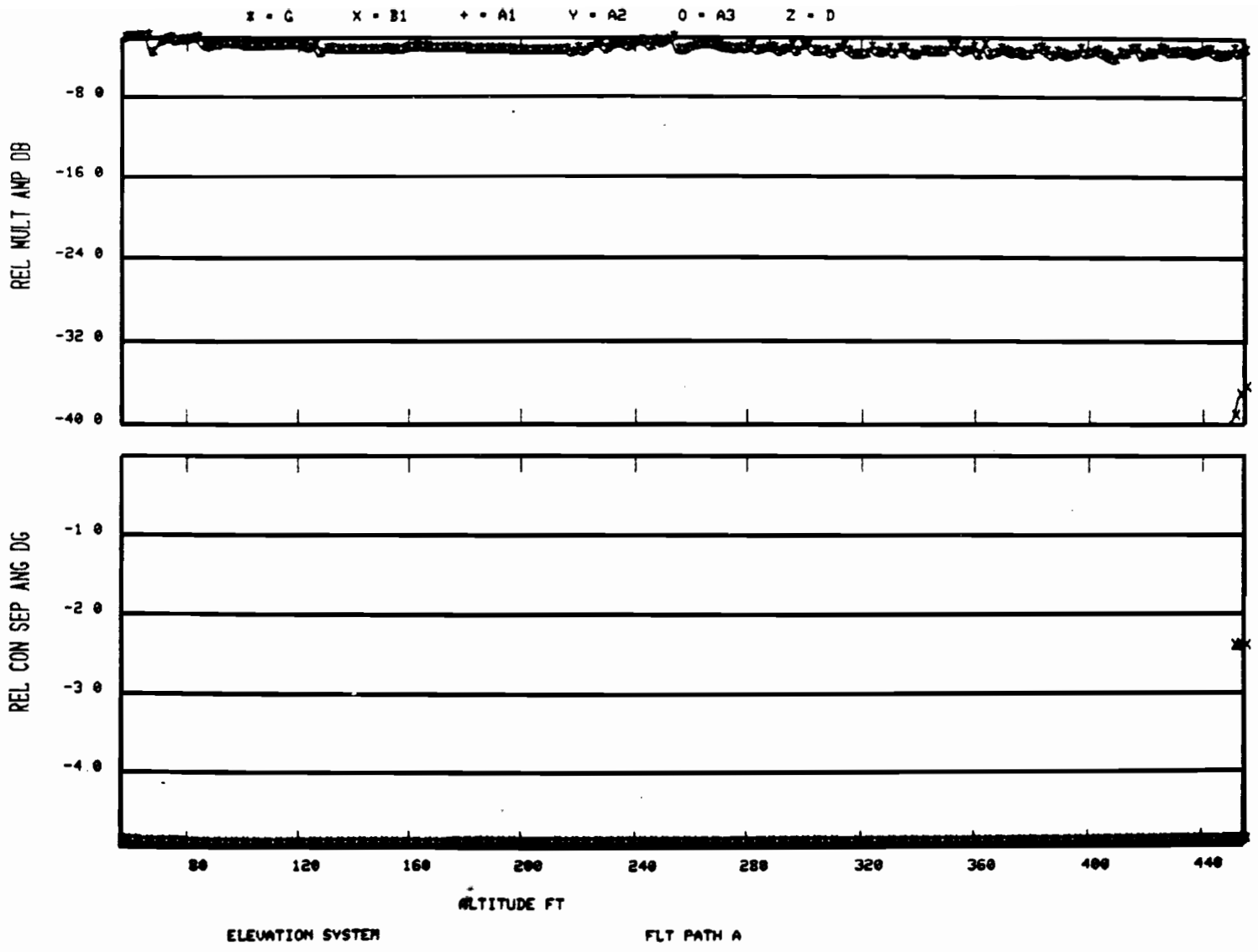

Fig. 10-8. Elevation multipath magnitude and separation angle on 2.86° glideslope for transmitter location #1.

Figure 10-9 shows the elevation error in degrees along the flight path. We see that there is a very slowly varying error that increases from 0.04° to 0.06° as the aircraft approaches threshold. This error change is probably due to a change in rf phase between the direct and ground reflected signal as the aircraft nears threshold since ρ and ϕ_{sep} are essentially constant. Figure 10-3 suggests a worst case peak error of (0.05°) (1.414) = 0.707° for ρ = -3 dB and $\phi_{sep} \approx 4°$, which agrees quite well with the results in Figure 10-7.

Since the error in Figure 10-9 varies so slowly (50 feet in altitude correspond to 5 seconds of flight time), the error would be principally a path following error, for which the MLS functional requirement specification is 0.1°. Thus, the error on glideslope for this particular flight path and transmitter location would probably be viewed as acceptable.

It should also be noted that a MLS basic wide or narrow system at this same location should yield essentially zero error since with the narrower beamwidth, the ground reflection would be completely out of beam.

Figures 10-10 to 10-12 are analogous to Figs. 10-7 to 10-9 except now the transmitter is located at x = 970 and y = 250. We see that the peak multipath level is increased somewhat and, more importantly, the ϕ_{sep} is now approximately -3.6° versus the -5° with the other location. This difference arises because with an extra site further out from the runway and further back, one gets a substantial reflection off a terrain plate which slopes upward and outward;

slope in y direction 3.37°

slope in x direction 0.95°

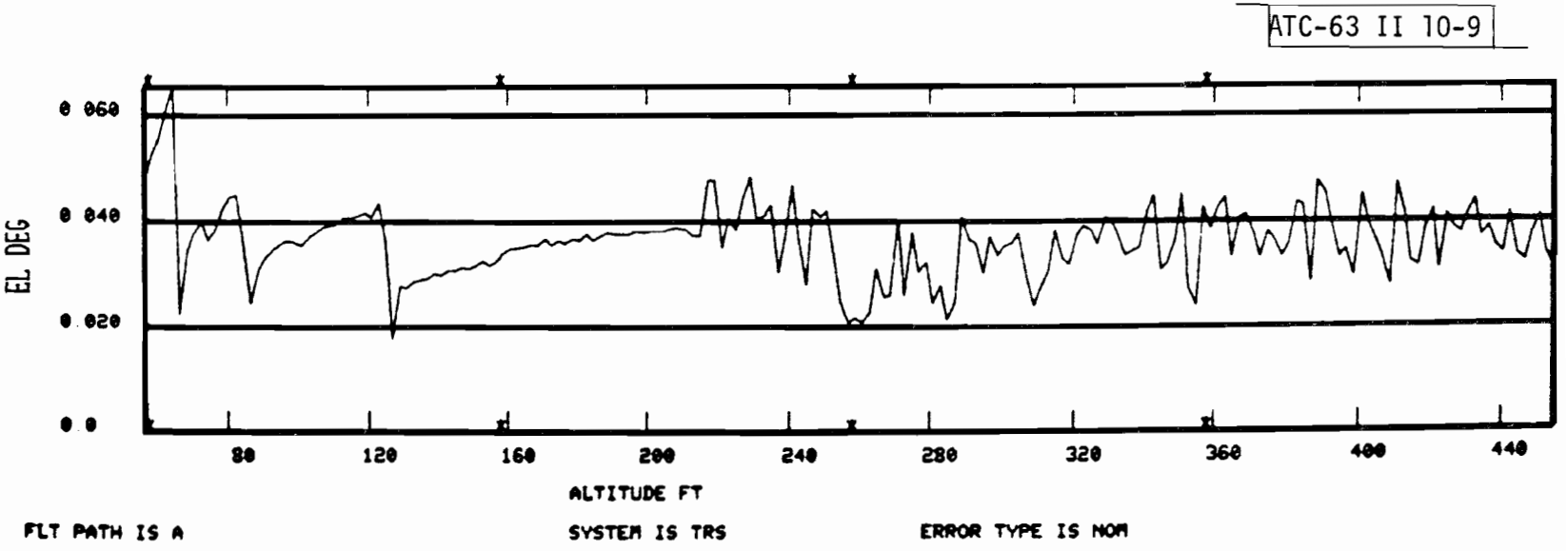

Fig. 10-9. TI demo D system errors at transmitter location #1 with MCT scan stop angle of 1.65° and receiver on 2.86° glideslope.

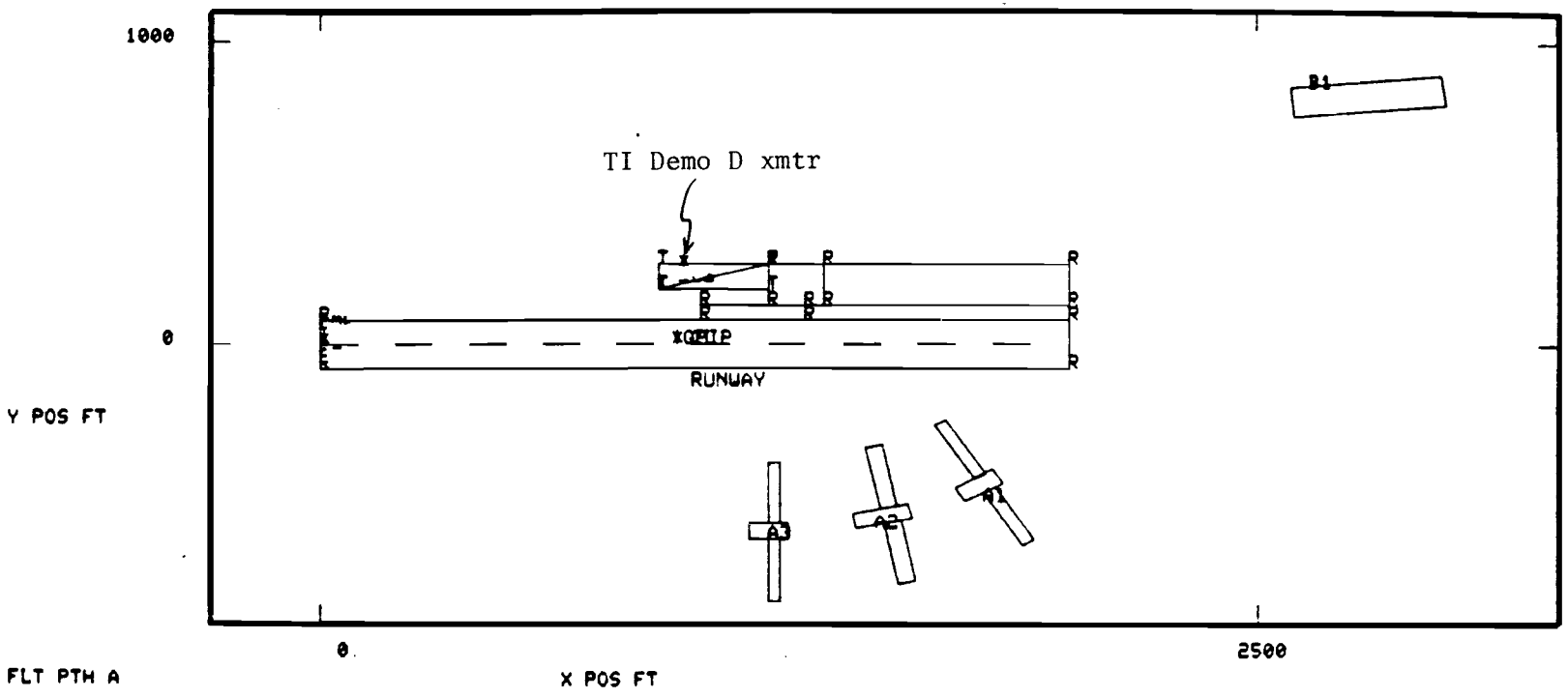

EL SYSTEM

OBST	RANK	AMP	ALT	RDOP
G	1	1	65 0	-10
B1	2	45	450 6	-52
A1	3	80	454 6	0
A2	4	80	454 6	0
A3	5	80	119 0	-991

Fig. 10-10. MLS computer simulation airport map: transmitter location #2.

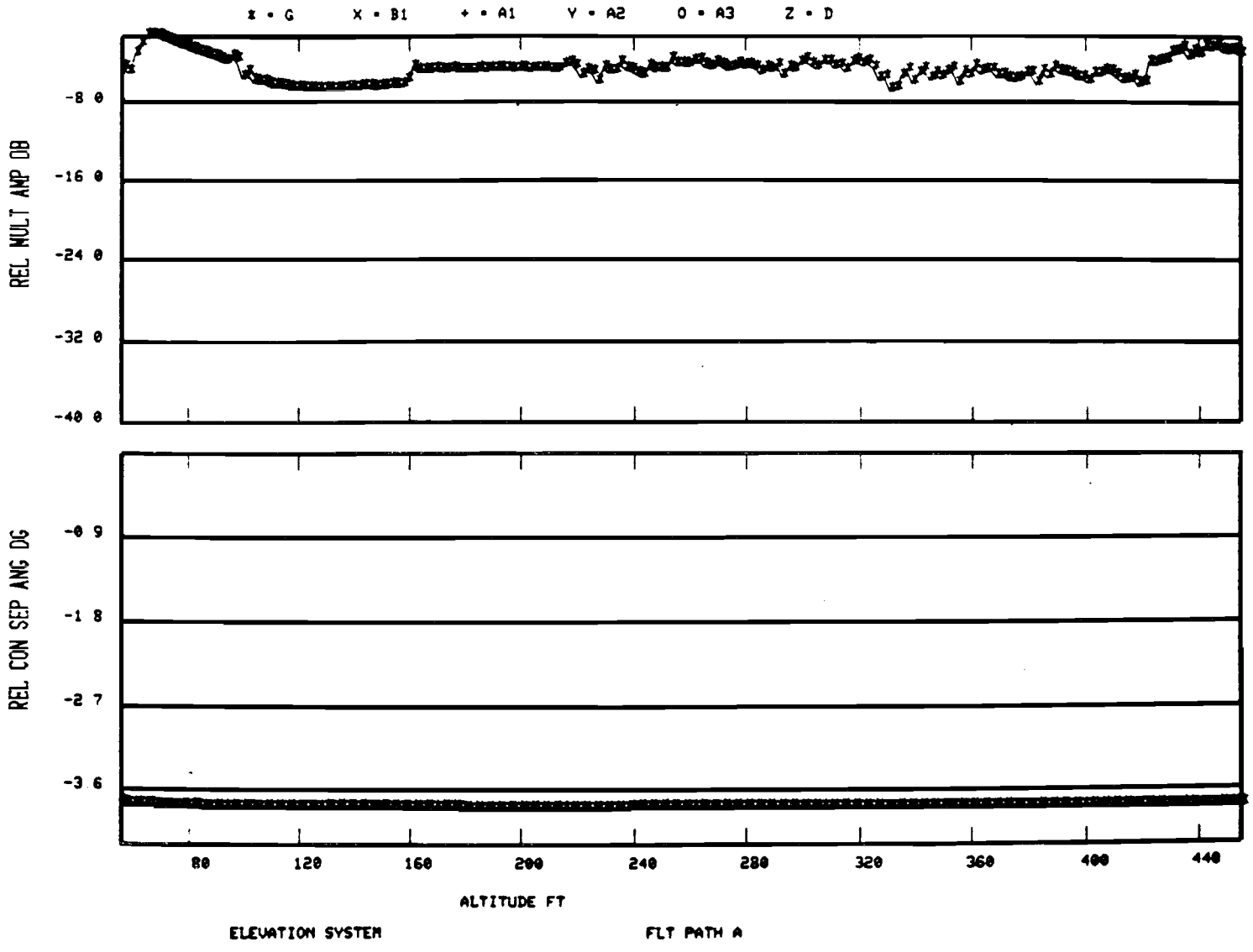

Fig. 10-11. Elevation multipath amplitude and separation angle on 2.86° glideslope for transmitter location #2.

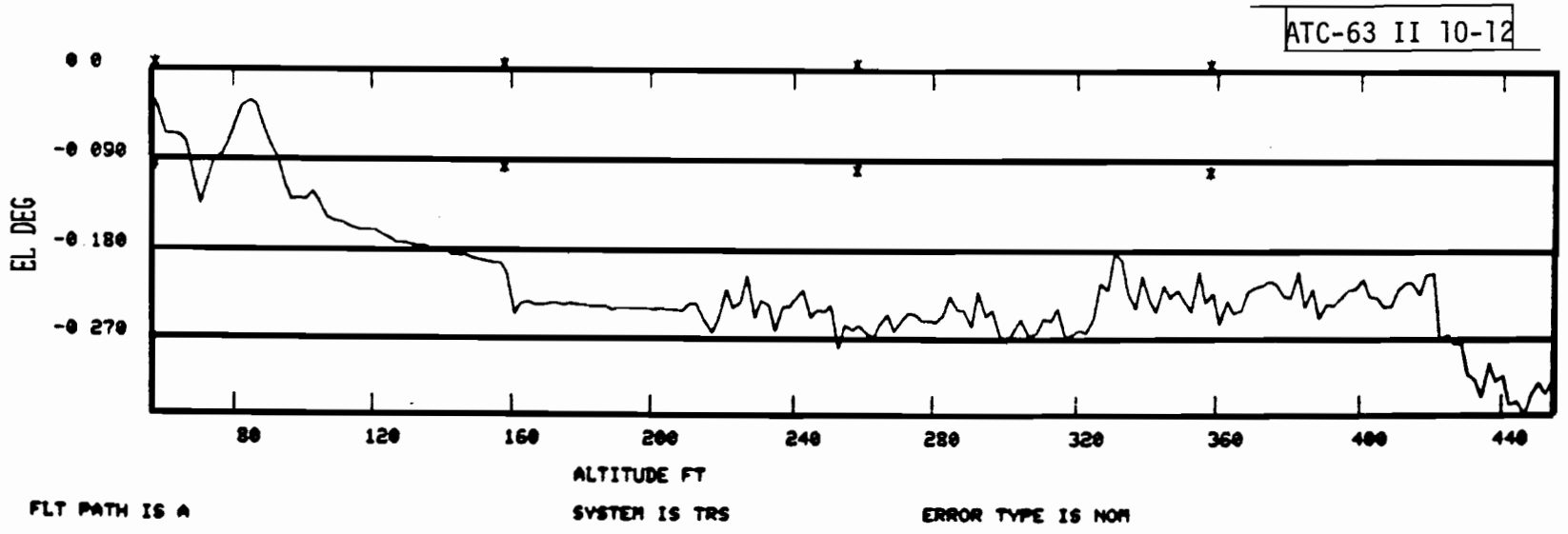

Fig. 10-12. TI demo D system errors at transmitter location #2 for 2.86° glideslope approach.

since

ϕ_{sep} = a/c elevation angle - 2x terrain slope

we see that the change in separation angle is consistent with the change in local terrain slope.

With the reduced separation angle, it is not surprising that the elevation errors in Fig. 10-12 are significantly larger than those of Fig. 10-9. The peak errors on the order of 0.3° are probably unacceptable from the viewpoint of the MLS functional requirements.. The magnitude of the errors is consistent with Fig. 10-3: taking ρ = -6 dB and ϕ_{sep} = -3.7°, Fig. 10-3 yields a worst case error of 0.3°.

Although the TI D system emerges as being quite sensitive to system siting in this case, it should be emphasized that the TRSB basic systems (narrow or wide) should be able to function satisfactorily at either XMTR location since the separation angle exceeded 3° in both cases.

(b) Simulation of Level Flight Path

In view of the large errors encountered on a 3° glideslope with transmitter location 2 (y = 250), a level flight simulation was done only for transmitter location 1 (x = 1020, y = 225). To avoid problems with the plotting routine, the profile used was a linear segment from (88980, 0, 2010) to (15080, 0, 1990), which corresponds to elevation angles from 1.3° to 8°. The aircraft velocity was taken to be 200 ft/sec, but the multipath and system errors were computed at points separated by 720 feet since the multipath was expected to be slowly varying along the path.

The airport map was essentially identical to that of Fig. 10-7. Figure 10-13 shows the variation in ρ and ϕ_{sep} along the path. Since the aircraft is flying an essentially level inbound path, the aircraft elevation angle and ϕ_{sep} increases steadily in magnitude. The ground reflection magnitude represents a complicated interaction of the different plates and Fresnel reflection coefficient which occasionally reaches +1 dB. Since the highest levels occur at the smaller separation angles, it is not surprising that large angular errors occur in Fig. 10-14. The large errors above 2008 ft represent a combination of MCT truncation error (receiver elevation angle is -0.750 wrt MCT scan stop angle) and ground reflection multipath, whereas the other errors represent primarily ground reflection multipath. Without MCT, Figs. 10-3 and 10-13 suggest that the error above 2008 feet would have been on the order of 1.0°.

10.4 Summary and Conclusions

The Texas Instruments "D" system is sensitive to ground reflection multipath from rising terrain for conventional aircraft approach angles due to its large beamwidth. The use of MCT reduces, but does not eliminate, this sensitivity if adequate guidance is to be furnished down to 1.3° elevation angle.

At the proposed Friendship International Airport runway 15 site, there could be problems with rising terrain. However, it is possible to find a site on the preferred side of the runway which yields adequate multipath performance for approaches at or above the current ILS glideslope of 2.86°. For angles below the ILS glideslope, significantly larger ground reflection

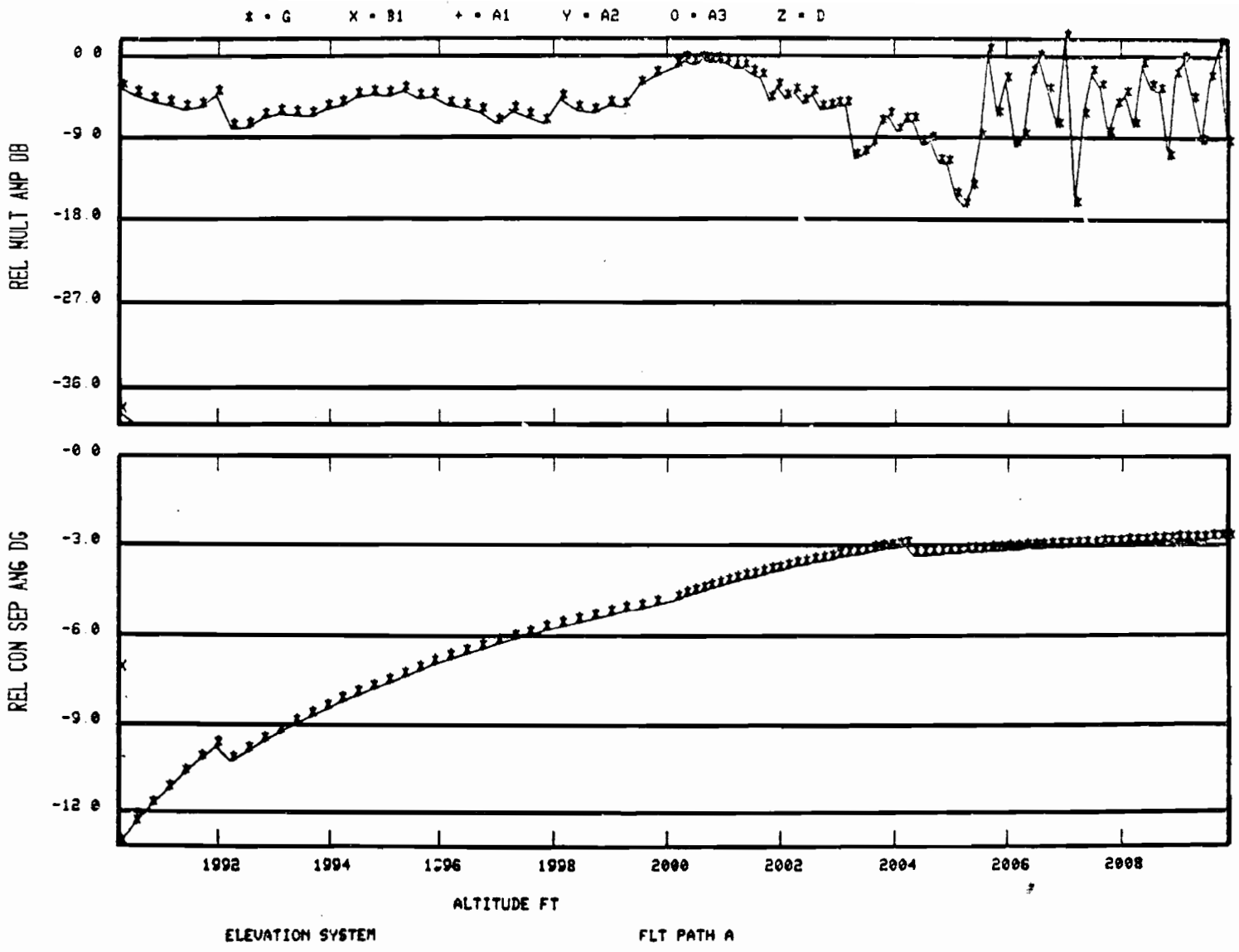

Fig. 10-13. Elevation multipath magnitude and separation angle at transmitter location #1 for level flight.

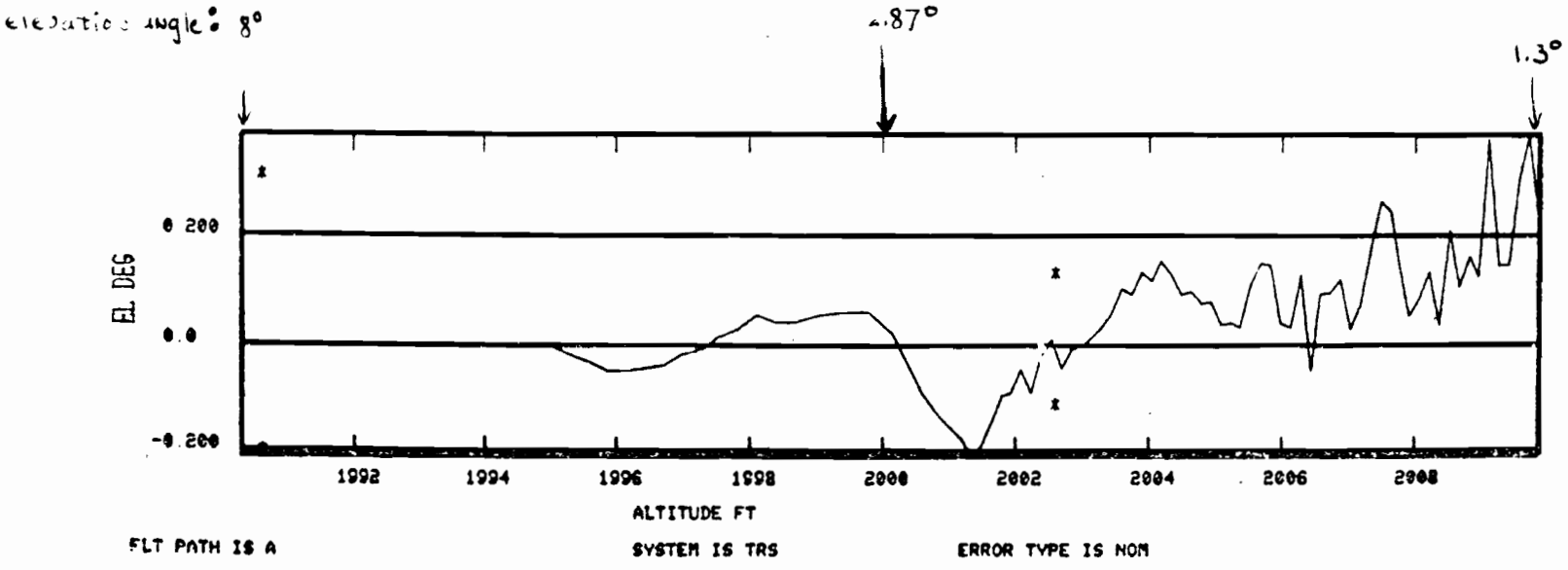

Fig. 10-14. TI demo D system errors at transmitter location #1 for level flight.

errors will occur. The errors due to building and aircraft reflections were negligible.

Based on fact that in all cases the separation angle of the multipath is at least 2.8°, it appears that either of the TRSB basic elevation systems would perform well at the preferred transmitter location for aircraft elevation angles down to 1.4°.

The results of three representative system runs are given in Section 10.3. It appears that with an appropriate choice of transmitter location, adequate accuracy would be achieved on the 2.86° glideslope with ground reflection multipath yielding predominantly a path following error $\leq$ 0.06° which is well within the MLS functional requirement specification of 0.1°. However, at lower angles (e.g., 2°) on a transmitter location in front of rising terrain, very large errors (0.7° - 0.4°) may occur due to ground reflection multipath.

APPENDIX A

MULTIPATH ERROR IN DOPPLER MLS

A.1 Introduction

This appendix presents an anlaysis of the effect of multipath on Doppler MLS. Precise models of the Hazeltine and ITT/Gilfillan methods of signal generation are developed, including, in particular, the bidirectional scan reversals. The analysis derives the measurement error for a single multipath in the absence of receiver filtering. For the case of small to moderate multipath, a final results is obtained that incorporates averaging over a succession of up-down scans.

A.2 Signal Models

We begin with signal models, which are slightly different for the two U.S. Phase II systems.

A.2.1 Hazeltine

In the Hazeltine system, upper and lower sidebands are generated by mixing an independent 100 kHz oscillator with a 47.2 MHz reference. The upper and lower sidebands are extracted by filters and then selected by switches on alternate scans. Reference and selected sideband are translated to RF by a common oscillator. The reference is transmitted directly via a broad coverage antenna. The sideband is transmitted via a multiple feed beamport array that imposes time varying phase shift at each element or port with the result that the sideband frequency observed in the far field varies with observation angle.

The total sideband phase during an upper sideband, up-scan interval is

$$(\omega_c + \omega_o)t + \phi_o + k\theta_d(t - nT_s) \tag{A-1}$$

where ω_c and ω_o are reference and sideband frequency respectively; ϕ_o is an arbitrary sideband phase, $k\theta_d$ is the angle dependent frequency for the direct path and nT_s is the midscan time for the n^{th} scan. The corresponding phase for the lower-sideband $(n + 1)^{th}$ scan is

$$(\omega_c - \omega_o)t - \phi_o - k\theta_d[t - (n+1)T_s] \tag{A-2}$$

The reference and sideband oscillators run continuously and either the upper or lower sideband is gated to the array. The Doppler scan phasing alternates direction at each scan and passes through zero at midscan.

In general, the sideband signal for the n^{th} scan may be represented as

$$\cos\{[\omega_c + (-1)^n\omega_o]t + (-1)^n\phi_o + (-1)^nk\phi_d(t - nT_s)\} \tag{A-3}$$

The reference signal is

$$\cos(\omega_c t + \phi_n) \tag{A-4}$$

where at the n^{th} scan ϕ_n is the digitization phase accumulated on the reference in the Hazeltine system.

At the receiver, a square-law envelope detector effectively forms the product of reference and sideband to yield the subcarrier signal:

$$\cos\{(-1)^n[\omega_o t + \phi_o + k\theta_d(t-nT_s)] - \phi_n\} \tag{A-5}$$

Since cos is an even function, $(-1)^n$ can be factored out and dropped, whereby the sign reversal is transferred to the digitization phase, giving

$$\cos[\omega_o t + \phi_o + k\theta_d(t-nT_s) - (-1)^n\phi_n] \qquad \text{(A-6)}$$

We observe that there would be no need for digitization in the Hazeltine system if the subcarrier frequency ω_o were not a multiple of the scan rate. If the midscan phase $\omega_o nT \pmod{2\pi}$ varies with n from scan to scan, the effect of digitization is accomplished. However, this is not the case since the sideband oscillator also provides timing for scan generation.

Before proceeding to multipath considerations, the signal model for the other Doppler system will be developed.

A.2.2 ITT/Gilfillan

The sideband generator in the ITT/G system consists of a digital phase shifter that advances (retards) the phase of the reference during the up (down) scan. The reference is radiated from a fixed antenna and the sideband is commutated along a linear array. The direction of commutation reverses every scan and a digitization phase step is applied at the beginning of every up scan.

During the $0'^{th}$ scan, the sideband phase is

$$\omega_c t + \omega_o t + (\omega_c + \omega_o)tk \sin\theta_d \quad , \quad -\frac{T_s}{2} < t < \frac{T_s}{2} \qquad \text{(A-7)}$$

After the first scan reversal the phase is

$$\omega_c t + (T_s - t)\omega_o + (\omega_c - \omega_o)(T_s - t)k \sin\theta_d \quad \frac{T_s}{2} < t < \frac{3}{2}T_s \qquad \text{(A-8)}$$

The phase shift due to commutation is referred to zero at midscan or center of the array. The phase due to ω_c and ω_o is continuous across the scan transition. In general, the sideband signal is

$$\cos\{\omega_c t + (-1)^n(t - nT_s)\omega_o + (-1)^n(t-nT_s)\omega_c k \sin\theta_d + (t - nT_s)\omega_o k \cdot \sin\theta_d + \phi_n\} \tag{A-9}$$

The accumulated digitization phase ϕ_n is included.

The Doppler shift represented by the term $(t-nT_s)\omega_o k \sin\theta_d$ does not referse direction at scan reversals. It introduces a proportional error with ratio $\omega_o/\omega_c \approx 3 \times 10^{-5}$. This can be neglected and the term will henceforth be omitted. The omission corresponds to the usual narrowband assumption in which the Doppler shift is treated as a simple spectrum translation. A similar assumption is implicit in the Hazeltine transmitter design.

After square-law detection, the subcarrier output is

$$\cos\{(t - nT)(\omega_o + \omega_c k \sin\theta_d) + (-1)^n\phi_n\} \tag{A-10}$$

Comparing this result with the corresponding one for Hazeltine shows that both can be represented as

$$\cos\{(t - nT_s)(\omega_o + \omega_d) + (-1)^n\psi_n \tag{A-11}$$

where

$$\omega_d = \begin{cases} k\theta_d \text{ for Hazeltine} \\ \omega_c k \sin\theta_d \text{ for ITT/G} \end{cases} \tag{A-12}$$

$$\psi_n = \begin{cases} (-1)^n(\omega_o n T_s + \phi_o) - \phi_n & \text{for Hazeltine} \\ \phi_n & \text{for ITT/G} \end{cases} \qquad \text{(A-13)}$$

A.3 Reference Phase Error Due to Multipath

The reference signal will be perturbed by multipath in both amplitude and phase. The amplitude fading may cause measurement error due to low SNR or due to deviation from desired operating levels for the square-law detector and angle processor. The amplitude effects will not be treated here but the reference shift will be included as a potential source of error at high scalloping rates.

The sum of direct and multipath reference is

$$\cos \omega_c t + \rho_c \cos[\omega_c(t-\tau_c) + \phi_c] \qquad \text{(A-14)}$$

where ρ_c is the amplitude, τ_c the delay and ϕ_c the reflection phase of the multipath. The resultant reference is

$$\sqrt{1 + \rho_c^2 + 2\rho_c \cos(\phi_c - \omega_c\tau_c)}\, \cos\left[\omega_c t + \tan^{-1} \frac{\rho_c \sin(\phi_c - \omega_c\tau_c)}{1 + \rho_c \cos(\phi_c - \omega_c\tau_c)}\right] \qquad \text{(A-15)}$$

The reference phase shift will be denoted ψ_c and after detection will appear as a phase shift on the direct and the multipath subcarrier.

A.4 Subcarrier Phase Error Due to Multipath

The sum of direct and multipath sidebands is

$$\cos[\omega_c t + (-1)^n(t-nT_s)(\omega_o - \omega_d) + \psi_n]$$

$$+ \rho\cos[\omega_c(t-\tau_m) + (-1)^n(t-\tau_m-nT_s)(\omega_o + \omega_m) + \psi_n + \phi_m] \qquad \text{(A-16)}$$

Here ρ is the amplitude, τ_m the relative delay, ϕ_m the reflection phase and ω_m the Doppler frequency of the multipath signals.

After detection the sum of subcarriers is

$$\cos[(-1)^n(t-nT_s)(\omega_o + \omega_d) + \psi_n - \psi_c]$$

$$+ \rho\cos[(-1)^n(t-\tau_m-nT_s)(\omega_o + \omega_m) + \psi_n + \phi_m - \psi_c - \tau_m\omega_c] \qquad \text{(A-17)}$$

The resultant subcarrier phase is

$$(-1)^n(t-nT_s)(\omega_o + \omega_d) + \psi_n - \psi_c$$

$$+ \tan^{-1} \frac{\rho\sin[(-1)^n(t-nT_s)(\omega_m-\omega_d)-(-1)^n\tau_m(\omega_s+\omega_m)+\phi_m-\tau_m\omega_c\ ]}{1+\rho\cos[(-1)^n(t-nT_s)(\omega_m-\omega_d)-(-1)^n\tau_m(\omega_s+\omega_m)-\phi_m-\tau_m\omega_c)} \qquad \text{(A-18)}$$

The $(-1)^n$ to-fro scan dependence may again be factored out leaving

$$\cos\left\{(t-nT_s)(\omega_o+\omega_d) + (-1)^n(\psi_n-\psi_c)\right.$$

$$\left. + \tan^{-1} \frac{\rho\sin[(t-nT_s)(\omega_m-\omega_d)-\tau_m(\omega_o+\omega_m)+(-1)^n(\phi_m-\tau_m\omega_c)]}{1+\cos[(t-nT_s)(\omega_m-\omega_d)-\tau_m(\omega_o+\omega_m)+(-1)^n(\phi_m-\tau_m\omega_c)]}\right\} \qquad \text{(A-19)}$$

A.5 Frequency Measurement Error

The frequency measurement error incurred due to multipath is given by the ratio of the phase difference over the measurement interval to the length of

the interval. Denoting the end points of the interval as t_{n1} and t_{n2}, the subcarrier frequency error (radians/sec) is

$$\frac{1}{t_{n2} - t_{n1}} \left\{(-1)^n[\psi_c(t_{n1})-\psi_c(t_{n2})] + \chi_n(t_{n2}) - \chi_n(t_{n1})\right\} \tag{A-20}$$

where the time dependence of the reference phase ψ_c has been made explicit and χ_n denotes the $\tan^{-1}$ function above.

A.5.1 Reference Phase Contribution to Frequency Error

The reference phase contribution is found by evaluating $\psi_c(t)$ at the two end points. From Section 3

$$\psi_c(t) = \tan^{-1} \frac{\rho_c \sin(\phi_c-\omega_c\tau_c)}{1+\rho_c \cos(\phi_c-\omega_c\tau_c)} \simeq \rho_c \sin(\phi_c-\omega_c\tau_c) \tag{A-21}$$

where the last step invokes the usual small-to-moderate multipath assumption.

The path delay phase difference for linear aircraft motion can be expressed as

$$\omega_c\tau_c(t) = \omega_s t \tag{A-22}$$

where ω_s is the scalloping frequency and the phase is referred to an arbitrary time origin.

Defining the scan duration T_s and scan gate T_g, we have

$$\frac{1}{2}(t_{n2} + t_{n1}) = nT_s$$

$$t_{n2} - t_{n1} = T_g \tag{A-23}$$

The frequency error is then

$$\frac{\psi_c(t_{n1}) - \psi_c(t_{n1})}{T_g} = \frac{\rho_c}{T_g} \left[\sin(\phi_c - \omega_s t_{n1}) - \sin(\phi_c - \omega_s t_{n2})\right]$$

$$= \frac{-2\rho_c}{T_g} \sin(\omega_s T_g/2) \cos(\phi_c - \omega_s n T_s) \qquad \text{(A-24)}$$

The argument of the cosine factor is the midscan phase of the n^{th} scan. Recalling the $(-1)^n$ factor in Eq. (A-20), one may compute the average E_c over two successive scans, the first one being odd.

$$E_c = \frac{-\rho_c}{T_g} \sin(\omega_s T_g/2) \left\{ \cos[\phi_c - \omega_s (n+1) T_s] - \cos(\phi_c - \omega_s n T_s) \right\}$$

$$\frac{-2\rho_c}{T_g} \sin(\omega_s T_g/2) \sin(\omega_s T_s/2) \sin[\phi_c - \omega_s (n+\tfrac{1}{2}) T_s] \qquad \text{(A-25)}$$

The argument of the last sinusoid may be recognized as the phase at the transition between the odd- and even-numbered scans. It is the cyclic variation of the last factor that leads to motion averaging improvement.

When M bidirectional scans separated by a sample spacing $T=2T_s$ are averaged, the improvement is

$$\frac{\sin(M\omega_s T/2)}{M \sin(\omega_s T/2)} = \frac{\sin(M\omega_s T_s)}{2M \sin(\omega_s T_s/2) \cos(\omega_s T_s/2)} \qquad \text{(A-26)}$$

Applying this factor to E_c, the resulting error is

$$\overline{E}_c = \frac{-\rho_c}{T_g} \frac{\sin(M\omega_s T_s)}{M\cos(\omega_s T_s/2)} \sin(\omega_s T_g/2)\sin(\eta_c) \qquad \text{(A-27)}$$

The last sine factor accounts for the arbitrary phase relation between sampling instants and scalloping frequency.

A.5.2 Frequency Error Due to Subcarrier Multipath

In this section we derive the error due to multipath of the subcarrier, in contrast to the carrier multipath error derived above. Again assuming small multipath, the expression to be evaluated at the two end points is:

$$\chi_n(t) \approx \rho\sin\left\{(t-nT_s)(\omega_m+\omega_d)-(\omega_s+\omega_m)\tau_m(t) + (-1)^n[\phi_m-\omega_c\theta_m(t)]\right\} \qquad \text{(A-28)}$$

Inserting

$$\omega_c\tau_m(t) = \omega_s t \qquad \text{(A-29)}$$

$$(\omega_s+\omega_m)/\omega_c = r \qquad \text{(A-30)}$$

and the previous definitions of T_g and T_s gives

$$\begin{aligned}\frac{\chi_n(t_{n2})-\chi_n(t_{n1})}{T_g} &= \frac{\rho}{T_g}\sin\left[T_g(\omega_m-\omega_d)/2-r\omega_s t_{n2}+(-1)^n(\phi_m-\omega_s t_{n2})\right] \\ &\quad - \frac{\rho}{T_g}\sin\left[-T_g(\omega_m-\omega_d)/2-r\omega_s t_{n1}+(-1)^n(\phi_m-\omega_s t_{n2})\right] \\ &= \frac{2\rho}{T_g}\cos\left[-r\omega_s nT_s+(-1)^n(\phi_m-\omega_s nT_s)\right] \\ &\quad \cdot \sin\left[T_g(\omega_m-\omega_d)/2-r\omega_s T_g/2+(-1)^n\omega_s T_g/2\right] \qquad \text{(A-31)}\end{aligned}$$

Averaging over two bidirectional scans, the first one being odd, we get for the multipath error E_s:

$$E_s = \frac{2\rho}{T_g} \sin\left[T_g(\omega_m-\omega_d)/2-r\omega_s T_g/2\right]\cos(\omega_s T_g/2)$$
$$\cdot \cos\left[r\omega_s(n+\tfrac{1}{2})T_s+\omega_s T_s/2\right]\cos\left[r\omega_s T_s/2+\omega_s(n+\tfrac{1}{2})T_s-\phi_m\right]$$
$$+ \frac{2\rho}{T_g}\cos\left[T_g(\omega_m-\omega_d)/2-r\omega_s T_g/2\right]\sin(\omega_s T_g/2)$$
$$\cdot \sin\left[r\omega_s(n+\tfrac{1}{2})T_s+\omega_s T_s/2\right]\sin\left[r\omega_s T_s/2+\omega_s(n+\tfrac{1}{2})T_s-\phi_m\right] \qquad \text{(A-32)}$$

The sinusoidal variation of the error due to the changing phase $\omega_s(n+\frac{1}{2})T_s$, is the so-called scalloping effect which permits a reduction of the error by averaging over a succession of scans.

The ratio r of subcarrier to carrier freqeuncy is on the order of 10^{-5}. Terms of the type $r\omega_s T_s$ are obviously negligible. Even those of the form $nr\omega_s T_s$ are not significant since the scan index n for each averaging interval ranges from 1 to at most 50 and the interesting values of $\omega_s T_s$ are 2π or less. It follows that $nr\omega_s T_s < 10^{-3}$.

Setting r=0 and multiplying E_s by the averaging factor from (A-26) gives

$$E_s = \frac{2\rho}{T_g}\frac{\sin(M\omega_s T_s)}{2M\sin(\omega_s T_s/2)}\sin[T_g(\omega_m-\omega_d)/2]\cos(\omega_s T_g/2)\cos\eta_m$$
$$+ \frac{2\rho}{T_g}\frac{\sin(M\omega_s T_s)}{2M\cos(\omega_s T_s/2)}\cos[T_g(\omega_m-\omega_d)/2]\sin(\omega_s T_g/2)\sin\eta_m \qquad \text{(A-33)}$$

The phase η_m accounts for the arbitrary phasing between sampling instants and scalloping frequency.

The Doppler "beamwidth" in radians is defined as the inverse of the sideband antenna effective aperture in wavelengths (λ/L). The separation angle between direct and multipath expressed in fractional beamwidths is

$$\theta_m = T_s(\omega_m-\omega_d)/2\pi \tag{A-34}$$

Adding in the carrier phase error and letting $\eta_c = \eta_m$, the total multipath error, also expressed in fractional beamwidths, is

$$\bar{E}_m = \frac{\rho T_s}{\pi T_g} \frac{\sin(M\omega_s T_s)}{2M} \left\{ \frac{\sin[\pi\theta_m T_g/T_s] \cos(\omega_s T_g/2) \cos\eta_m}{\sin(\omega_s T_s/2)} \right.$$

$$\left. - \frac{[1-\cos(\pi\theta_m T_g/T_s)] \sin(\omega_s T_g/2) \sin\eta_m}{\cos(\omega_s T_s/2)} \right\} \tag{A-35}$$

When $T_g = T_s$, this result is essentially equivalent to Wheeler's multipath error formula [33]. Because of differences in phase reference definitions, Wheeler's short wave factor corresponding to η_m depends on the separation between direct and multipath.

APPENDIX B

INTERMODULATION DUE TO ENVELOPE DETECTION OF SSB SIGNAL

In the Doppler MLS signal format a reference carrier is transmitted from a fixed antenna while an offset carrier is transmitted from a simulated moving source. The signal in space then consists of a carrier and single-side-band whose frequency relative to the carrier is the offset plus the doppler shift produced by the projection of the moving source velocity onto the line-of-sight to the observer. Considering the offset frequency as a subcarrier, the subcarrier is FM'd in accordance with the angular position of the observer with respect to an axis defined by the source motion.

The objective at the observer is to determine the frequency of the subcarrier. This is accomplished in most direct fashion by envelope detecting the SSB signal to extract the subcarrier followed by filtering and frequency measurement. Other, more elaborate, schemes exist for demodulating the SSB signal. One of these is described in the Hazeltine Phase TACD report [33] and is mentioned later on. The purpose of this appendix is to indicate the effects on SSB envelope detection when multipath components of both the reference carrier and Doppler sideband are present.

The direct path signal is represented as

$$\cos \omega_c t + a_1 \cos [(\omega_c + \omega_1) t + \psi_1] \qquad \text{(B-1)}$$

The reference carrier multipath signal is $\alpha \cos \omega_o (t-\tau)$ whereupon the resultant reference is

$$1 + \alpha^2 + 2\alpha \cos \omega_c \tau \cos (\omega_c t + \psi_c) \qquad \text{(B-2)}$$

The multipath Doppler signal is $a_2 \cos [(\omega_c + \omega_2)t + \psi_2]$. Note that the multipath from the fixed antenna gives rise to reference carrier fading, whereas the moving source multipath produces a doppler sideband distinct from the direct path. Because of the changing geometry, reference and sidebands can be affected independently. This is in contrast to the normal communication situation where carrier and sidebands fade together as long as the signal bandwidth is less than the coherence bandwidth of the channel.

Subsequent equations omit phase angles that becloud the analysis and are irrelevant to the present investigation of intermodulation in envelope detectors. The total signal at the detector input is

$$s(t) = A \cos \omega_c t + a_1 \cos (\omega_c + \omega_1)t + a_2 \cos (\omega_c + \omega_2)t \qquad \text{(B-3)}$$

For narrowband signals the envelope is uniquely determined as $E(t) = \sqrt{I^2(t) + Q^2(t)}$, where $s(t) = I(t) \cos \omega_o t + Q(t) \sin \omega_o t$ and $I(t)$, $Q(t)$ are the in-phase and quadrature components of the bandpass signal referred to an arbitrary in-band carrier. Equivalently, the squared envelope can be derived by squaring $s(t)$ and applying a low-pass filter. The latter approach is somewhat easier to pursue especially when the phase modulation defined as $\tan^{-1}[Q(t)/I(t)]$ is of no interest. Squaring and eliminating second harmonics of ω_c leaves

$$E^2(t) = 1/2[A^2+a_1^2+a_2^2+2Aa_1 \cos \omega_1 t+2Aa_2 \cos \omega_2 t+2a_1a_2 \cos (\omega_1-\omega_2)t] \quad (B-4)$$

If a square-law envelope detector were employed, this would be the total low-pass output. The desired Doppler signal at ω_1 can be filtered to remove the multipath at ω_2 as well as the intermodulation term at $(\omega_1-\omega_2)$. The latter would tend to fall into the data band around the reference carrier. The inter-mod would interfere with data detection if the Doppler scan and data are present simultaneously. A converse interference of data with Doppler would also occur. The data, being normal DSB AM modulation on the reference carrier, will fade together with the carrier. The parameter A above can then be interpreted as including the AM, i.e.,

$$A = \sqrt{1 + \alpha^2 + 2\alpha \cos \omega_c t}\,[1 + mf(t)] \quad (B-5)$$

where data modulation f(t) is imposed with modulation index m. We observe from Eq. (B.4) that the AM appears on the Doppler subcarriers.

The mutual interference is eliminated by not transmitting data and Doppler sidebands simultaneously. This is the approach selected in the optimized doppler format.

Practical envelope detectors are more nearly linear rather than square law. To find the additional spectral components in that case, the square root of Eq. (B.4) must be found. It is assumed that no data modulation accompanies the Doppler signal. Applying the binomial expansion of the square root and letting $R = A^2 + a_1^2 + a_2^2$ gives

$$\frac{2\sqrt{E(t)}}{A^2+a_1^2+a_2^2} = \left[1 + \frac{2Aa_1 \cos \omega_1 t + 2Aa_2 \cos \omega_2 t + 2a_1a_2 \cos(\omega_1-\omega_2)t}{R}\right]^{1/2}$$

$$= 1 + \frac{1}{R}\left[Aa_1 \cos \omega_1 t + Aa_2 \cos \omega_2 t + a_1a_2 \cos(\omega_1-\omega_2)t\right]$$

$$+ 2A^2a_1a_2[\cos(\omega_1+\omega_2)t + \cos(\omega_1-\omega_2)t] + 2Aa_1^2a_2[\cos \omega_2 t + \cos(2\omega_1-\omega_2)t]$$

$$= 1 + \left[\frac{Aa_1}{R} - \frac{Aa_1a_2^2}{2R^2}\right]\cos \omega_1 t + \left[\frac{Aa_2}{R} - \frac{Aa_1^2a_2}{2R^2}\right]\cos \omega_2 t$$

$$+ \left[a_1a_2 - \frac{A^2a_1a_2}{R^2}\right]\cos(\omega_1-\omega_2)t - \frac{Aa_1^2a_2}{2R^2}\cos(2\omega_1-\omega_2)t - \frac{Aa_1a_2^2}{2R^2}\cos(2\omega_2-\omega_1)t \qquad \text{(B-6)}$$

+DC, out of band and higher order products.

From Eq. (B.6) it is apparent that the multipath-to-direct ratio at the linear detector output is

$$M/D = \frac{a_2}{a_1}\left[\frac{1 - \frac{a_1^2}{2R}}{1 - \frac{a_1^2}{2R}}\right]$$

$$\approx \rho\left[1 - \frac{a_1^2}{2R}(1 - \rho^2)\right] \qquad \text{(B-7)}$$

If the angle signal is small relative to the carrier ($a_1 \ll 1$), M/D is approximately equal to ρ, as is the case for square law. If carrier and sideband

are equal ($a_1 = 1$) the linear detector exhibits multipath suppression on the order of 2.5 dB for small ρ. However, this reduction is at the expense of the introduction of the other modulation products shown in Eq. (B.6). For carrier at least 6 dB above sideband, the small multipath characteristics of linear and square law detectors nearly coincide.

APPENDIX C

SCANNING BEAM PEAK LOCATION ERROR DUE TO MULTIPATH

There are a number of different methods for processing the detected signal envelope in a scanning beam receiver so as to determine the beam, i.e., pulse, position. The mean of leading and trailing edges is one candidate; a split-gate discriminator is another. As a first approximation, the split-gate discriminator can be represented by an equivalent filter followed by a differentiator. For multipath interference in the absence of noise, the filter plays a secondary role and will be neglected in this analysis.

The problem is now to find the point of zero derivative on the envelope of the sum of direct signal plus multipath. The resultant squared envelope is

$$A^2(\theta) + \rho^2 A^2(\theta-\theta_m) + 2\rho A(\theta)\, A(\theta-\theta_m) \cos \psi \qquad \text{(C-1)}$$

where $A(\theta)$ is the beam envelope vs angle, θ_m is the multipath separation, ρ is the relative multipath referred to the peaks of the two beams and ψ is relative phase between the two signals.

For the sake of analytical tractability, the beam pattern is taken as Gaussian with a half-power (-3 dB) beamwidth, BW:

$$A(\theta) = \exp\left[-k \left(\frac{\theta}{BW}\right)^2\right] \qquad k = 2 \ln 2 \qquad \text{(C-2)}$$

The pertinent derivatives are

$$\frac{dA(\theta)}{d\theta} = -\frac{2k}{(BW)^2}\,\theta A(\theta) \tag{C-3}$$

$$\frac{dA(\theta-\theta_m)}{d\theta} = -\frac{2k}{(BW)^2}\,(\theta-\theta_m)\,A(\theta-\theta_m) \tag{C-4}$$

Differentiating the envelope and setting the result equal to zero gives

$$0 = A^2(\theta) + \rho^2(\theta-\theta_m)\,A^2(\theta-\theta_m) + \rho A(\theta)\,A(\theta-\theta_m)(2\theta-\theta_m)\cos\psi \tag{C-5}$$

whence

$$\frac{\theta}{\theta_m} = \frac{\rho^2[A(\theta-\theta_m)/A(\theta)]^2 + \rho\cos\psi[A(\theta-\theta_m)/A(\theta)]}{1+\rho^2[A(\theta-\theta_m)/A(\theta)]^2 + 2\rho\cos\psi[A(\theta-\theta_m)/A(\theta)]} \tag{C-6}$$

Inserting the beam pattern yields

$$\frac{\theta}{\theta_m} = \frac{\rho^2Y^2 + Y\cos\psi}{1 + \rho^2Y^2 + 2Y\cos\psi} \tag{C-7}$$

$$Y = \exp\left[-k\left(\frac{\theta_m}{BW}\right)^2\left(1 - 2\,\frac{\theta}{\theta_m}\right)\right] \tag{C-8}$$

The solution to this nonlinear equation is a point of zero derivative of the envelope. Assuming that only one such solution exists, it corresponds to the peak of the envelope.

The above equation is solved numerically by a one-point iteration of the form

$$x_{n+1} = F(x_n) \tag{C-9}$$

For input parameters BW, ρ and θ_m, a curve of θ vs ψ is generated. The initial value is $\theta = 0$ at $\psi = 0$. The iteration proceeds until $|x_{n+1}-x_n| < 0.01\ x_{n+1}$. Iterations for subsequent increments of ψ use the preceding solution of θ/θ_m as the initial value.

The theoretical curves in Fig. 6.3 were produced by this method. The theoretical peak location error is less than the simulation error, substantially so when the dwell gate broadening occurs as explained in Fig. 4-8. Split gate discriminators that are approximations to peak location would not be subject to the large dwell gate broadening errors.

APPENDIX D

MULTIPLE COMPONENT TRSB ERROR FORMULA

A formula for TRSB static error in the presence of several small-amplitude multipath components is derived. This result proves useful in the critical area study program.

With the i-th of M multipath components, $1 \leq i \leq M$, associate relative amplitude ρ_i, separation θ_i(BW) and phase angle ϕ_i. The assumed antenna pattern, A(x), is Gaussian:

$$A(x) = 2^{-2x^2} = e^{-kx^2} \quad ; \quad k = 2 \ln 2 \tag{D-1}$$

where x is angle in BW's. With all the multipath components present, the squared envelope (as a function of scan angle) is

$$e^2(x) = \left| A(x) + \sum_{i=1}^{M} \rho_i A(x-\theta_i)\, e^{j\phi_i} \right|^2 \tag{D-2}$$

When the right-hand side is expanded out and second order terms in amplitude (i.e., $\rho_i \rho_j$) are dropped, the equation may be written as

$$e^2(x) = A^2(x)\left[1 + 2 \sum_{i=1}^{M} \eta_i\, e^{2k\theta_i x} \cos \phi_i \right] \tag{D-3}$$

where η_i is the "effective" multipath amplitude:

$$\eta_i = \rho_i e^{-k\theta_i^2} \tag{D-4}$$

The objective is to solve for the leading and trailing edge threshold crossings, i.e., solutions of

$$e^2(x) = e^{-2kv^2} \tag{D-5}$$

v being the nominal threshold crossing location in beamwidths. Taking logarithms in (D-3), and using the small argument approximation $\ln(1 + y) \simeq y$, the equation becomes

$$kx^2 = kv^2 - \sum_{i=1}^{M} \eta_i e^{2k\theta_i x} \cos \phi_i \tag{D-6}$$

For the leading edge crossing, replace x by

$$x = -v + \varepsilon_\ell \tag{D-7}$$

where ε_ℓ is the leading edge error. In the exponential term, x can be replaced by the nominal value (-v) alone. Retaining only the linear term in ε_ℓ yields a solution

$$= -\frac{1}{2kv} \sum_{i=1}^{M} \eta_i e^{-2kv\theta_i} \cos \phi_i \tag{D-8}$$

Similarly, for the trailing edge crossing, replace x by

$$x = v + \varepsilon_t \tag{D-9}$$

and solve for the trailing edge error, which is

$$\varepsilon_t = \frac{1}{2kv} \sum_{i=1}^{M} \eta_i \, e^{2kv\theta_i} \cos \phi_i \tag{D-10}$$

The average of ε_ℓ and ε_t is the error made by a dwell gate processor:

$$\varepsilon = \frac{1}{2} (\varepsilon_\ell + \varepsilon_t)$$

$$= \sum_{i=1}^{M} \rho_i \theta_i \, e^{-k\theta_i^2} \, \frac{\sinh 2kv\theta_i}{2kv\theta_i} \cos \phi_i \tag{D-11}$$

Although (D-11) is a single scan error result, it applies equally to the to-fro error in the static case since the scans yield mirror-image waveforms. Note that the multiple component result is merely the sum of the single component errors.

The criteria used for the threshold crossing [Eq. (D-3)] assumes a threshold with respect to the unperturbed beam maximum, as might occur with a slow acting AGC and high scalloping rates. If a real time thresholding system is used, then one seeks solutions of

$$e^2(x) = e^{-2kv^2} [e^2(x)]_{max}$$

$$\approx e^{-2kv^2} e^2(0) \tag{D-12}$$

It turns out that, making the same approximations as above, that (D-12) yields the error expression (D-11). This result suggests that in the presence of "small" multipath with high scalloping rates, slow acting AGC and real time thresholding will yield essentially identical performance.

APPENDIX E

SEMIRIGOROUS TREATMENT OF DOPPLER SCANNING FROM A CIRCULAR ARRAY

This appendix presents a mathematical analysis from the point of view of conventional antenna theory of the Hazeltine circular array for generating MLS doppler signals in space. The principles of operation of the array are explained in a more direct way than any of the previously offered analyses. In particular, the work provides a firm mathematical foundation for the notion of a moving "bright spot".

In addition to the basic doppler coding, the chirp phenomenon and its elevation angle dependence are derived. The behavior of the received signal amplitude as a function of observation angle and scan time is also predicted. A mathematical explanation of the latter phenomena has not previously been reported. The theoretical results are consistent with computer simulations conducted by Hazeltine during Phase I studies.

E.1 Far-Field Formulation

With reference to Fig. E-1, let $A(\psi)$ be the complex excitation along a continuous circular line aperture. Then the far field pattern in the plane of the circle is given as a function of azimuth angle θ by

$$E(\theta) = \int_{-\psi_c}^{+\psi_c} A(\psi) \exp[j \frac{2\pi r}{\lambda} \cos(\psi - \theta)] \, d\psi$$

The equation results from geometrical considerations using the center of the circle as a phase reference. For example, the radiation from the element at $\psi = \theta$ is advanced by r/λ wavelengths with respect to the elements on the diameter normal to θ ($\psi = \theta \pm \pi/2$).

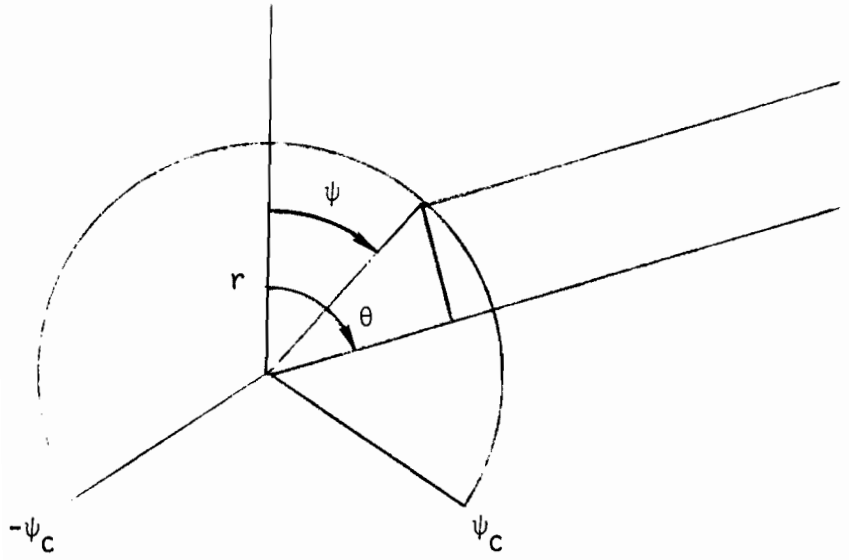

Fig. E-1. Circular line aperture.

The excitation specified by Hazeltine as a function of angle along the aperture is*

$$A(\psi) = \exp(j\, 2\pi f_{da}\, \psi t)$$

This represents a frequency offset from the carrier proportional to the angular position of the aperture element.

Inserting for $A(\psi)$ in the integral and making a change of variables $x = \psi - \theta$ gives

$$E(\theta) = \int_{-\psi_c-\theta}^{\psi_c-\theta} \exp[j2\pi f_{da} t(x + \theta)] \exp[j \frac{2\pi r}{\lambda} \cos x]\, dx$$

The factor independent of x may be taken outside the integral. Defining $a = 2\pi r/\lambda$ and $u = 2\pi f_{da} t/a$ leaves

$$E(\theta) = \exp(j2\pi f_{da}\theta t) \int_{-\psi_c-\theta}^{\psi_c-\theta} \exp[ja(u + \cos x)]\, dx$$

Except for the limits of integration, which we return to later, the remaining integral is independent of θ. As advertised, the far-field pattern has a linearly time-varying phase, i.e., constant frequency directly proportional to the azimuth angle θ. There is an additional time-varying factor due to the integral that is eliminated by appropriately modulating the common excitation to all aperture elements.

E.2 Azimuth-Independent Modulation

The common modulation can be found by evaluating the integral using the method of stationary phase. [76] This is a method for approximating integrals of the form

*The time-dependent excitation common to the entire aperture is not included here but will be derived shortly.

$$I = \int A(x)\, \exp[j\, a\, g(x)]\, dx$$

when a is large.

The stationary phase points are those where the phase a g(x) rotates slowly resulting in maximum contribution to the integral. Elsewhere the phase changes rapidly, the integrand is highly oscillating and the net contribution to the integral is small. Assume that the slope of g(x) is zero at only one point x_o between the limits of integration.*

$$\dot{g}(x_o) = 0$$

It can be shown that the integral asymptotically approaches the following value for $a \to \infty$.

$$I \sim A(x_o) \frac{2\pi}{a|\ddot{g}(x_o)|} \exp[j\, a\, g(x_o) + j\, \pi/4]$$

For the problem at hand

$$g(x) = ux + \cos x$$

$$\dot{g}(x) = u - \sin x = 0$$

$$x_o = \sin^{-1} u$$

$$\ddot{g}(x_o) = -\cos x_o = -\sqrt{1 - u^2}$$

Hence

$$I \sim \sqrt{\frac{2\pi}{a\sqrt{1 - u^2}}} \exp[j\, a\, (u \sin^{-1} u + \sqrt{1 - u^2}) + j\pi/4]$$

The exponent in this expression is the time-varying phase or chirp independent of azimuth. The amplitude variation over the scan cycle of the form $(1 - u^2)^{-1/4}$ has been observed in computer simulations performed by Hazeltine during Phase I [33].

*The existence of a second stationary phase point is discussed subsequently.

The time-varying phase can be eliminated by appropriately phase modulating the aperture excitation. Ignoring the constant phase at $u = 0$, the compensating phase can be expanded in a power series

$$\phi(u) = -\frac{a}{2}\left(u^2 + \frac{u^4}{12} + \ldots\right)$$

Using only the quadratic phase term as Hazeltine suggests imposes a linear FM on each aperture element in addition to the constant frequency offset that produces the angle coding. The resultant excitation frequency is a displaced FM ramp, with displacement varying according to position along the aperture. This behavior is shown in the diagram of frequency vs time for a few elements in the circular array (Fig. E-2).

Expressed in terms of the original coordinate system, the stationary phase point's location on the aperture is

$$\psi_o(u) = \sin^{-1} u + \theta$$

It is seen to move as a function of scan time u, reaching a point in line with the direction of observation θ at midscan u=0. The apparent motion of this so-called "bright spot" produces the chirp derived above. However, the motion of the stationary phase point cannot be used to explain the basic doppler angle coding. A simple heuristic model similar to the moving source of the commutated linear array is still lacking.

E.3 Aperture Cut-Off Considerations

Returning to the question of integration limits, it has been assumed thus far that the stationary phase point lies within the limits. This need not be the case. If the range of integration is restricted so as not to encompass the desired stationary phase point, the radiation from the aperture is reduced.

The commutation of the array during the scan as described by Hazeltine will be examined from this point of view. Aperture cut-off angles that

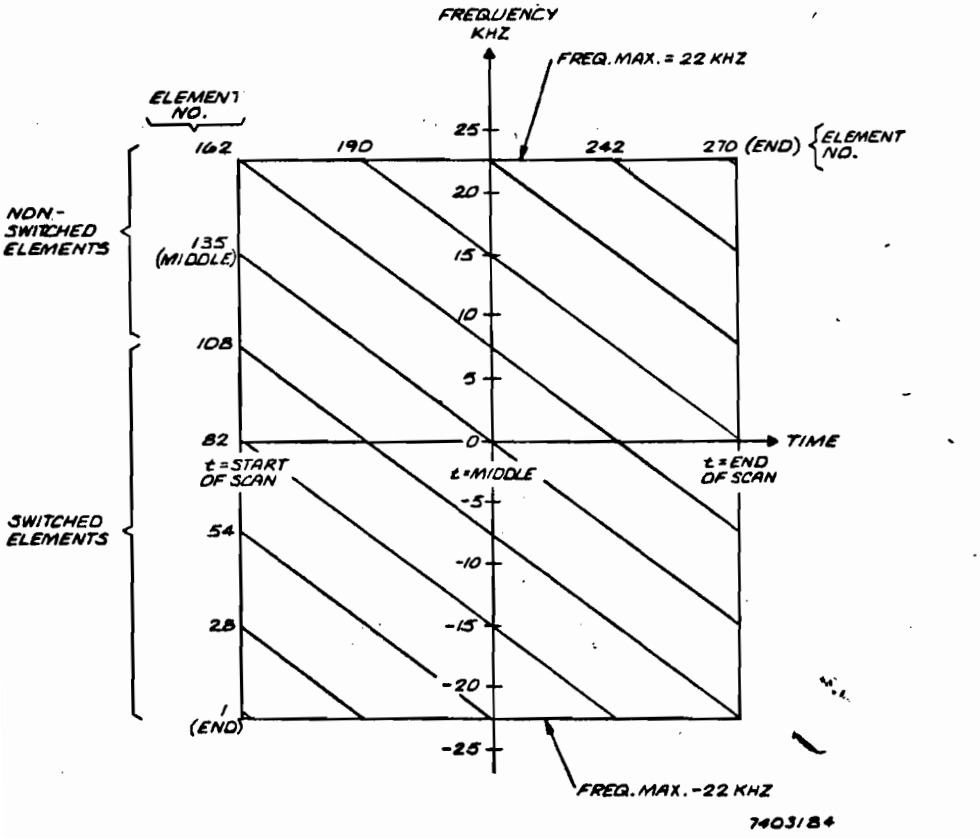

Fig. E-2. Frequency relations with scan time from Hazeltine Phase II Report, Fig. 21-27 [33].

vary with normalized scan time u lead to limits of integration defined as

$$\text{Lower} = -75^{o} + \sin^{-1} u$$

$$\text{Upper} = +75^{o} + \sin^{-1} u$$

These limits as well as the fixed limits $\pm 120^{o}$ are plotted vs u in Fig. E-3 along with a graph of the stationary phase point $\psi_o(u)=\sin^{-1} u+\theta$ The scan time is assumed to reach a maximum of $u_{max} = \sin 45^{o}$. This is close to the value derived from the Hazeltine parameters.

As long as the limits of integration encompass the stationary phase point $\psi_o(u)$, the desired output is obtained. As $\psi_o(u)$ changes due to the azimuth viewing angle θ, part or all of it will fall outside the limits and the radiation is correspondingly reduced. With the commutated array the limit lines are parallel to $\sin^{-1}u$ and the radiation disappears suddenly beyond $|\theta| \approx 75^{o}$. With fixed limits, the radiation gradually reduces at the end (beginning) of the scan for positive (negative) θ. This behavior is evident from Hazeltine's simulation results reproduced in Figs. E-4 and E-5.

E.4 Elevation Angle Dependence

The preceding derivation pertained to the far field in the plane of the aperture circle. When viewed from a conical elevation angle $\alpha \neq 0$ the relative phase from the aperture elements changes. The expression for the pattern generalizes to

$$E(\theta) = \int_{-\psi_c}^{+\psi_c} A(\psi) \exp[j \frac{2\pi r}{\lambda} \cos \alpha \cos(\psi - \theta)] \, d\psi$$

Comparison with the previous derivation reveals that a is simply replaced by $a \cdot \cos \alpha$. The compensating phase modulation $-\frac{a}{2}u^2$ valid for zero elevation is longer correct and there remains a residual chirp viz. $(\cos \alpha - 1)\, u^2/2$. This phenomenon was also observed during Hazeltine Phase I simulation and its consequences discussed. It leads to a

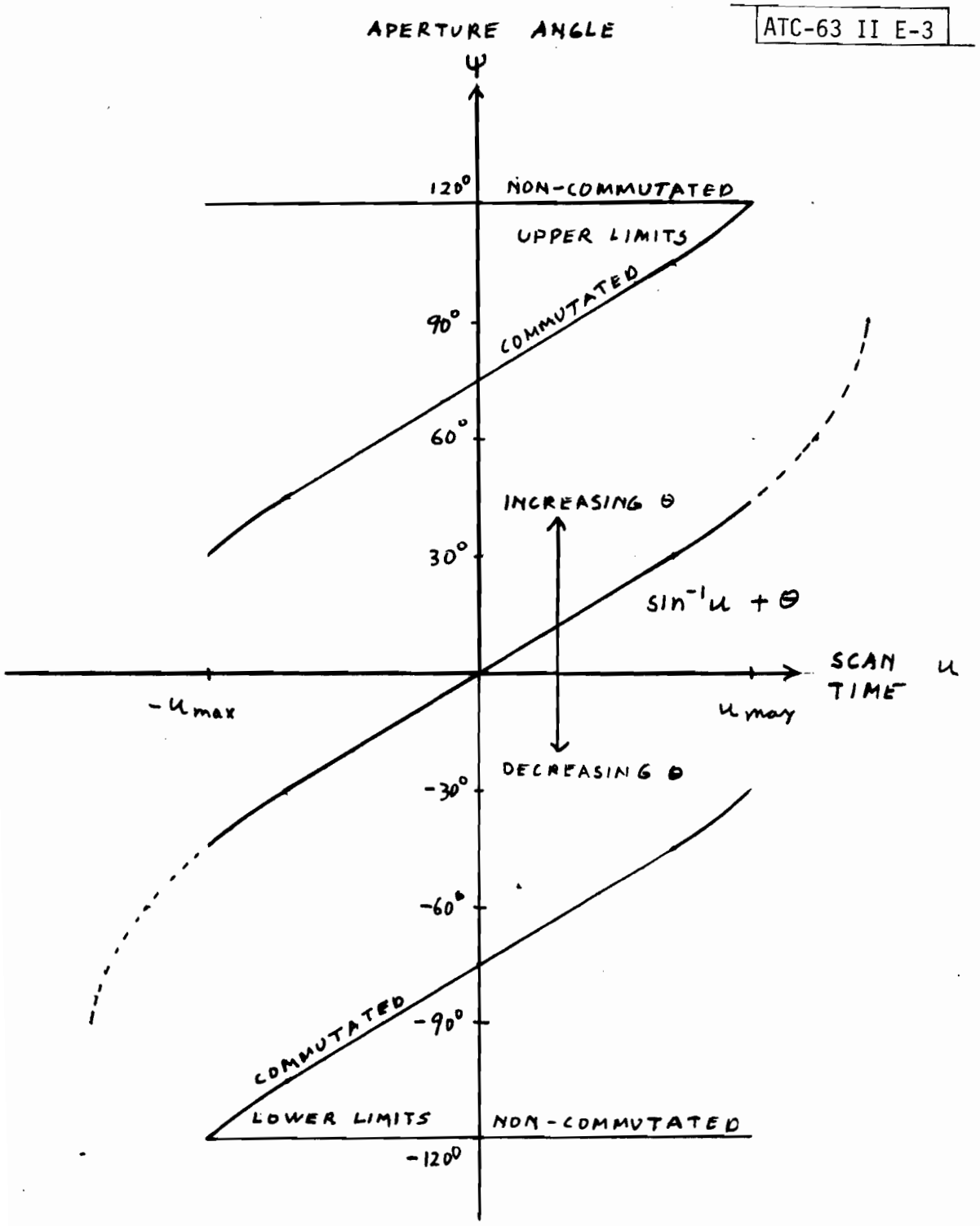

Fig. E-3. Integration limits and stationary phase points.

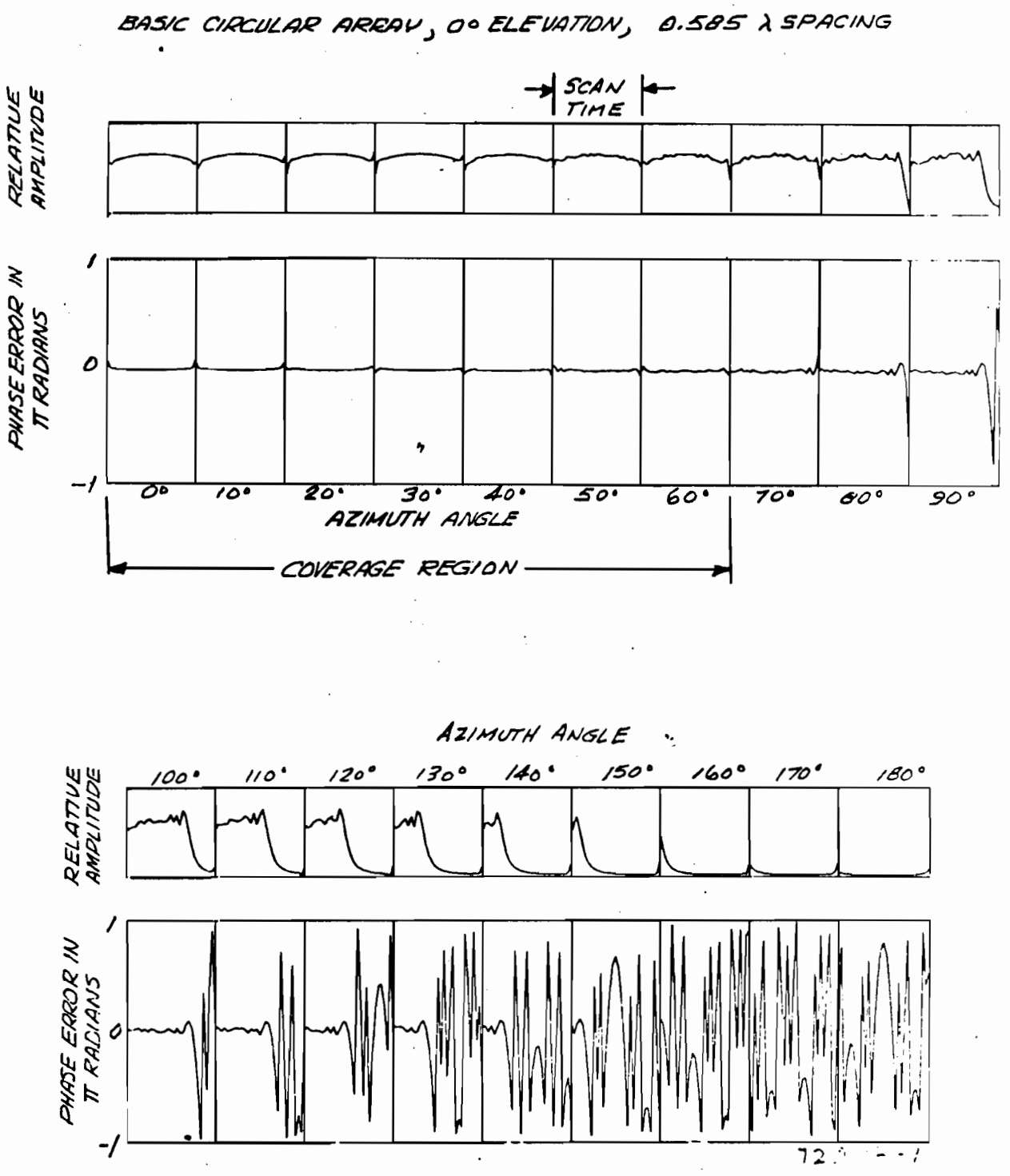

Fig. E-4. Computed Doppler signals from Hazeltine Phase I Report, Fig. 4-37 [33].

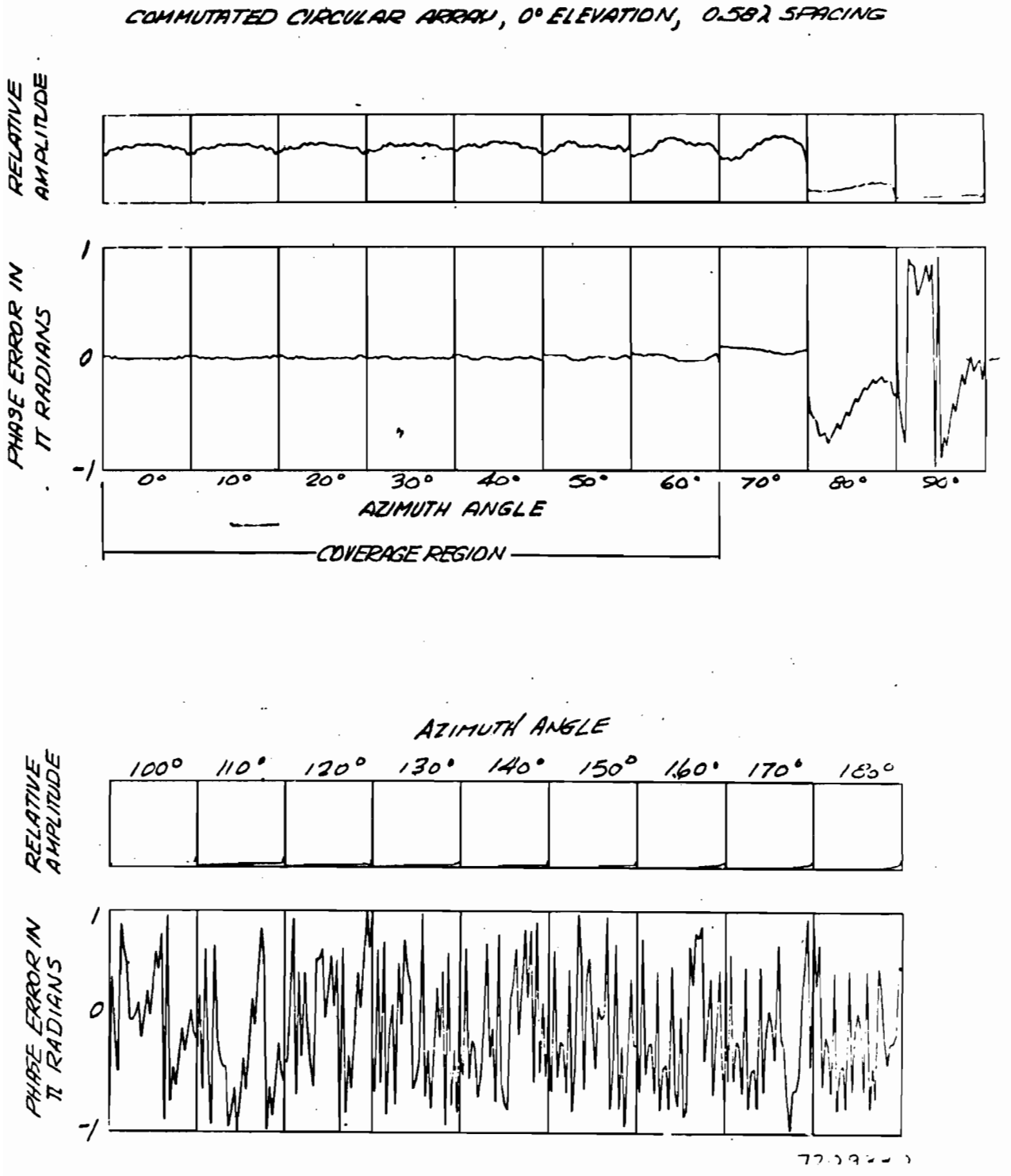

Fig. E-5. Computed Doppler signals from Hazeltine Phase I Report, Fig. 4-33 [33].

broadening of the Doppler band and a consequent widening of filters at the higher elevation. The average frequency over the scan remains unchanged.

E.5 The Second Stationary Phase Point

Further examination of the stationary phase integral reveals that there exist two solutions to the equation

$$\dot{g}(x) = u - \sin x = 0$$

They are $x_o = \sin^{-1} u$ already used and

$$x_1 = \pi - \sin^{-1} u$$

$$\cos x_1 = - \cos x_o$$

The asymptotic value of the integral corresponding to x_1 is

$$I_1 \sim \sqrt{\frac{2\pi}{a\sqrt{1 - u^2}}} \exp [j a(\pi u - u \sin^{-1} - \sqrt{1 - u^2}) + j\pi/4]$$

The contributions from the two stationary phase points must be added to obtain the total integral.

The relative contribution from the second stationary phase point depends on the amplitude pattern of the individual aperture elements. Thus far, omnidirectionality has been assumed, but in practice the array elements tend to be directive outwards. The portion of the aperture associated with the second stationary phase point is 180^o removed from the first, i.e., $\psi_1 = \psi_o + \pi - 2 \sin^{-1} u$, whereas the direction of observation is on the side of the array corresponding to x_o. The elements contributing to x_1 are either non-existent or they are effectively shielded towards the observer.

Observe that the second stationary point produces a frequency offset with respect to the first one through the factor

$$\exp j\pi au = \exp j2\pi^2 f_{da} t$$

For 333 Hz/deg angle coding, πf_{da} = 60 kHz. The unwanted signal falls outside the passband (± 20 kHz relative to the angle carrier) and can there be removed by filtering.

For the reasons cited in the two preceding paragraphs, the effect of the second stationary phase point may be ignored.

References

1. "Experimentation with REGAL Vertical Guidance Landing System," FAA Rep. RD-64-149 (Nov. 1964).

2. "Experimentation with FLARESCAN Vertical Guidance Landing System," FAA Rep. RD-64-150, Proj. 114-012-00X (Nov. 1964).

3. "Advanced Scanning Beam Guidance System for All Weather Landing," FAA Rep. RD-68-2, Proj. 320-01N (Feb. 1968).

4. L.N. Spinner and V.L. Bencivenga, "Advanced Scanning Beam Guidance System for All Weather Landing," FAA Syst. Res. Dev. Serv., Washington, D.C., RD 68-2 (Feb. 1968) AD 665 973.

5. E.J. Murphy, "Exploratory AILS Multipath Investigations" NAFEC Technical Note 1.

6. _____,"Modils Azimuth Investigations," NAFEC Technical Note 4.

7. _____,"Miscellaneous Tests on AILS and MODILS," NAFEC Technical Note 5.

8. _____,"Test and Evaluation of an Advanced Integrated Landing System for all Weather Landing," (Aug. 1970) FAA-RD-70-28.

9. V.L. Bencivenga, "Test and Evaluation of a Portable Scanning Beam Guidance System," (March 1972) FAA-RD-72-16.

10. J.D. Burlage, "AWCLS Take on Carrier Landings," U.S. Naval Aviation News (Nov. 1967).

11. "All Weather Landing System for Combat Aircraft," Interavia (March 1969).

12. "The STOL Navigation Package: 3-D Area Nav and MLS Provide Pinpoint Accuracy," Canadian Aviation (April 1974).

13. Woodward, J.E., "Post-1970 Scanning Beam Approach and Landing," AGARD Conf. Proc. No. 59 on Aircraft Landing Systems AGARD-CP-59-70 (May 1969).

14. "Test of the FLARESCAN Flareout System in Caravelle Number 02." Ministere des Armees (AIR), Direction Technique et Industrielle, Centre D'Essais en Vol. (April 1964).

15. F.X. Kelly, "Tests of Scanning-Beam Microwave Landing Systems at Difficult Sites," presented at technical seminar "Aviation - A Tool for Economic Development," First International Aerospace Show, Sao Paulo, Brazil (Sept. 1973).

16. R.J. Kelly, "Time Reference Microwave Landing System Multipath Control Techniques," Institute of Navigation 31st Annual Meeting (June 1975).

17. P. Fombonne, "Position Errors in Microwave Landing Systems," Electronics and Civil Aviation Intl. Conf., Paris, France (June 1972).

18. ITT/Gilfillan, "Microwave Landing System (MLS) Development Plan as Proposed by ITT/Gilfillan During the Technique Analysis and Contract Definition Phase," FAA-RD-74-118.

19. L. Sanders, "Multipath Challenge for MLS," Electronics and Civil Aviation International Conf., Paris, France (June 1972).

20. S.A. Meer, "Microwave Landing System Siting Case Studies at Kennedy, LaGuardia and Newark Airports," MITRE Corp. MTR-6958 (August 1975).

21 G. Ploussious, "Low Angle Guidance for Scanning Beam Systems," report to CALSPAN by Meyer Assoc. (21 Jan. 1975).

22. Bendix Corp., "Refined Microwave Landing System (MLS) Program Development Plan (Phase III)," (1 Oct. 1974).

23. C.W. Wightman, et al, "Dynamic Multipath Effects on MLS Scanning Beam and Doppler Scan Techniques," Cornell Aero. Lab., Inc., (Sept. 1972) FAA-RD-72-124.

24. _____,"Dynamic Multipath Performance of Airborne Processors," Report TN-3, Calspan Corp. (3 Dec. 1974).

25. _____,"Performance Characteristics of MLS Phase II Receiver-Processors," TN-4, Calspan Corp. (Dec. 1975).

26. "Microwave Landing System (MLS) Development Plan as Proposed by Texas Instruments,Inc., During the Technique Analysis and Contract Definition Phase of the National MLS Development Program," (1 Sept. 1972) FAA-RD-74-170.

27. J. Benjamin, and G.E.J. Peake, "Contributions to the U.K. Microwave Landing System Study (Phase I)," Royal Aircraft Establishment, Tech Memo 1021 (May 1973).

28. A.E. Brindley, L.C. Calhoun, and T.N. Patton, (IITRI) "Multipath Environment Evaluation," Air Force Flight Dynamics Laboratory (Nov. 1974) AFFDL-TR-74-150.

29. D.A. Shnidman, "The Logan MLS Multipath Experiment," Project Report ATC-55, Lincoln Laboratory, M.I.T. (23 Oct. 1975) FAA-RD-75-130.

30. Hazeltine Corp., "Refined Microwave Landing System (MLS) Development Program Plan Feasibility Demonstration Phase II," Report 11009 (1 Oct. 1974).

31. ITT/Gilfillan, "Five Year MLS Development Program Plan (updated) Microwave Landing System," MLS-0420 (1 October 1974).

32. Texas Instruments, Inc., "Refined Microwave Landing System (MLS) Development Program Plan," DM74-03-04 (1 Oct. 1974).

33. Hazeltine Corp., "Microwave Landing System (MLS) Development Plan as Proposed by Hazeltine Corp. During the Technique Analysis and Contract Definition Phase of the National MLS Development Program," (27 Sept. 1973) FAA-RD-73-185.

34. Bendix Corp., "Microwave Landing System (MLS) Development Plan as Proposed by Bendix Corp. During the Technique Analysis and Contract Definition Phase of the National MLS Development Program," (Sept. 1972) FAA-RD-74-152.

35. S.A. Meer, "Estimate of MLS Shadowing, Critical Areas and Airport Building Restrictions," MITRE Corp., MTR-6847 (May 1975).

36. D.A. Shnidman, "Airport Survey for MLS Multipath Issues," Project Report ATC-58, Lincoln Laboratory, M.I.T. (Nov. 1975) FAA-RD-75-195.

37. P.S. Demko, "Polarization/Multipath Study," U.S. Army Electrom. Command Rep. VL-5-72 (Aug. 1971/June 1972).

38. R.A. Rondini and R.H. McFarland, "Experimental Validation of Boeing 747 ILS Signal Scattering Calculations for Critical Area Determination," FAA SRDS (Jan. 1974) FAA-RD-74-57.

39. Microwave Landing System Technique Assessment Doppler Working Group, "Final Report of the Doppler Working Group" (Dec. 1974).

40. C.S. Smith and P. Barton, "Experiments with Narrow Band Information Filters," in UK Phase II Progress Report to FAA MLS Assessment (Sept. 1974).

41. Final Report to NATO: Performance of Advanced Approach and Landing Systems (AALS), Vol. 4, Appendix 1, Electronics Research Laboratory, Univ. of Trondheim, Norwegian Inst. of Tech. (March 1973).

42. N. Blachman, "Zero-Crossing Rate for the Sum of Two Sinuesoids or a Signal Plus Noise," IEEE Trans. on Info. Theory, Vol. IT-21 (Nov. 1975) pp. 671-675.

43. A.E. Brindley, L.E. Calhoun, T.N. Patton and L. Valcik, "Analysis, Test and Evaluation Support to the USAF Advanced Landing System Program," USAF Flight Dynamics Lab. (Aug. 1974) AFFDL-TR-74-62.

44. R. Collin and F. Zucker, Antenna Theory: Part I, McGraw-Hill, New York (1969).

45. "Aeronautical Telecommunications," Annex 10 to the Convention on International Civil Aviation, 2nd Ed., Vol. 2, International Civil Aviation Organization (April 1968).

46. F.G. Overbury, "The Effects of Scalloping and a Further Discussion of Scalloping," in Study of the Doppler Landing Guidance System - Second Report," Standard Telecommunications Laboratories (Oct. 1972).

47. P. Beckman, "Scattering by Composite Rough Surfaces," Proc. IEEE, (Aug. 1965), pp. 1012-1015.

48. D.E. Kerr, Propagation of Short Radio Waves, McGraw-Hill Book Co.,N.Y. (1951).

49. P. Beckmann, and A. Spizzichino, The Scattering of Electromagnetic Waves from Rough Surfaces, Pergamon Press, N.Y. (1963).

50. J.W. Goodman, Introduction to Fourier Optics, McGraw-Hill Book Co., N.Y. (1968).

51. K.M. Mitzner, "Change in Polarization on Reflection from a Tilted Plane," Radio Science, Vol. 1, no. 1 (Jan. 1966). pp. 27-29.

52. S. Silver, Microwave Antenna Theory and Design, McGraw-Hill Book Co., N.Y. (1949).

53. H.J. Riblet and C.B. Barker, "A General Divergence Formula," J. of Applied Physics, Vol. 19 (Jan. 1948). pp. 63-70.

54. R.E. Kell, "On the Derivation of Bistatic RCS from Monostatic Measurements," Proc. IEEE, (Aug. 1965), pp. 983-988.

55. R.D. Kodis, "A Note on the Theory of Scattering from an Irregular Surface," IEEE Trans. Ant. Prop., Vol. AP-14, no. 1 (January 1966), pp. 77-82.

56. D.E. Barrick, "Rough Surface Scattering Based on the Specular Point Theory," IEEE Trans. Ant. Prop., Vol. AP-16, no. 4 (July 1968), pp. 449-454.

57. T.P. McGarty, "Models of Multipath Propagation Effects in a Ground-to-Air Surveillance System," Technical Note 1974-7, Lincoln Laboratory, M.I.T. (25 February 1974).

58. E.C. Jordan and K.G. Balmain, Electromagnetic Waves and Radiating Systems, Prentice-Hall, Inc., N.J. (1968).

59. S.O. Rice, "Diffraction of Plane Radio Waves by a Parabolic Cylinder: Calculation of Shadows Behind Hills," Bell System Tech. Jour., Vol. 33 (March 1954), pp. 417-504.

60. G.T. Ruck, D.E. Barrick, W.D. Stuart and C.K. Krichbaum, Radar Cross Section Handbook, Vol. 1, 2, Plenum Press, N.Y. (1970).

61. J.W. Crispin, and K.M. Siegel, Methods of Radar Cross-Section Analysis, Academic Press, N.Y. (1968).

62. R. Horonjeff, Planning and Design of Airports, McGraw-Hill, N.Y. (1962).

63. J.B. Keller, "Geometrical Theory of Diffraction," J. of the Optical Society of America, Vol. 52, No. 2 (February 1962), pp. 116-130.

64. A. Sommerfeld, Optics, Academic Press, New York (1954).

65. A Spiridon, "Impact of Obstacle Shadows on Monopulse Azimuth Estimate," Project Report ATC-50, Lincoln Laboratory, M.I.T., FAA-RD-75-91.

66. "Test Requirements and Coordination Plan, National Microwave Landing System Phase II Test Program," FAA MLS Division (7 Sept. 1973).

67. C.J. Hirsch, "Experimentation for the Use of L-band DME with the MLS," Final Report to FAA SRDS (Feb. 1974).

68. "Final Report of the MLS Scanning Beam Working Group to the MLS Technique Assessment," MLS Scanning Beam Working Group (Dec. 1974).

69. G. Ploussious, "Circular Polarization Analysis Interim Report #2: Aircraft Reflections," Meyer Assoc., Inc., U.S. Army Contract #DAAB07-75-C-0801 (31 Jan. 1975).

70. _____ "Circular Polarization Analysis Final Report," Meyer Assoc., Inc., U.S. Army Contract #DAAB07-75-0801 (Dec. 1975).

71. G. Litchford, "Study and Analysis of SC-117, National and USAF Plans for a New Landing System," Technical Report AFFDL-TR-72-76 Part II, U.S. Air Force Flight Dynamics Laboratory (May 1974).

72. G.J. Schlieckert, "An Analysis of Aicraft L-band Beacon Antenna Patterns," Project Report ATC-37, Lincoln Laboratory, M.I.T. (15 Jan. 1975), FAA-RD-74-144.

73. T.C.M. Tong and T.B.A. Senior, "Scattering of Electromagnetic Waves by a Periodic Surface with Arbitrary Profile," Scientific Rep. 13, Univ. of Michigan (April 1972) AFCRL-72-0258.

74. A. Hessel and J. Shmoys, "Computer Analysis of Propagation/Reflection Phenomena," Scientific Report Contract Number DAAB07-73-M-2716, Polytechnic Inst. of Brooklyn (Aug. 1973).

75. K.A. Zaki and A.R. Neureuther, "Scattering from a Perfectly Conducting Surface with a Sinusoidal Height Profile: TE-Polarization," IEEE Trans. Antennas Prop. AP-19, 208-214 (1971).

76. K.A. Zakai and A.R. Neureuther, "Scattering from a Perfectly Conducting Surface with a Sinusoidal Height Profile: TM-Polarization," IEEE Trans. Antennas Prop. AP-19, 747-751 (1971).

77. A. Papoulis, The Fourier Integral and its Applications, McGraw-Hill, N.Y. (1962), pp. 134-143.